Turbulence characterisation for Astronomical Observatories

SHEPHERD, HARRY,WILLIAM

Turbulence characterisation for Astronomical Observatories

by

Harry Shepherd

Supervisor: Dr RW Wilson

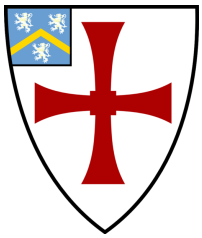

Submitted in conformity with the requirements
for the degree of Doctor of Philosophy
Centre for Advanced Instrumentation
Department of Physics
University of Durham

Abstract

Turbulence characterisation for Astronomical Observatories

Harry Shepherd

Atmospheric turbulence has two effects in astronomy; (i) the broadening of the point spread function due to phase fluctuations limiting the resolution of imaging and (ii) producing intensity fluctuations known as scintillation. Adaptive Optics (AO) can be installed on telescopes to correct for the effect of phase, and with the push to large telescopes more complex AO systems such as Multi Conjugate AO (MCAO) and Multi Object AO (MOAO) are desired. Operation of these systems requires a detailed profile of the turbulent atmosphere in real time.

In this thesis we consider two turbulence profilers, SLOpe Detection And Ranging (SLODAR) and SCIntillation Detection and Ranging (SCIDAR), two cross beam profilers that retrieve data using covariance of phase variations (SLODAR) and intensity variations (SCIDAR). We present a modification of SLODAR to allow an estimate for non resolved turbulence to be made by considering scintillation in the subapertures of a Shack Hartmann wavefront sensor. A new SCIDAR (Stereo–SCIDAR) is described, allowing dynamic re–conjugation to improve altitude resolution.

Practical considerations for the implementation of a SLODAR instrument are considered, including a discussion of potential false measurements of non Kolmogorov power spectra in the ground and surface layers of turbulence. Data is presented from SLODAR observing campaigns on La Palma, and at Paranal. Evidence is presented for orographic effects on measured turbulence, including those due to man made structures.

Contents

Declaration **v**

List of Figures **vi**

List of Tables **ix**

Acronyms **x**

Acknowledgements **xii**

1 Introduction **1**
1.1 Introducing the Thesis 1
1.2 Thesis synopsis 3

2 Introduction and Theory **5**
2.1 Optical Turbulence 5
2.1.1 Structure of the Turbulent atmosphere 6
2.1.2 Models of Turbulence 7
2.1.3 Propagation of Light Through Atmospheric Turbulence 12
2.1.4 Effect of propagation on the phase power spectrum 13
2.1.5 Measuring Atmospheric Turbulence 17
2.2 Adaptive Optics 19
2.2.1 Wavefront Sensing 19
2.2.2 Wavefront Correctors 23
2.2.3 Wavefront Reconstruction 23
2.2.4 Laser Guide Stars 25
2.2.5 Multi-Object Adaptive Optics (MOAO) 27
2.2.6 Ground Layer Adaptive Optics (GLAO) 27
2.2.7 Multi-Conjugate Adaptive Optics (MCAO) 28
2.2.8 Implications for turbulence profiling 28
2.3 SLODAR 31
2.3.1 SLODAR Principle 31
2.3.2 SLODAR response functions, and β 32
2.3.3 Different SLODAR configurations 34
2.4 SCIDAR 35
2.4.1 SCIDAR Principle 35
2.4.2 SCIDAR instruments 35

3 Simulation **37**

3.1 Methods for Computer Simulation of Atmospheric Turbulence 37
3.1.1 Generating phase screens 38
3.1.2 Geometric Propagation 38
3.1.3 Fresnel Propagation 39
3.1.4 Sampling Limits 40
3.2 Verification of the Simulation 42
3.2.1 Phase Screens 42
3.2.2 Fresnel Propagation 43
3.3 Assumptions made 45
3.4 Conclusions 46

4 Stereo-SCIDAR 48
4.1 Introduction 48
4.2 Stereo-SCIDAR Response Functions 50
4.3 Data Reduction 51
4.4 Results from Simulation 53
4.4.1 Response to a single layer 54
4.4.2 Closely spaced layers 55
4.4.3 Determining the altitude of a Single Layer 56
4.4.4 Effects of misconjugation 60
4.4.5 Effects of β on S-SCIDAR 62
4.5 Comparison with G-SCIDAR 64
4.5.1 Simulation and data reduction of G-SCIDAR simulations 64
4.5.2 Example simulation results from G-SCIDAR 66
4.6 On sky example 66
4.7 Conclusion 69

5 Whole Atmosphere SLODAR 73
5.1 Introduction 73
5.2 Methodology 74
5.2.1 Calculating propagation corrected SLODAR Impulse Response Functions (SIRFs) 74
5.2.2 Fitting unresolved turbulence 75
5.3 Results 76
5.3.1 Corrected SIRFs 76
5.3.2 Fitting un-sensed turbulence 82
5.4 On sky testing of this method 86
5.4.1 Simulation results for 50 cm telescope 87
5.4.2 Comparison with MASS 90
5.4.3 Description of the Surface Layer SLODAR at Paranal 93
5.4.4 Comparison with MASS 96
5.5 Conclusions 102

6 Practical SLODAR 105
6.1 Introduction 105
6.2 The La Palma SLODAR 106
6.2.1 Description of the instrument 107
6.2.2 Profiling Campaign 107
6.2.3 Comparison with DIMM 107
6.2.4 Turbulence profiles 113

6.3 Real world effects on a SLODAR instrument . . . 114
6.3.1 Beta . . . 114
6.3.2 Convergence of Measurements . . . 119
6.3.3 Temporal Sampling . . . 121
6.3.4 Dome and Tube turbulence . . . 122
6.3.5 SL-SLODAR specific considerations . . . 124
6.4 Discussion of the effect of weather conditions and local topography . . . 127
6.4.1 La Palma . . . 127
6.4.2 Paranal . . . 128
6.4.3 Conclusions . . . 135
6.5 Conclusion . . . 139

7 Conclusion **141**
7.1 A summary of conclusions . . . 141
7.1.1 Stereo SCIDAR . . . 141
7.1.2 FA-SLODAR . . . 142
7.1.3 La Palma SLODAR observing campaign . . . 143
7.1.4 Practical Effects on SLODAR . . . 143
7.2 Proposed future work . . . 144
7.2.1 SCIDAR . . . 144
7.2.2 Full atmosphere SLODAR . . . 145
7.2.3 Geographical and Meteorological Effects . . . 145

Bibliography **147**

Declaration

The material in this thesis is based on research carried out at the Centre for Advanced Instrumentation, the Department of Physics, the University of Durham, United Kingdom. No part of this thesis has been submitted elsewhere for any other degree or qualification. The research reported within this thesis has been conducted by the author unless indicated otherwise.

Publications

Some of the work presented has been published in the following:

J. Osborn, R.W. Wilson, T. Butterley, H. Shepherd, and M. Sarazin. Profiling the surface layer of optical turbulence with SLODAR. *Mon. Not. R. Astron. Soc*, 406:1405, 2010.

G. Lombardi, J. Melnick, R. Hinojosa Goi, J. Navarrete, M. Sarazin, A. Berdja, A. Tokovinin, R. Wilson, J. Osborn, T. Butterley, and H. Shepherd. Surface layer characterization at Paranal Observatory. In *Proceedings of the SPIE*, volume 7733, page 77334D, 2010.

Copyright Notice

List of Figures

2.1 Figure illustrating the effects of atmospheric turbulence on a telescope PSF. . 6
2.2 Figure showing a Kolmogorov, modified von Karman, and generalised power spectrum. 8
2.3 Kolmogorov phase power spectrum with and without the modification for atmospheric scintillation propagation. 15
2.4 Figure illustrating a Shack Hartmann wavefront sensor. 19
2.5 Figure illustrating G- and Z-tilts. 20
2.6 Figure illustrating the first 4 radial modes of Zernike Polynomials. 22
2.7 Figure illustrating focal anisoplanatism. 26
2.8 SLODAR turbulence profile measured from the WHT. 29
2.9 Overview of the SLODAR geometry. 31
2.10 Cross and auto covariance movies for iSLODAR and OTP 33

3.1 A demonstration of Fresnel propagation on phase and intensity. 40
3.2 Simulation results showing centroid variance against r_0 for two different sub-aperture sizes. 43
3.3 Simulation results showing scintillation variance against layer altitude, demonstrating the $\sigma_I \propto h^{5/6}$ relationship for small apertures. 44
3.4 Simulation results showing scintillation variance against layer altitude, demonstrating the $\sigma_I \propto h^2$ relationship for large apertures 45

4.1 The effects of increasing the optical propagation distance on the altitude resolution of SCIDAR. 49
4.2 A schematic of the Stereo SCIDAR instrument 50
4.3 The effects of increasing propagation distance on the cross covariance response for S-SCIDAR. 52
4.4 A schematic overview of the SCIDAR simulation. 53
4.5 Plots of theoretical SCIDAR response functions against those from Monte-Carlo simulation. 54
4.6 Plots of theoretical and simulated peak SIRF values for S-SCIDAR. 55
4.7 Simulated S-SCIDAR profiles for a range of conjugation distances, showing two narrowly spaced turbulent layers with equal strengths. 57
4.8 Simulated S-SCIDAR profiles for a range of conjugation distances, showing two narrowly spaced turbulent layers with differing strengths in a 40:60 ratio. 58
4.9 Simulated S-SCIDAR profiles for a range of conjugation distances, showing two narrowly spaced turbulent layers with differing strengths in a 30:70 ratio. 59
4.10 The effects of misconjugating the two detectors of the S-SCIDAR instrument. 61

4.11 Comparison of Kolmogorov and non Kolmogorov responses, and profile fitting for S-SCIDAR . . . 63
4.12 Suppression of the S-SCIDAR response functions for different β values. . . . 64
4.13 A slice through a G-SCIDAR autocovariance for a two layer atmosphere. . . . 65
4.14 Example simulated profiles of G-SCIDAR measuring a 2 layer atmosphere. . . 67
4.15 Diagram of the conjugate-plane photometer from which the S-SCIDAR measurements were made. . . . 68
4.16 Profile of the NOT S-SCIDAR for several conjugate altitudes. . . . 68
4.17 Cross covariance movie for the NOT S-SCIDAR. . . . 70
4.18 Example turbulence profile for the NOT S-SCIDAR. . . . 71

5.1 Flowchart showing the fitting method for FA-SLODAR. . . . 77
5.2 A comparison of SLODAR Impulse Response Functions with and without Fresnel propagation correction. . . . 79
5.3 Orthogonality plot for Fresnel corrected SIRFS. . . . 80
5.4 Effect of differing inner and outer scale on the generation of SLODAR impulse response functions. . . . 81
5.5 Fitting Fresnel and non Fresnel corrected impulse response functions to a two layer atmosphere (0km and 4km). . . . 83
5.6 Fitting the height of a single layer of unresolved turbulence using corrected impulse response and scintillation variance. . . . 84
5.7 Fitting the strength of a single layer of unresolved turbulence using both corrected impulse response and scintillation variance. . . . 85
5.8 Plot showing theoretical and Monte Carlo simulation results for subaperture scintillation variance for FA-SLODAR with subaperture diameter of 4.75 cm. 88
5.9 Plot showing theoretical and Monte Carlo simulation results for subaperture scintillation variance for FA-SLODAR with subaperture diameter of 6.25 cm. 89
5.10 MASS response functions for a typical instrument. . . . 91
5.11 Mass profile for 1:00 UT, 18/03/2011 at Paranal Chile. . . . 92
5.12 Illustration of bias when retrieving a single altitude from a MASS profile, with no *a priori* knowledge. . . . 94
5.13 Photo of the SL-SLODAR instrument . . . 95
5.14 Map of average subaperture illumination for the SL-SLODAR with binary components of magnitudes 4.48 and 5.74. . . . 96
5.15 Illustration of the telescope aperture for SL-SLODAR projected onto an 8×8 wavefront sensor. The subapertures used to measure the scintillation index for the FA-SLODAR are highlighted. . . . 97
5.16 Free atmosphere height measured by FA-SLODAR plotted against height measured by MASS at Paranal, for 222 nights of data. . . . 98
5.17 Free atmosphere turbulence strength measured by FA-SLODAR plotted against the integrated strength measured by MASS at Paranal, for 222 nights of data between March 2011 and February 2012. . . . 99
5.18 Free atmosphere turbulence strength measured by FA-SLODAR against the prediction made by the current SL-SLODAR. . . . 100
5.19 Scatter plot, and cumulative frequency histogram showing the estimates for isoplanatic angle made my SL-SLODAR and MASS at Paranal. . . . 101
5.20 Distribution of scintillation variance as measured by the FA-SLODAR subapertures. . . . 103

6.1 Map showing the location of the SLODAR instrument on the top corner of the Caldera de Taburiente. . . . 106
6.2 Photo of the pt5m instrument . . . 108
6.3 WHT SLODAR v DIMM seeing. . . . 109
6.4 WHT SLODAR v DIMM seeing, showing low, medium, and high wind speeds. 110
6.5 The average WHT SLODAR and DIMM seeing for each given wind direction as measured by the ING weather station. . . . 111
6.6 WHT SLODAR v DIMM seeing, indicating the results as the wind blows from the caldera, and from all other directions. . . . 112
6.7 The effects of wind direction on the turbulence profile at the ORM . . . 112
6.8 Pearson's χ^2 for the Gaussian distribution of wavefront slopes measured by the La Palma SLODAR as a function of seeing angle. . . . 114
6.9 Three examples of the fitting of Gaussian distribution to wavefront slopes measured by the La Palma SLODAR. . . . 115
6.10 Average profile from the La Palma SLODAR. . . . 116
6.11 Figure showing Kolmogorov and $\beta = 9/3$ SLODAR response functions, and the effect of fitting a Kolmogorov response to a single layer of non-Kolmogorov atmospheric turbulence. . . . 118
6.12 Effect of wind speed on the measured value for β. . . . 118
6.13 Comparison of the wind speed vs. β plots for SL-SLODAR data and Monte-Carlo simulation. . . . 120
6.14 Plot of two simulated SLODAR measurements of r_0, for independent realisations of a turbulent atmosphere with identical strengths. . . . 121
6.15 Maximum wind speed detectable by SLODAR. . . . 122
6.16 An illustration of the effect of dome and tube seeing on SLODAR auto covariance . . . 123
6.17 An example of temporal filtering on a SLODAR turbulent profile. . . . 124
6.18 An example of SL-SLODAR turbulence profile showing an absence of dome seeing and surface layer of turbulence for the early part of the night. . . . 125
6.19 Figure showing the effect of rotational misalignment for the two detectors in an SL-SLODAR system. . . . 126
6.20 The Monthly median seeing recorded by RoboDIMM between 2008 and 2012. 129
6.21 Wind roses for Paranal, colour coded by discrepancy between DIMM seeing and UT image quality, and the temperature gradient between 2 and 30 m. . . . 131
6.22 Directional effects on the SL-SLODAR profile at Paranal. . . . 133
6.23 Directional effects on the SL-SLODAR profile at Paranal for summer and winter. . . . 134
6.24 Arial photograph of the observing platform at Cerro Paranal. . . . 136
6.25 Plot of SLODAR and DIMM total seeing for 2 nights at Cerro Paranal . . . 137
6.26 Turbulence profiles corresponding to the plots in figure 6.25. . . . 138

List of Tables

4.1 The effects of re-conjugating the S-SCIDAR to pin-point the altitude of a single turbulent layer 60
4.2 The effect of misconjugating S-SCIDAR on the peak and integrated turbulence for a single layer. 61

5.1 High layer fitting for a two atmosphere model with a low resolved layer, and an unresolved layer at 10 km. 86
5.2 Quartiles and Median isoplanatic angles measured by SL-SLODAR and MASS. 101

6.1 Median and Quartiles for seeing measured by the ING RoboDIMM each year between 2008 and 2011. 128
6.2 Frequency of the wind directions at the Paranal observatory, for the directions that result in the large seeing discrepancies. 131

Acronyms

ANN	artificial neural networks
aO	active optics
AO	adaptive optics
APD	avalanche photo diode
CCD	charge coupled device
CFHT	Canada France Hawaii telescope
CoM	centre of mass
DIMM	differential image motion monitor
DM	deformable mirror
ELT	extremely large telescope
E-ELT	European extremely large telescope
EMCCD	electron multiplication charge coupled device
ESO	european southern observatory
FA-SLODAR	full atmosphere slope detection and ranging
FFT	fast Fourier transform
FORS2	focal reducer and low dispersion spectrograph two
FSM	fast steering mirror
FWHM	full width at half maximum
G-tilt	global tilt
GL	ground layer
GLAO	ground layer adaptive optics
G-SCIDAR	generalised scintillation detection and ranging
IAC	Instituto de Astrofísica de Canarias
ING	Isaac Newton group
iSLODAR	interleaved slope detection and ranging
IFU	integral field unit
JKT	Jacobus Kapteyn telescope
L & A	learn and apply
LGS	laser guide star
LOLAS	low layer scintillation detection and ranging
LTAO	laser tomography adaptive optics
LuSci	lunar scintillometer
MASS	multi aperture scintillation system
MCAO	multi conjugate adaptive optics
MOAO	multi object adaptive optics
NGS	natural guide star
NOT	Nordic optical telescope
ORM	Observatorio del Roque de los Muchachos

OTP	optical turbulence profiler
PBL	planetary boundary layer
PSF	point spread function
SALT	South Africa large telescope
SCIDAR	scintillation detection and ranging
SH	Shack Hartmann
SIRFS	slope detection and ranging impulse response functions
SL	surface layer
SLODAR	slope detection and ranging
SODAR	sonic detection and ranging
S-SCIDAR	stereo scintillation detection and ranging
UT	unit telescope
VLT	very large telescope
VST	VLT Survey Telescope
WFS	wave front sensor
WHT	William Herschel telescope
Z-tilt	Zernike tilt

Aknowledgements

I would first like to thank my supervisor Dr. Wilson for his support and help over the four years of my PhD, and to thank Tim Butterley and James Obsorn for their continuing help and stimulating discussions.

I am privileged to have had the opportunity to work at many different observatories, and I would like to express my gratitude to the people and institutions that have offered me this opportunity. These trips would not have been anywhere near as productive and enjoyable without the travelling companions I have had the pleasure to work with, Richard W, Tim B, James O, Tim Morris (for letting me loose on the WHT) and Mark Harrison.

My time at Durham would not have been as enjoyable without my colleagues and office mates in 117; Fraiser, Kim, Ulrike, Sofia, Laura, Bart, Scott, and those in 127 and 125b.

During my PhD I restarted my rowing career, and this has bought a lot of enjoyment, and a huge sense of achievement, along with moments both sublime and ridiculous. The sense of camaraderie and friendship has greatly enriched my life. There are many people to thank, but I would like to mention a few here; Matt, Rox, Sweedish, Danny, FP, Dave, Rich, Andy, Sarah, Guy and Bill.

Special thanks must also go to my mother Eileen, for her support and encouragement in my academic endeavours, and for always being welcoming when I need to get away for a while.

Chapter 1

Introduction

1.1 Introducing the Thesis

When light from an astronomical object passes through the atmosphere, various physical processes distort and move the image, in a process known as *astronomical seeing*. As a result all ground based telescopes with no correction achieve an angular resolution no better than telescopes of only a few centimetres diameter. There is also a reduction in the central intensity of the star imaged by the telescope which can be two orders of magnitude or more, depending on the telescope diameter, wavelength, and strength of turbulence. The turbulence also results in intensity fluctuations in the image known as *scintillation*. With the aid of both active optics (to control the mirror shape to correct for flexure and thermal deformation), and Adaptive Optics (AO) to correct for the turbulence, fainter objects can be observed at a higher resolution than ever before [1].

Even using the most sophisticated AO systems today, 8 m telescopes are unable to reach their diffraction limit at visible wavelengths. At its simplest, an AO system consists of a sensor, a corrective mirror, and a control system. To increase the amount of correction tomographic techniques such as multi-conjugate AO (MCAO) can be used, in which multiple corrective mirrors are conjugate to different heights in the atmosphere. This requires detailed knowledge of the profile of the atmospheric turbulence (i.e. the distribution of turbulence strength as a function of height) [2]. If the ground layer of turbulence is strong, a large degree

of correction can be obtained over a large field of view by conjugating a single corrective mirror to the ground in a technique known as ground layer AO (GLAO).

With the current push towards telescopes with mirror diameters of over 30 metres, techniques such as MCAO and GLAO become even more crucial. In addition the telescope itself may be higher than the ground layer of turbulence. Significant amounts of turbulence may be present within the telescope, so the optical path may encounter the same patch of turbulence two or three times. Three of these large telescopes are currently planned,

- *European Extremely Large Telescope.* A 39 m telescope to be built by the European Southern Observatory located at Cerro Armazones in Chile.

- *Thirty Metre Telescope.* An American telescope to be located at the summit of Mauna Kea on Hawaii, run by a collaboration of Caltech, and the Association of Canadian Universities for Research in Astronomy.

- *Giant Magellan Telescope*, which instead of having a large segmented mirror like the two above will use seven 8.4 m mirrors, and have a resolving power equivalent to a 24.5 m telescope. This will be located at Las Campanas observatory in Chile.

As these projects are hugely expensive the sites must be chosen carefully, and part of this process involves a detailed understanding of the turbulence conditions. There are many different instruments that can be used to characterise turbulence parameters, and that are suitable for long long term site profiling campaign. In addition long term climate effects are present at certain observatory sites, most notably Cerro Paranal in Chile.

Studies show that atmospheric turbulence predominately occurs in three distinct regions, a Surface Layer (< 20 m), a ground layer (< 1000 m), and the free atmosphere where the turbulence can be distributed between 1 and 20 km. There are a variety of techniques to probe atmospheric turbulence, each of which has its own limitations. Two such techniques are SLOpe Detection And Ranging (SLODAR), and SCIntillation Detection And Ranging (SCIDAR), both of which are optical cross beamed techniques.

These methods and their application to current and future optical telescopes, form the subject of this thesis.

1.2 Thesis synopsis

- *Chapter 2* presents the background to the work presented in this thesis. The phenomenon of atmospheric turbulence is described, along with the mathematical framework used to describe the turbulence. Instruments used to measure the turbulence are discussed. The motivations for studying turbulence are discussed within the framework of adaptive optics. Finally the two instruments forming the work in the thesis are explained, specifically the crossed beams techniques SLODAR and SCIDAR.

- *Chapter 3* describes the simulation of atmospheric turbulence that is used in the work in chapters 4, 5 and 6. The methods and implementation are described, including the sampling limits to ensure the simulation is fit for purpose. The simulation is tested against theory, and the assumptions made are presented.

- *Chapter 4* presents an analysis of a modification to SCIDAR, Stereo Scidar, in which the pupil images from two stars each fall on separate CCD detectors, and can be conjugated to arbitrary heights. Response functions are calculated for this instrument, and the effect of re-conjugation to increase the altitude resolution of the method is shown from simulation. The effects of arbitrary atmospheric power spectra are discussed, and the results of an on sky demonstration are shown, including a seven layer turbulent atmosphere.

- *Chapter 5* calibrates SLODAR for the effects of Fresnel propagation in the atmosphere. Response functions are calculated using a semi-analytical method and compared with simulation. A technique to use the scintillation of Shack Hartmann spots in conjunction with the SLODAR autocovariance to fit high altitude turublence is explained and verified with simulation. This technique is applied to data from the SL-SLODAR at Paranal, and compared with the MASS, another turbulence profiler.

- *Chapter 6* first presents results from a SLODAR campaign at the ORM, and a comparison with DIMM, showing clear effects of both meteorology and topology on the seeing measurements, and optical turbulence profiles. Real world effects on the accuracy of SLODAR are discussed, as are the changing weather conditions at the two SLODAR

sites on La Palma, and at Paranal.

- *Chapter 7* presents my conclusions.

Chapters 2 and 3 contain preparatory material, placing the work in the thesis into a wider context, and describing the scientific background. Chapters 4, 5, and 6 contain new material by the author.

Chapter 2

Introduction and Theory

2.1 Optical Turbulence

The fundamental limiting angular resolution of an optical instrument with a circular aperture is given by

$$\theta = 1.22\frac{\lambda}{D} \tag{2.1}$$

where λ is the wavelength of light entering the instrument, and D is the aperture diameter [3]. The angle θ is defined as the angular radius of the first dark ring in the Airy diffraction pattern. Hence objects with a separation smaller than this angle can not be completely resolved. However the resolving power of telescopes with apertures greater than 10 to 20 cm when observing in the visible and near infra red parts of the spectrum is limited due to the effects of turbulence in the atmosphere.

Turbulence in the atmosphere mixes air of different temperatures, resulting in density variations which in turn causes the refractive index of the air to fluctuate. As light from the observed object passes through the atmosphere, these refractive index fluctuations cause aberrations. When the object is brought into focus by a telescope, the focussed image appears distorted as a result of fluctuations in the incident wavefront. This process of telescope images being degraded is known as "*seeing*". For major observatories the seeing angle (resolution limit due to the seeing), is typically between 0.5" and 2". To put this in

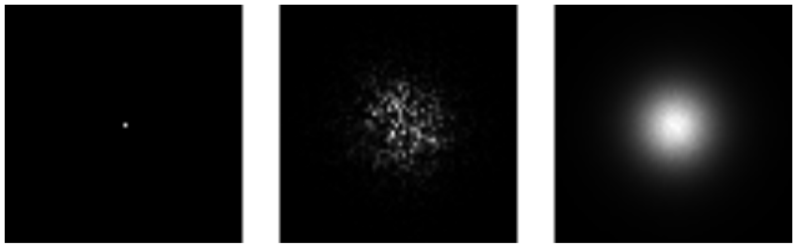

Figure 2.1: Figure illustrating the effects of atmospheric turbulence on a telescope PSF. The left hand image shows the diffraction limited PSF of the telescope, the centre image a short exposure, and the right hand image a long exposure. The data is simulated, with a 2 m telescope, and a Fried parameter of 10 cm. Note the random speckled PSF in the short exposure, and the smooth and approximately Gaussian PSF in the long exposure, many times wider than the diffraction limit. Each image has been scaled independently in intensity for clarity

perspective the diffraction limited resolution of a 4 m telescope at a wavelength of 500nm is 0.03". Figure 2.1 shows an example of a diffraction limited PSF, and the effects of atmospheric turbulence on both short and long exposures.

To assess the effect of atmospheric turbulence (and the impact of any correction performed), in practice the Strehl ratio is often measured. This is the ratio of the observed peak intensity for the measured PSF in the detection plane to the theoretical maximum peak intensity of the optical system working at its diffraction limit. This can be expressed by

$$S = \exp(-(2\pi\sigma/\lambda)^2), \tag{2.2}$$

where σ is the root mean square deviation of the wavefront, and λ the wavelength. The Strehl ratio for a perfect system is 1, however for $S \geq 0.8$, an observer is unable to separate the measured image from an ideal one [4].

2.1.1 Structure of the Turbulent atmosphere

The atmospheric turbulence considered in this thesis occurs in the troposphere, the name derived from the Greek *tropos* for "turning" or "mixing", referring to the fact that turbulent mixing has a key role in the structure and behaviour of this part of the atmosphere. The troposphere is the atmospheric layer from the ground up to approximately 20 km. The border between the troposphere and the next highest layer, the stratosphere, is known as

the tropopause. This is an inversion layer[1], and as such there is very little mixing between the two atmospheric layers.

In considering optical turbulence it is useful to divide the troposphere into three distinct regions. The first two are part of the Planetary Boundary Layer (PBL), where friction plays a large role in generating turbulence. The lowest region is the Surface Layer (SL), where friction from the topography causes turbulent eddies, and chaotic wind patterns to form. The surface layer extends to an altitude of $\sim$ 30 m. Above this, extending to an altitude of up to 1500 m is the Ground Layer (GL). This region is geostrophic, where the pressure gradient and Coriolis forces are balanced in the absence of friction. The friction of the ground still has effect, causing air to spiral into low pressure, as the frictional forces cause a reduction in the magintude of the Coriolis force. Above the PBL is the free atmosphere, where the effects of surface friction are negligible. The main contribution to turbulence in this region is wind shear.

In addition to the altitude structure of the turbulent atmosphere, there is often a distinct velocity structure linked to wind speeds. The free atmosphere turbulence has a high velocity often associated with the jet streams (up to 25 ms^{-1}) , and the ground layer turbulence moves much slower, usually below 13 ms^{-1}. Although not strictly atmospheric turbulence, turbulence can appear in telescope domes, and within the telescope tubes. These phenomena are known as dome seeing and tube seeing respectively. They have a much slower characteristic speed than genuine atmospheric turbulence, and often exhibit a different power spectrum.

2.1.2 Models of Turbulence

The refractive index fluctuations are caused by the mixing of air with differing temperatures and hence differing densities. As the refractive index is a function of air density, the turbulence creates a volume of varying refractive indices. Each of the variations themselves may be locally small, but the cumulative effect can be rather large, and hence parts of a wavefront propagating through this region receive a phase delay with respect to others. This leads to an aberration of the incoming wavefront. The phase effects are characterised by spatial power spectra, examples of three different cases are illustrated in figure 2.2. Atmospheric

[1] A region where atmospheric temperature increase with altitude.

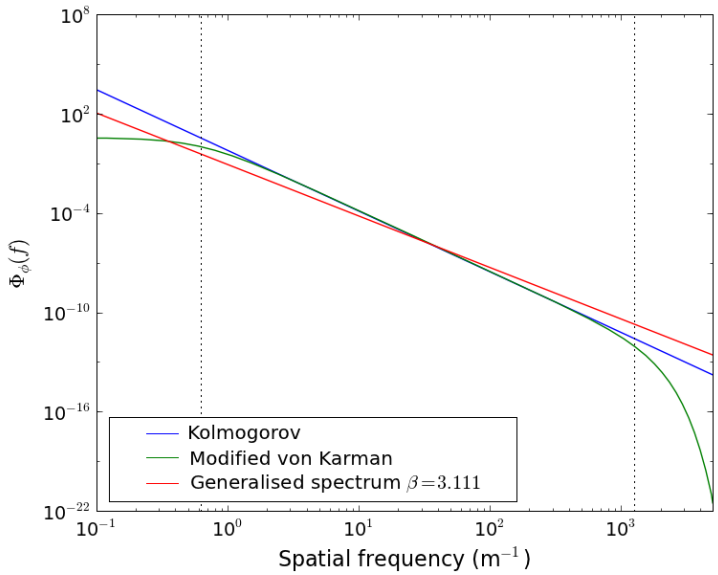

Figure 2.2: Figure showing a Kolmogorov, modified von Karman, and generalised power spectrum. The blue line shows the Kolmogorov spectrum ($\beta = 11/3$, and the red a generalised power spectrum with $\beta = 3.111$. This generalised turbulence will have more energy on smaller length scales, and less on larger scales when compared to the Kolmogorov case. The green line shows the modified von Karman spectrum. The power converges to zero at scales smaller than the inner scale due to the dissipation of the turbulence, and reaches an asymptote at the outer scale, as this corresponds to the largest spatial scale of turbulence in this model. The vertical dotted lines are the spatial frequencies for the inner and outer scale used for this plot (inner scale = 5 mm, and outer scale 10 m). The scaling on the y-axis is arbitrary, and is related linearly to the strength of the turbulence.

turbulence typically occurs in relatively thin layers (a few tens of metres at the thickest). These can be modelled as thin 'phase screens' at discrete altitudes.

Kolmogorov Model

The Kolmogorov model for atmospheric turbulence was proposed in 1941 [5] and after some development [6] remains the most commonly used model today. There are many summaries of the results [1,7,8], so only the key points will be presented here. As the refractive index of the atmosphere is inhomogenous, the wavefront of the light is distorted as it passes through. The model is a general turbulence model for a fluid, and assumes that energy enters the flow at low spatial frequencies i.e. on large spatial scales. These large spatial fluctuations can be characterised by their outer length scale L_0, which is the scale on which energy is

introduced to the system. In the case of the atmosphere this energy is introduced by solar heating. These fluctuations then break down into smaller and smaller structures within the turbulent flow, until they dissipate at a scale length known as the inner scale l_0. The range of values $[l_0, L_0]$ is known as the *inertial range*. Within this range energy is transferred, and dissipation due to viscosity is negligble. The distribution of the turbulence can be expressed using the power spectral density (PSD) $\Phi_n(f)$, where $f = 2\pi/x$, and x is a distance across the turbulence.

The fluctuations in the refractive index can be described by a structure function

$$D_n(r) = \left\langle \left| n(\boldsymbol{x}) - n(\boldsymbol{x}') \right|^2 \right\rangle \tag{2.3}$$

where $n(\boldsymbol{x})$ and $n(\boldsymbol{x}')$ are the refractive indices at the points $\boldsymbol{x}$ and $\boldsymbol{x}'$ in three dimensional space, $r = |\boldsymbol{x} - \boldsymbol{x}'|$, and the angular brackets represent an average over a large number of points. The spatial refractive index structure function for Kolmogorov turbulence is

$$D_n(r) = C_n^2(h)\, r^{2/3}. \tag{2.4}$$

where $C_n^2(h)$ is the refractive index structure parameter. This corresponds to the strength of turbulence. It must be noted however that this is only valid for $l_0 < r < L_0$. The corresponding power spectral density (PSD) of these refractive index fluctuations is

$$\Phi_n(f) = 0.033 C_n^2(h)\, f^{-11/3}. \tag{2.5}$$

In order to quantify the effects of propagation through turbulence on imaging, it is useful to consider the effects of optical phase propagation $\phi(\boldsymbol{r})$ within the telescope pupil (where $\boldsymbol{r}$ is a 2D vector). We introduce the 2D phase PSD and and the corresponding structure function for propagation through Kolmogrov turbulence;

$$\Phi_\phi(f) = 0.023 f^{-11/3} {r_0}^{-5/3} \tag{2.6}$$

and

$$D_\phi(\boldsymbol{r}) = 6.88\left(\frac{r}{r_0}\right)^{5/3} \tag{2.7}$$

where $f = 2\pi/r$, and r_0 is the Fried Parameter [9].

The Fried parameter allows the total strength of the turbulence to be characterised, and has the form

$$r_0 = \left(0.423k^2 \sec(\gamma) \int_0^\infty C_n^2(h)\,\mathrm{d}h\right)^{-3/5} \tag{2.8}$$

where γ is the zenith angle, and k is the wave number of the light ($k = 2\pi/\lambda$).

There are two physical interpretations of the Fried Parameter. The length can be thought of as the diameter of a circular aperture over which the optical phase distortion has a mean value of 1 rad, or alternatively as the maximum diameter of a telescope aperture that is diffraction limited.

The long exposure Full Width at Half Maximum (FWHM) of the seeing limited PSF is given by

$$s = 0.98\frac{\lambda}{r_0}. \tag{2.9}$$

It is useful to introduce the concept of *isoplanatism*, and define the *isoplanatic angle* as the angular separation at which the Strehl ratio falls to $1/e$ of the value obtained close to a reference star. This is a key concern for adaptive optics (section 2.2), where on axis science objects are corrected using off axis guide stars. For wider separations and higher turbulent layers the correlation of the aberrations between the two light paths will be lower. The isoplanatic angle can be defined in terms of the vertical turbulence distribution as

$$\theta_0 = \left(2.91k^2 \int_0^\infty C_n^2(h)\,h^{5/3}\mathrm{d}h\right)^{-3/5}. \tag{2.10}$$

This equation implies that for ground based telescopes, the effect of angular anisoplanatism is dominated by higher layer turbulence.

von Karman Turbulence

The outer scale of turbulence L_0 has been measured to be of the order of metres to tens of metres, which is of the same order as the size of the aperture of large telescopes [10].

Less image motion (angle of arrival variance) is observed in the image plane of a large telescope than predicted by the Kolmogorov model. L_0 can be measured by direct sensing of the wavefront on differing length scales, and fitting a model to the observations. It is therefore inappropriate to assume that the turbulence will obey the Kolmogorov model at these length scales. von Kármàn modified the Kolmogorov power spectrum to attenuate low spatial frequencies [11]. The PSD for the von Kármàn spectrum, and its corresponding structure function [12] are

$$\Phi_\phi(f) = 0.022883 {r_0}^{-5/3} \frac{{L_0}^{11/3}}{(1 + {L_0}^2 f^2)^{11/6}} \tag{2.11}$$

and

$$D_\phi(r) = 0.017253 \left(\frac{L_0}{r_0}\right)^{5/3} \left[1 - \frac{2\pi^{5/6}}{\Gamma(5/6)} \left(\frac{r}{L_0}\right)^{5/6} K_{5/6}\left(2\pi \frac{r}{L_0}\right)\right] \tag{2.12}$$

where K is a modified Bessel function of the second kind. There also exists a modified von Kármàn spectrum, which includes the effect of the inner scale. This is important if atmospheric scintillation is to be considered.

Generalised Turbulence Spectrum

A second alternative to the Kolmogrov model is a generalised power spectrum proposed by Nicholls *et al.*. This generalised spectrum does not assume the same power law as the Kolmogorov model [13]. The PSD is given by

$$\Phi_\phi(f) = \frac{A_\beta f^{-\beta}}{{\rho_0}^{\beta-2}} \qquad (2 < \beta < 4) \tag{2.13}$$

where β is the exponent for the power law, $\rho_0 \equiv r_0$, and the constant A_β is chosen so the wavefront variance across a pupil of diameter equal to ρ_0 is 1 rad^2 (after piston subtraction). The value for this constant is [14]

$$A_\beta = \frac{2^{\beta-2}[\Gamma(\frac{\beta+2}{2})]^2 \Gamma(\frac{\beta+4}{2}) \Gamma(\frac{\beta}{2}) \sin(\pi \frac{\beta-2}{2})}{\pi^\beta \Gamma(\beta+1)}, \tag{2.14}$$

and the corresponding form for the structure function is

$$D_\phi(r) = \gamma_\beta \left(\frac{r}{\rho_0}\right)^{\beta-2} \tag{2.15}$$

where γ_β is a constant which allows consistency between the power spectrum and structure function [15]. This constant is defined as

$$\gamma_\beta = \frac{2^{\beta-2}[\Gamma(\frac{\beta+2}{2})]^2\Gamma(\frac{\beta+4}{2})}{\Gamma(\frac{\beta}{2})\Gamma(\beta+1)}. \tag{2.16}$$

2.1.3 Propagation of Light Through Atmospheric Turbulence

When an optical field propagates through atmospheric turbulence, the variations of the refractive index will cause perturbations of the phase and complex amplitude of such a field. Considering an observer on the ground, viewing a star at the zenith, and by assuming the light waves arriving from the star are both planar and monochromatic, they can be represented mathematically as

$$U(\boldsymbol{x}) = A\exp(i\phi_0) \tag{2.17}$$

where U is the optical field, $\boldsymbol{x}$ is a 2-d position in the field, and A, and ϕ are the amplitude and phase of the field respectively. This can be generalised to an arbitrary field at altitude h, by allowing vertical variation of both the complex amplitude and the phase

$$U_h(\boldsymbol{x}) = A_h(\boldsymbol{x})\exp(i\phi_h(\boldsymbol{x})) \tag{2.18}$$

Propagation through a turbulent layer

We assume that the atmospheric turbulence is made up of thin layers of thickness δh, chosen such that the thin screen approximation holds [8]. The turbulent layer acts as a phase screen, and as such only causes phase variations of the optical field, rather than any intensity variations. For one such layer, located between h and $h+\delta h$, the phase shift $\Delta\phi(\boldsymbol{x})$ caused by the random variations of the refractive index $n(\boldsymbol{x}, h)$ is

$$\Delta\phi(\boldsymbol{x}) = k\int_h^{h+\delta h} n(\boldsymbol{x}, z)\,\mathrm{d}z \tag{2.19}$$

where k is the wave number. Consider an optical field encountering this layer, and propagating from altitude $h + \delta h$ to h, the field at $h + \delta h$ can be given by equation 2.18, and the optical field at h by

$$\begin{aligned} U_h(\boldsymbol{x}) &= A_{h+\delta h}(\boldsymbol{x}) \exp\left(i\phi_{h+\delta h}(\boldsymbol{x}) + i\Delta\phi(\boldsymbol{x})\right) \\ &= U_{h+\delta h}(\boldsymbol{x}) \exp\left(i\Delta\phi(\boldsymbol{x})\right) \end{aligned} \tag{2.20}$$

Free space propagation

After encountering a turbulent layer in the atmosphere the phase distortions then propagate to the ground. As the optical wavelengths used are much smaller than the smallest observed wavefront perturbations, we can use Fresnel propagation (see [3, 8, 16]). If we assume the turbulent layer in the section above was the only one present in the atmosphere, then the complex field a distance z from the turbulent layer is given by the convolution (denoted $\otimes$)

$$U_{h-z}(\boldsymbol{x}) = U_h(\boldsymbol{x}) \otimes K(\boldsymbol{x}, z) \tag{2.21}$$

where $K(\boldsymbol{x}, z)$ is the *Fresnel propagation kernel*, which is equivalent to the point spread function of Fresnel propagation, and is defined for a propagation distance z as

$$K(\boldsymbol{x}, z) = \frac{1}{i\lambda z} \exp(ikz) \exp\left(\frac{i\pi |\boldsymbol{x}|^2}{\lambda z}\right) \tag{2.22}$$

2.1.4 Effect of propagation on the phase power spectrum

Recall that the power spectrum for Kolmogorov turbulence was defined in equation 2.11. Optical propagation affects the properties of the power spectrum at the ground. These effects are fully documented by Roddier [8] and Dravins *et al.* [17–19]. The key parts are presented below, to explain the modified power spectra for both phase and complex amplitude that are required for the work presented here. In this treatment, the following assumptions are made: there is an atmosphere containing one thin turbulent layer at altitude (h), with thickness

(δh) and the phase fluctuations due to this layer are much less than one, ie

$$\Delta\phi\left(\boldsymbol{x}\right) \ll 1. \tag{2.23}$$

This criteria is known as the *small perturbation approximation*. Assume the incident field onto this turbulent layer has a value of unity, then the field at the layer output can be approximated to

$$U_h\left(\boldsymbol{x}\right) \simeq 1 + \Delta\phi\left(\boldsymbol{x}\right), \tag{2.24}$$

then the complex field after propagation distance z becomes,

$$U_{h-z}\left(\boldsymbol{x}\right) = 1 + \Delta\phi\left(\boldsymbol{x}\right) \otimes K\left(\boldsymbol{x}, z\right). \tag{2.25}$$

Define a complex quantity $\epsilon = \Delta\phi\left(\boldsymbol{x}\right) \otimes K\left(\boldsymbol{x}, z\right)$, so the real part $\chi\left(\boldsymbol{x}\right)$ describes the relative fluctuation of the amplitude, and the imaginary part $\phi_0\left(\boldsymbol{x}\right)$ the phase.

$$\chi\left(\boldsymbol{x}\right) = \Delta\phi\left(\boldsymbol{x}\right) \otimes \frac{1}{\lambda h}\cos\left(\frac{\pi\left|\boldsymbol{x}\right|^2}{\lambda z}\right) \tag{2.26}$$

$$\phi_0\left(\boldsymbol{x}\right) = \Delta\phi\left(\boldsymbol{x}\right) \otimes \frac{1}{\lambda h}\cos\left(\frac{\pi\left|\boldsymbol{x}\right|^2}{\lambda z}\right) \tag{2.27}$$

Using the convolution theorem, and the standard result for the Fourier transform of a Gaussian function, the fourier transforms of ϵ, χ, and ϕ_0 are

$$\mathfrak{F}\left(\epsilon\right) = \mathfrak{F}\left(\Delta\phi\right) i \exp\left(-i\pi\lambda z\left|\boldsymbol{f}\right|^2\right) \tag{2.28}$$

$$\mathfrak{F}\left(\chi\right) = \mathfrak{F}\left(\Delta\phi\right) \sin\left(\pi\lambda z\left|\boldsymbol{f}\right|^2\right) \tag{2.29}$$

$$\mathfrak{F}\left(\phi_0\right) = \mathfrak{F}\left(\Delta\phi\right) \cos\left(\pi\lambda z\left|\boldsymbol{f}\right|^2\right). \tag{2.30}$$

By rewriting the power spectrum for the phase in terms of the single layer, and the atmospheric turbulence contained in that layer, the power spectrum of the fluctuations of

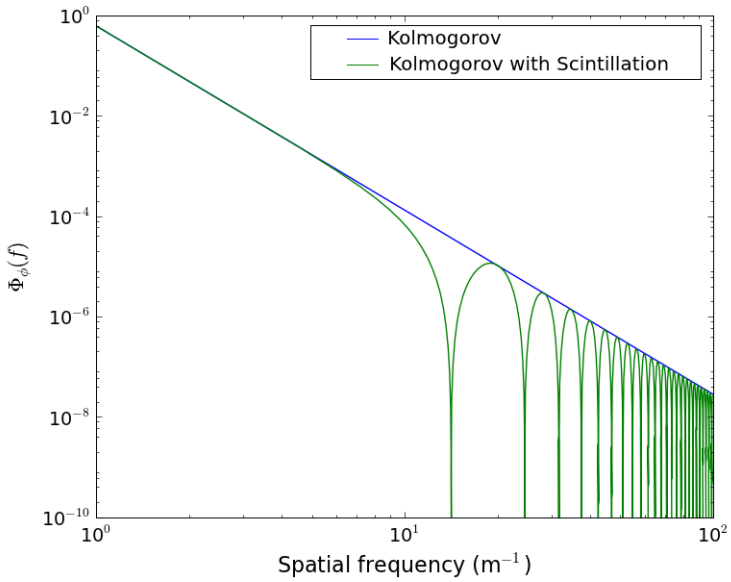

Figure 2.3: Kolmogorov phase power spectrum with and without the modification for atmospheric scintillation propagation (Fresnel propagation). The example shown has r_0 of 14 cm, a layer altitude of 5000 m, and a wavelength 500 nm.

intensity and phase for the free atmosphere propagation are

$$W_\chi(\boldsymbol{f}) = 9.7\times10^{-3}k^2\boldsymbol{f}^{-11/3}C_n^2(h)\,\delta h\sin^2\left(\pi\lambda z\left|\boldsymbol{f}\right|^2\right) \tag{2.31}$$

$$W_{\phi_0}(\boldsymbol{f}) = 9.7\times10^{-3}k^2\boldsymbol{f}^{-11/3}C_n^2(h)\,\delta h\cos^2\left(\pi\lambda z\left|\boldsymbol{f}\right|^2\right). \tag{2.32}$$

The modified phase power spectrum for Kolmogorov turbulence is shown in figure 2.3, for a layer altitude of 5000 m, with $r_0 = 14$ cm, and using a wavelength of 500 nm. The suppression of spatial frequencies corresponding to discrete multiples of the layer's Fresnel length can clearly be seen.

Effect of more than one layer

When multiple layers are considered the fluctuations at the ground add linearly, as the fluctuations can be assumed to be statistically independent. We can simply integrate equations

2.31 and 2.32 to give

$$W_{\chi}(\boldsymbol{f}) = 9.7 \times 10^{-3} k^2 \boldsymbol{f}^{-11/3} \int_0^{\infty} C_n^2(h) \sin^2\left(\pi \lambda z |\boldsymbol{f}|^2\right) \mathrm{d}h \tag{2.33}$$

$$W_{\phi_0}(\boldsymbol{f}) = 9.7 \times 10^{-3} k^2 \boldsymbol{f}^{-11/3} \int_0^{\infty} C_n^2(h) \cos^2\left(\pi \lambda z |\boldsymbol{f}|^2\right) \mathrm{d}h \tag{2.34}$$

A statistical representation of scintillation

Scintillation effects are measured as fluctuations of intensity on a telescope detector. By assuming the power spectrum of the phase is approximately equal to that of the fluctuations in complex amplitude, we can make the near field approximation by assuming Fresnel diffraction. The complex amplitude at the ground can be represented by

$$U_0(\boldsymbol{x}) = 1 + \chi(\boldsymbol{x}) + i\phi_0(\boldsymbol{x}) \tag{2.35}$$

and neglecting any terms above first order, the intensity is

$$I(\boldsymbol{x}) = |U_0(\boldsymbol{x})|^2 \simeq 1 + 2\chi(\boldsymbol{x}). \tag{2.36}$$

The relative fluctuations of the intensity are described by the term $2\chi(\boldsymbol{x})$. If a quantative measurement of scintillation strength is required, the normalised variance of the intensity is often used. This is known as the *scintillation index*, and is defined as

$$\sigma_I^2 = \frac{\langle \langle I \rangle - I \rangle^2}{\langle I \rangle^2} \tag{2.37}$$

where the angled brackets denote an ensemble average. Using equation 2.36, the power spectrum of the intensity fluctuations $W_I(\boldsymbol{f})$ is related to that of the amplitude fluctuations by

$$W_I(\boldsymbol{f}) = 4W_{\chi}(\boldsymbol{f}). \tag{2.38}$$

By substituting equation 2.33 and integrating over frequency $\boldsymbol{f}$, we arrive at an expression for the scintillation index

$$\sigma_I^2 = 19.12\lambda^{7/6} \left(\cos\gamma\right)^{11/6} \int_0^\infty h^{5/6} C_n^2 \left(h\right) \mathrm{d}h \tag{2.39}$$

where γ is the zenith angle. This is known as the Rytov approximation. From this expression it can clearly be seen that the scintillation index depends on wavelength as $\lambda^{7/6}$, and layer height $h^{5/6}$.

2.1.5 Measuring Atmospheric Turbulence

Direct Measurement

Early methods to measure the vertical distribution of atmospheric turbulence used microthermal sensors suspended from weather balloons [20, 21]. The balloon is released and will ascend to a height of approximately 25 km, measuring the temperature variations as a function of altitude. This method measures the temperature structure parameter C_T^2, rather than C_n^2. The two can be related providing a hypothesis of Kolmogorov turbulence is used. This method is effective for site testing, but is impractical for long term monitoring, or for providing real time support for existing observatories.

Differential Image Motion Monitor (DIMM)

The DIMM calculates the Fried parameter from the differential image motion between two apertures. This is commonly achieved by masking a telescope aperture to give two smaller apertures. Because the differential image motion is measured, the results are rendered insensitive to common motion such as tracking errors or wind shake of the telescope. By taking the variance of this differential image motion, r_0 (and hence the seeing angle) can be calculated, assuming a Kolmogorov turbulence model [22]. The DIMM was developed by ESO for the site selection campaign for the VLT, and is now a common site monitoring instrument at observatories around the world.

The DIMM can not determine the turbulence as a function of height.

Multi Aperture Scintillation System (MASS)

The MASS is a low cost turbulence profiler. It uses a small (14 cm) telescope, and measures the scintillation of a single star through a series of concentric annular apertures, and a circular central aperture. The incident intensity is measured, and the scintillation index is calculated for each of the apertures. As it measures scintillation, the MASS is blind to low altitude turbulence, however at many observatories the MASS and DIMM are combined to give a hybrid instrument known as a MASS-DIMM. The inability of the MASS to measure low altitude turbulence arises from the fact that stellar scintillation requires Fresnel propagation to develop, in the case of MASS at ~ 0.5 km for a measurable signal. This allows the strength of ground layer turbulence to be determined by calculating the difference between the integrated C_n^2 measured by the MASS and the DIMM [23]. The MASS has quite a coarse non-linear response, for example the ESO MASS provides turbulence strength estimates for 6 bins, centred at $h = 0.5$, 1, 2, 4, 8, and 16 km, with a resolution of $h/2$. The nature of the MASS response is discussed further in section 5.4.2.

Other Instruments

There are optical turbulence profilers that do not measure point sources. The Lunar Scintillometer (LuSci) measures scintillation of the moon using photodetectors to provide a profile of the surface layer of turbulence. Extended sources produce a large light cone, averaging out the effect of high altitude turbulence and causing the signal to be dominated by the surface layer [24]. This extended source profiling was first demonstrated by Beckers, measuring the surface layer for solar astronomy using the SHABAR instrument [25].

In addition to using optical techniques, it is possible to use sound to measure turbulence in the lower atmosphere. Doppler sonic detection and ranging (SODAR) is an acoustic radar technique used in applications outside astronomy (for example at airports, and wind farms). Crescenti reviews different applications of the technique [26]. As for the balloon measurement technique SODAR measures C_T^2 rather than C_n^2.

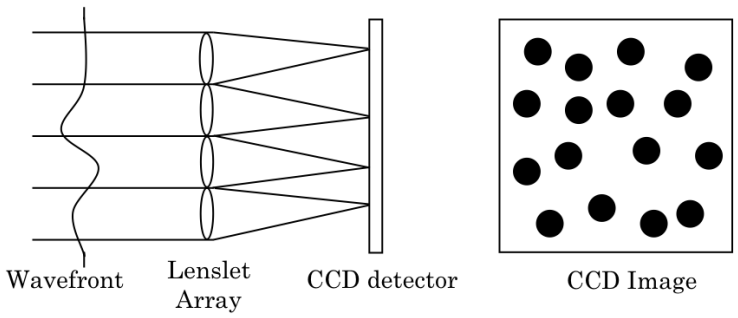

Figure 2.4: Figure illustrating a Shack Hartmann wavefront sensor. A distorted wavefront is incident on a lenslet array forming spots on a CCD detector. The distortion leads to the spots moving off axis, the amplitude of this motion is proportional to local wavefront slopes.

2.2 Adaptive Optics

We now summarise the main components of astronomical adaptive optics, to contextualise the discussion of optical turbulence, and turbulence profilers.

2.2.1 Wavefront Sensing

A wavefront sensor measures either the phase gradient or the phase curvature across a wavefront. There are many types of wavefront sensor, and three common ones are described below.

Shack Hartmann wavefront sensor

The Shack-Hartnann wavefront sensor consists of an array of lenslets, typically placed at the optical conjugate of the telescope aperture. A flat wavefront incident on these lenslets will create a uniform array of spots in the image plane. If the incident wavefront is distorted then the spot positions will deviate from the uniform pattern [27]. The amplitude of this deviation is proportional to the wavefront phase gradient across each lenslet. This is illustrated in figure 2.4. Measuring the centroid deviations of the spots from their centre positions allows a map of phase gradient to be constructed for the telescope pupil. This map of phase gradients can then be used to reconstruct the phase map of the wavefront. This is the wavefront sensor used on all SLODAR systems described in this thesis.

The centroids for the SLODAR use a simple centre of mass (CoM) algorithm. Consider

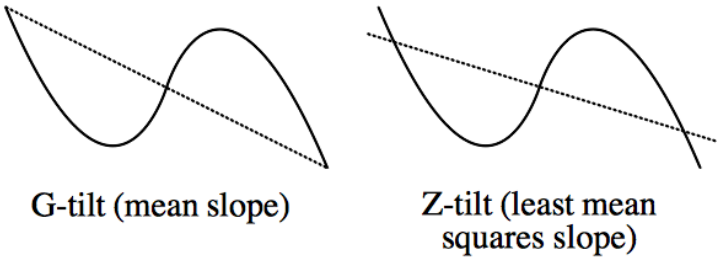

Figure 2.5: Figure illustrating Global and Zernike tilts. We show the wavefront across a Shack Hartmann subaperture and the G-tilt measuring the mean slope, and the Z-tilt measuring the least mean squares slope (in effect a best fit to the wavefront). Tokovinin states that an aggressively thresholded and windowed centroid measures a Z-tilt [29].

one subaperture of the wavefront sensor. If $I(x, y)$ is the background subtracted intensity pattern then the centroid in the x-direction, $\hat{x}$ is expressed as

$$\hat{x} = I_{\text{tot}}^{-1} \sum_{x,y} xI(x, y). \tag{2.40}$$

where I_{tot} is the total intensity in the subaperture. This yields a measurement for the angle of arrival fluctuation known as global tilts (G-tilts). [28]. However this only measures optimum centroids for Gaussian image profiles, with shot noise, but in the absence of any other noise. In practice however, for a square subaperture the image profile is shaped like a sinc function, and noise contributions from the detector and residual background are present. To combat this instruments that require the measurement of an image centroid, for example SLODAR and the DIMM, apply either one or both of *thresholding* or *windowing*. For thresholding, a certain threshold value is subtracted from the subapertue intensity, and the centroid is calculated from the resulting non negative pixels. Using the windowing method only a certain number of pixels around the image centre (often taken as the brightest pixel) are taken into account. Tokovinin analyses in detail the effect of these two methods on the centroids [29], and only a key result is presented here. With thresholding and windowing G-tilts are no longer measured, and instead the image motion measured is the Zernike tilt (Z-tilt), defined as the normal to a plane that best fits the wavefront distortion. An illustration of the two tilts are shown in figure 2.5.

Other wavefront sensors

A curvature wavefront sensor measures defocused images of the telescope pupil, before and after the focus position. The image before focus is the *intrafocal* image, and the one post focus is the *extrafocal* image. The intrafocal image is brighter in regions with a positive curvature, and darker in regions with negative curvature. This is reversed in the extrafocal image [30]. The aim for the corrective system is then to make both images flat. To improve noise performance in practical systems, the images are binned, and the intensity of each bin is measured using an avalanche photodiode (APD) [31].

In a pyramid wavefront sensor the incoming light is focussed on to the apex of a square pyramid. The pyramid oscillates perpendicular to the optical axis, leading to the formation of four pupil images on a detector. By measuring the relative intensities of these images, a map of wavefront slopes across the pupil can be made [32]. In reality a fast steering mirror (FSM) is often used to move the optical beam across the pyramid, rather than oscillating the pyramid itself. An intrinsic advantage of this system is the telescope aperture is not divided as with a SH WFS, and so this increases sensitivity, especially as the wavefront is corrected.

SLODAR uses a Shack Hartmann sensor for practical reasons. In addition to being relatively low cost, they have no moving parts and can be mounted on the back of small telescopes. The SLODAR instruments are often required to operate independently in varied weather conditions with a high degree of reliability, and a simple wavefront sensor facilitates this.

Zernike representation of wavefronts

An aberrated wavefront across a circular pupil can be represented by a sum of basis fuctions, each with their own weighting. These basis functions are known as *Zernike polynomials*, and are orthogonal on the unit disk [33]. A sum of these functions can be fitted to wavefront sensor data to provide a mathematical representation of the wavefront. This process will not be performed in the work in this thesis, however mention will be made of some lower order Zernike modes. They are grouped by radial frequency n, and have even and odd forms, the

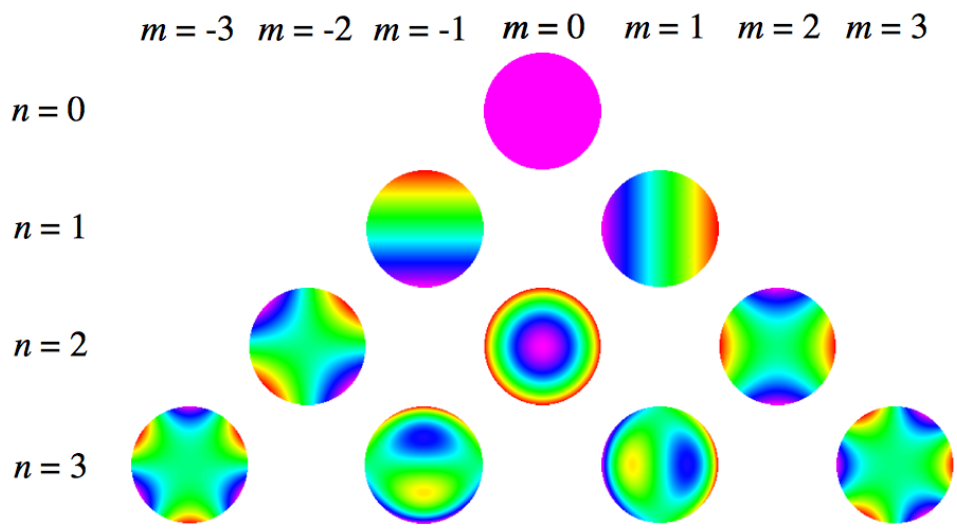

Figure 2.6: Figure illustrating the first 4 radial modes of Zernike Polynomials. This includes examples of Piston ($n = 0$), tip and tilt ($n = 1$), defocus ($n = 2, m = 0$), astigmatism ($n = 2, m = \pm 2$), and coma ($n = 3, m = \pm 1$).

even are defined as

$$Z_n^m(r,\theta) = N_n^m R_n^m(r)\cos(m\theta) \tag{2.41}$$

and the odd as

$$Z_n^{-m}(r,\theta) = N_n^m R_n^m(r)\sin(m\theta) \tag{2.42}$$

where m represents the angular frequency. Both m and n are non–negative integers, θ the azimuthal angle, and r is the radial distance across the unit disc. N_n^m is a normalisation constant, defined

$$N_n^m = \sqrt{\frac{2(n+1)}{1+\delta_{m,0}}} \tag{2.43}$$

where $\delta_{m,0}$ is the Kronecker delta function. We can define the radial component $R_n^m(r)$,

$$R_n^m(r) = \sum_{s=0}^{(n-m)/2} \frac{(-1)^s (n-s)!}{s![(n+m)/2-s]![(n-m)/2-s]!} r^{n-2s}. \tag{2.44}$$

The first four radial modes are shown in figure 2.6. In the thesis we make reference to several named low order zernike polynomials.

- *Piston* (Z_0^0) describes a constant phase across the telescope pupil. As this does not

involve a change in the wavefront slope, piston can not be measured by a Shack-Hartmann wavefront sensor.

- *Tip and Tilt* (Z_1^{-1}, Z_1^1) describe a constant slope across the pupil. In the case of a SHWFS this would result in all the spots having the same displacement. Tip and tilt can be induced by a motion of the telescope, for example by wind shake.

- *Defocus* (Z_2^0) describes the aberration resulting from a defocus of the optical system.

The higher order Zernike modes provide descriptions for other common aberrations, for example Coma, Astigmatism, and Spherical aberration.

2.2.2 Wavefront Correctors

The wavefront corrector alters the shape of an incoming wavefront to remove aberrations. In most astronomical AO systems, this consists of two components. The first is a flat Fast Steering Mirror (FSM), which tilts in the x and y directions to remove the tip-tilt components of the aberration, and correcting image motion. The higher order aberrations are removed using a deformable mirror (DM).

The two common types of DM are segmented DMs, and face-sheet DM's. A segmented DM is a mirror made of many small flat mirror segments mounted on actuators which allow each segment to move independently. Depending on the mirror they can have differing degrees of freedom: (1) Piston, (2) Tip - Tilt, (3) Piston, Tip, Tilt. The higher the number of degrees of freedom, the better will be the approximation to the wavefront shape, and hence a reduction in the 'fitting error'. A face-sheet DM has a flexible single mirror, supported by piston actuators allowing the overall shape of the mirror to be altered.

There are other types of wavefront correctors, for example liquid crystal devices, however they are not used in astronomical AO [34].

2.2.3 Wavefront Reconstruction

Generally AO systems operate in a 'closed loop' configuration, meaning that the wavefront sensor is placed after the corrector in the optical path. This means that the aberration

sensed is the residual error after the wavefront has been corrected, and the problem of reconstruction can be assumed to be linear.

The reconstruction of a wavefront from the WFS, and the determination of the control signals required for the DM are commonly combined into a single mathematical operation, defined by the matrix equation

$$\boldsymbol{x} = \mathbf{M}\boldsymbol{s} \tag{2.45}$$

where $\boldsymbol{x}$ is a vector of WFS measurements, $\boldsymbol{s}$ a vector of the control signals sent to the DM, and $\mathbf{M}$ is the "control matrix". In the simplest case (for a SH WFS and a face-sheet DM), this control matrix is generated from a "poke matrix" $\mathbf{B}$, which is a matrix that satisfies

$$\boldsymbol{s} = \mathbf{B}\boldsymbol{x}. \tag{2.46}$$

Each of the DM's actuators in turn is 'poked' (set to known displacements) in the absence of turbulence, and the resulting WFS measurement vectors are assembled into the poke matrix. The simplest control matrix is the pseudo-inverse of the poke matrix. By generating the pseudo-inverse using singular value decomposition, any poorly sensed modes which will worsen system performance can be removed. For ELTs and complex AO systems, which are generally either high order or include multiple WFSs and DMs, this method of matrix inversion may become intractable as a matrix inversion is required. As the matrix to invert becomes larger the computational time required to perform the inversion increases non linearly. Sparse matrix techniques have been proposed to reduce the scale of the inversion [35].

A recent development has been a method known as Learn and Apply (L & A), which has been successfully demonstrated with Canary [36,37], an open loop multi object adaptive optics system. This system includes a SLODAR optical turbulence profiler and so includes the turbulence profile within the reconstruction. The covariance matrices between the slopes of each guide star are calculated, and also the covariance between the guide stars and an on axis "calibration" WFS. When the covariance matrices are combined, the turbulence profiles and geometric positions of each guide star can be taken into account in the reconstructor. The matrices therefore need to be recalculated if the turbulence profile changes during

the course of operation. However as the system operates in open loop, the profile can be monitored from internal measurements allowing the covariance matrices to be updated. As the on axis calibration WFS is not available during observing, the on axis path aberrations must be reconstructed using the off axis guide stars, using the covariance matrices and knowledge of the guide star geometry [38].

It is also possible to use artificial neural networks (ANN) for open loop systems to perform on axis correction from off axis WFS data. These ANNs are "trained" by providing them with combinations of input WFS data, along with a desired output. This training can be performed either with on sky data [39], or with data from simulation [40].

2.2.4 Laser Guide Stars

Laser guide stars provide a means to increase the sky coverage of an AO system. A laser beam is projected into the atmosphere, forming a bright "beacon" in the direction of the science target [41]. Two different types of Laser Guide Stars are in use; Rayleigh beacons [42], and sodium LGS [43].

A Rayleigh beacon has a laser focussed at a point in the atmosphere above the telescope, at an altitude between 10 and 20 km. The laser light scatters off air molecules (Rayleigh scattering), and the scattered photons are collected by the telescope and measured by the wavefront sensor. A pulsed laser with range gating detection ensures that only the photons scattered from altitudes near the focal point are measured. The limiting altitude is due to the drop in return signal for increasing beacon height.

Sodium guide stars are generated with a laser of wavelength 589 nm, which excites a layer of sodium ions in the upper atmosphere ($\sim$ 90 km). This high altitude beacon reduces the effect of focal anisoplanatism and allows a larger fraction of the atmosphere to be sampled. Using the sodium layer removes the need for a range gated detector, so that a continuous laser can be used. The sodium layer however has a non-uniform distribution, which in some cases can lead to phenomena such as "double spots" in the wavefront sensor. By launching the sodium guide star from behind the secondary mirror, the effects of the Rayleigh scattering in the lower atmosphere can be obscured.

Laser guide stars can not provide a measurement for the global tip-tilt aberration over

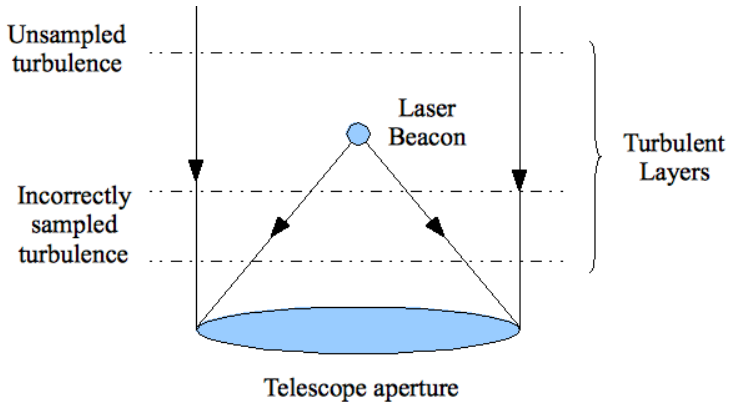

Figure 2.7: Figure illustrating focal anisoplanatism. The natural guide star can sample the whole atmosphere, whereas the laser guide star only samples a cone up to some maximum height. This means some very high altitude turbulence will may not be sensed, and the turbulence outside the laser cone will not be sampled either. This effect can be mitigated by using multiple laser guide stars across the whole aperture.

the telescope pupil, as the laser measurement has a contribution to tip-tilt error on both the upward and return path of light through the atmosphere. Generally laser guide star adaptive optics requires a natural guide star for tip-tilt correction. This measurement can be done with a very low order wavefront sensor, so that dim guide stars can be used, and there is still a huge improvement in sky coverage when compared to natural guide star adaptive optics.

One of the major limitations of an LGS is focal anisoplanatism (FA), commonly known as the "cone effect". A natural guide star samples a cylindrical volume of atmosphere as the light is planar by the time it reaches the top of the Earth's atmosphere. On the other hand an LGS samples a cone, as the source is not at an infinite distance. This has the implication that there is turbulence that the light from a science object will pass through that an LGS can not measure, as illustrated in figure 2.7. This problem becomes worse for a lower beacon, higher altitude turbulence, and larger telescope diameters.

A second limitation is spot elongation. The laser beacon is an extended column of light in the atmosphere, meaning that when observed from some distance away from the launch axis the beacon is elongated. This is a problem which becomes more severe for larger diameter telescopes and for lower altitude beacons. Sodium beacons therefore suffer less from this problem than Raleigh beacons. The diameter of ELTs is large enough however that spot elongation becomes a serious problem even for sodium beacons. A simple approach

to mitigate this problem is to use a shorter range gate, at the expense of reducing back scattered light. Hence the laser power must be increased, or the beacon must be focussed at a lower altitude (increasing the effects of FA). It is possible to use more complicated methods to correct this problem, for example launching multiple beams from around the aperture of the telescope, and allowing these beams to focus and combine at the same point [44]. Sodium guide stars also introduce another problem, in that the shape of sodium beacons depend strongly on the distribution of the sodium in the upper atmosphere, which is some cases is bimodal, which presents a challenge for accurately determining the centroids of the spots [45].

2.2.5 Multi-Object Adaptive Optics (MOAO)

MOAO is designed to correct simultaneously for a large number of science objects each with a small angular size, spread over a wide field of view. One DM per object is placed in the optical train feeding an Integral Field Unit (IFU). These science objects are commonly too faint for a measurement of the optical turbulence to be made directly. Multiple guide stars in the wide field are used to measure the effects of the turbulence. A tomographic approach is then used to reconstruct a 3-d turbulence volume above the telescope, and the correction for an individual science object is made by projecting along the direction for that object. A knowledge of the turbulence profile is required for the algorithm used to construct the turbulent volume. This technique was demonstrated on sky using the CANARY instrument [37], and is the method proposed for EAGLE, a MOAO IFU spectrograph currently being designed as a potential instrument for the E-ELT [46].

2.2.6 Ground Layer Adaptive Optics (GLAO)

GLAO is possibly the simplest modification of a classical Adaptive Optics system. As the name suggests, this system corrects only for the lowest layer of turbulence, giving poorer performance, but a much larger corrected field of view. The simplest implementation of a GLAO system uses multiple natural guide stars around the science field, and observe each with a dedicated wavefront sensor. The light from each guide star passes through the same turbulence at the ground, but different turbulence at high altitudes. The signals are

averaged, resulting in the high altitude turbulence being averaged out, and the common low layer turbulence preserved.

2.2.7 Multi-Conjugate Adaptive Optics (MCAO)

A more complex development is MCAO, which uses the same guide star arrangement as GLAO, but with multiple Deformable Mirrors. The wavefront is measured in multiple directions, and reconstructed to provide both the shapes and altitude of the optical aberrations, in essence providing a 3-D map of the turbulence. The DM's are conjugated to different altitudes, and the aberrations are corrected using the most appropriate DM.

2.2.8 Implications for turbulence profiling

Surface Layer: Height versus telescope

GLAO is only effective if there is a strong low layer of atmospheric turbulence that is visible to the telescope. Strong surface layer turbulence is seen in every observatory site where a turbulence profiling campaign has been carried out. Due to the size of large telescopes, the primary mirror sits some distance off the ground, for the VLT's this height is $\sim$10 m, and the top of the dome has a height of approximately 30 m. At Cerro Paranal the surface layer of turbulence has been measured to have an average scale height of 11 m [47], and by assuming an exponential decay of the turbulence strength 63% of the turbulence strength (in the surface layer) lies below 10 m, and 95% lies below 30 m. This implies that the VLTs are above much of the surface layer. Preliminary SODAR studies show Cerro Armazones (the site for the E-ELT) has similar surface layer parameters as Paranal [48], and so it is likely that the E-ELT primary mirror (at a height of 30 m) will sit above this turbulence. This implies a need to resolve the surface layer to a resolution of 5-10 metres to gain understanding of the turbulence the telescope is likely to see, and ideally there would be multiple measurements around the site as the properties of the surface layer can change from one side of a site to the other.

There are also cases where a telescope will see no ground layer turbulence. In 2009 the author took part in an experiment involving deploying a SLODAR instrument on the WHT

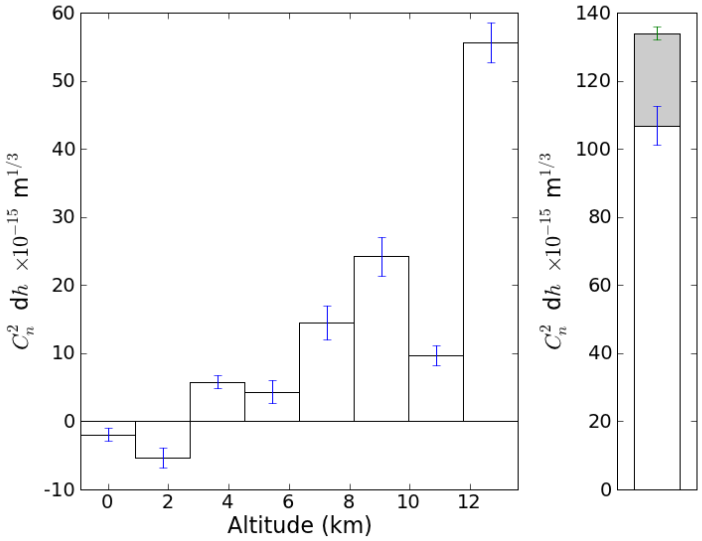

Figure 2.8: SLODAR turbulence profile measured from the WHT, on May 6$^{\text{th}}$ 2009. The left hand plot shows the resolved turbulence profile, showing two turbulent layers. The right hand plot shows the integrated turbulence, with the integrated resolved turbulence in white, and unresolved turbulence in grey. There is no surface or ground layer turbulence observed in this profile, suggesting the telescope dome shields the telescope in this case.

(section 2.3), for part of which there was no surface or ground layer turbulence measured, and an example profile is shown in figure 2.8. La Palma is known for having strong turbulence at the ground, and the hypothesis is that the telescope dome itself shields the telescope from the surface layer. This could potentially be confirmed and characterised by placing a seeing monitor or profiler within the telescope dome.

Dome Seeing

Many telescopes exhibit "dome seeing", in which heat sources in the dome cause typically slow moving turbulence, which may give the appearance of ground layer turbulence. In these cases a relatively inexpensive heat management solution may provide a marked increase in image quality, and the need for a GLAO system can then be more realistically assessed.

We present the case of the Canada France Hawaii telescope (CFHT), and the proposal for 'IMAKA, a wide field, high resolution optical imager, with a GLAO system [49]. Previous turbulence profiling campaigns have shown that Mauna Kea is suitable for GLAO as there is

typically strong surface layer turbulence and a weak free atmosphere [50]. It has long been known that turbulence from the dome and the telescope itself has an effect on the CFHT image quality [51], and recently a program of venting the dome has been implemented, gathering data from both physical, and computational fluid dynamic models of the telescope. As part of both the dome venting project, and presenting the case for 'IMAKA an instrument called OTP (Optical Turbulence Profiler) has been deployed on the CFHT and has been running since July 2009. This instrument is a high resolution Shack Hartmann wavefront sensor measuring a portion of the telescope pupil. This allows atmospheric turbulence to be characterised, to see any improvements from dome venting, and to filter out dome seeing from surface layer turbulence.

Free Atmosphere

Wavefront reconstruction in MCAO and MOAO critically depends on the $C_n^2(h)$ profile, and the accurate conjugation of the deformable mirrors. Hence it is important to be able to accurately pin down the altitude (and strength) of high atmosphere turbulence to allow for optimum reconstruction. Basden *et al.* [52] suggest that DM's should be conjugated to an accuracy of a few hundred metres of the dominant turbulence. In the EAGLE conceptual design, a figure of 250 m is placed on the requirement for accurate measurement of the optical turbulence profile [46].

Requirements

This subsection leads us to conclude that our ideal turbulence profiler can provide a profile of the surface layer to sub 10 m resolution, whilst being able to locate the altitude of free atmosphere turbulence to within 250 m. Currently SL-SLODAR achieves the first criterion, but is unable to profile above a few tens of metres. On a small telescope, SLODAR can provide the 250 m resolution, but only up to an altitude of 1250 m, to profile to higher altitudes it its required to sacrifice altitude resolution. In section 2.3 we shall see that it is possible to measure the wind velocity and direction from the SLODAR (and SCIDAR) instruments, however this places a maximum limit on the cycletime, t_{cyc} of the detector

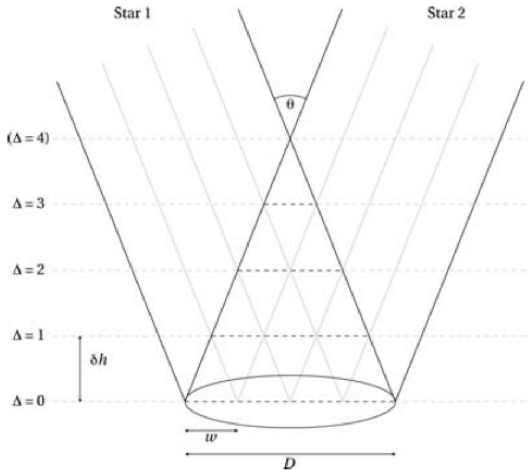

Figure 2.9: Overview of the SLODAR geometry. θ is the separation of the binary pair, D is the diameter of the telescope pupil, and w is a width of a single lenslet (sub-aperture) in the Shack Hartmann lenslet array. The centres of the altitude bins are given by $\Delta\delta h$ [54].

used, as it must be less than the crossing time of a turbulent layer

$$t_{\mathrm{cyc}} = D_{\mathrm{tel}}/v_{\mathrm{layer}}, \tag{2.47}$$

where D_{tel} is the telescope diameter, and v_{layer} is the velocity of the turbulent layer.

SCIDAR can provide a profile for the whole atmosphere, however not to the resolution required for EAGLE. Chapter 4 of this thesis discusses a method to improve the altitude resolution of SCIDAR, and chapter 5 a method to allow the SL-SLODAR to provide an estimate for free atmosphere turbulence and altitude.

2.3 SLODAR

2.3.1 SLODAR Principle

The SLODAR technique uses a binary star pair, which is observed using a Shack-Hartmann wavefront sensor, and the centroid data for each sub-aperture of the wavefront sensors are cross-correlated. The turbulence profile is obtained either by a deconvolution [53] or fitting a theoretical response function [54].

The binary star projects 'copies' of the wavefront aberration caused by the turbulent

layer at height H onto the ground. These copies have separation S. There is then a peak in the cross covariance function for this offset. Using simple trigonometry the value for H can be found by triangulation, where $S = H\theta$, and θ is the (measured) binary star separation. Thus the height resolution is determined by the separation of the sub-apertures of the Shack-Hartmann sensor (Figure 2.9). The strength of a turbulent layer is related to the amplitude of this cross-covariance signal, and in the simplest case a profile can be recovered by a deconvolution using the auto-covariance pattern of the brightest star on the Shack-Hartmann sensor. Even though the cross-covariance is 2-d, to recover the profile only a cut through the cross-covariance pattern in the direction of the binary star separation is required.

The 2-d cross covariance can also be used to determine the wind velocity and directions at different heights by introducing a temporal offset (Figure 2.10).

The centroiding algorithms in the SLODAR systems implemented by the Centre for Advanced Instrumentation, Durham use both thresholding and a circular window to reduce the effect of noisy spots in low signal regimes. In section 2.2.1 we state this leads to a measurement of Z-tilt, as opposed to G-tilt. In the case of SLODAR, the instrumental response functions stem from the work of Wilson and Jenkins [55] in which the mathematical analysis assumes measurement of Z-tilt, so the thresholding and windowing are essential.

2.3.2 SLODAR response functions, and β

In the first SLODAR instruments the turbulence profile was retrieved using a simple devonvolution with the auto-covariance, however in practice this is inaccurate. The average motion of the centroids (over all of the Shack-Hartmann sensor) must be subtracted from the data to remove the effects of errors in telescope guiding and the wind-shake of the telescope. The atmosphere itself introduces a common tilt motion across the wavefront which is also removed by this method. This introduces a small anisoplanatic component, so the response varies slowly with height. The mathematical functions that describe this response are known as SLODAR Impulse Response Functions (SIRFS). To derive these SIRFS it is first necessary to know the power spectrum of the turbulence that is measured. Kolmogorov's turbulence model is assumed, response functions are calculated and represented as a matrix. To recover the turbulence profile the generalised inverse of this matrix is multiplied by the

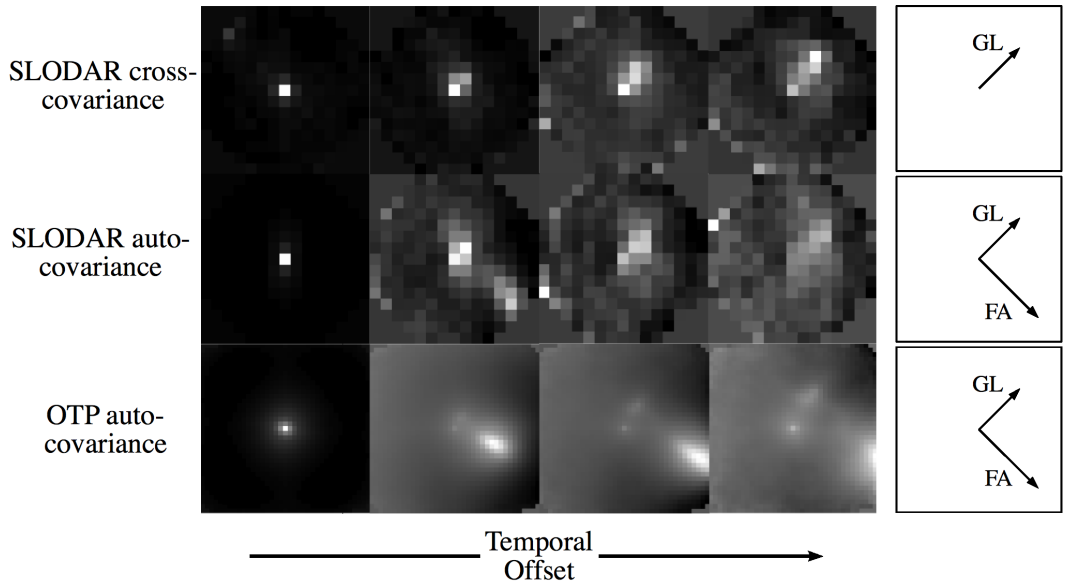

Figure 2.10: Figure showing cross and auto covariance movies for iSLODAR (top, middle), and autocovariance movie for the Optical Turbulence Profiler (OTP). OTP was a high resolution Shack Hartmann sensor on the CFHT for the purpose of characterising dome seeing. The temporal offset increases from left to right. In the two autocovariance images two layers can be seen, a slow layer to the 'North North East', and a faster one moving to the 'South East'. The fast layer can not be seen in the cross covariance, indicating that it has an altitude above 6 km, and this movie also shows the slower layer is at the ground. These turbulent layers are indicated in the key at the right, as ground layer (GL) and free-atmosphere (FA). Both sets of data were taken within 3 minutes of 13:38UT, on the 6th July 2009, Mauna Kea, HI.

cross-covariance. The process for deriving the response functions is presented in [54].

In addition the SLODAR fits a paramater β corresponding to the β in the generalised power spectrum (equation 2.13). This provides a check that the turbulence measured is Kolmogorov ($\beta = 11/3$), the implications of which will be discussed later in this thesis.

2.3.3 Different SLODAR configurations

Depending on the application of the instrument, the SLODAR instrument is deployed in one of three basic configurations. We concern ourselves mainly with small telescope SLODAR (telescope diameter < 0.5 m). Historically the two spot patterns have been separate, on one single CCD detector, and typically this allows for measurements of the ground layer of the atmosphere, up to an altitude of about 1 km, with an altitude resolution of approximately 125 m. A SLODAR of this type was situated at the South Africa large telescope in 2010, and also for the Tololo campaign in 2004 [56], Paranal 2005-6, and Mauna Kea in 2006 [57].

The second configuration is known as Surface Layer SLODAR (SL-SLODAR), in which a reflecting prism is used to separate the light from the two stars, onto two independent detectors [47]. This permits very wide binary star pairs to be measured, and allows profiling of the surface layer of turbulence to a resolution of about 10 m. This instrument is currently in use at Cerro Paranal, supporting the ESO VLTs. The third configuration interleaves the two spot patterns on a single detector to allow very close binaries to be observed, This allows turbulence to be measured up to almost 10 km, albeit with a very coarse resolution (bins are over 1 km wide). This instrument was originally tested at Mauna Kea in 2009, when it was known as iSLODAR. It is currently situated on La Palma, to provide turbulence profiles, and to support the CANARY adaptive optics pathfinder, where it is known as Full Atmosphere SLODAR (FA-SLODAR).

In addition to a stand alone instrument, SLODAR can be incorporated into other experiments. In April 2009 the author ran a SLODAR on the 4.2 m WHT, providing support for a range gated CCD experiment for a novel Laser Guide Star, an example profile from which is shown in figure 2.8.

2.4 SCIDAR

2.4.1 SCIDAR Principle

SCIDAR predates SLODAR, and operates in a similar manner. However instead of measuring the phase slope of the wavefront fluctuations, the scintillation patterns for the binary star pairs are measured. The two overlapping pupil images are incident on a single detector, and the auto-covariance of this image is calculated as, unlike for the SLODAR spot patterns the pupils can not be separated [58, 59]. This leads to a distinctive covariance pattern, with a single peak in the centre, and symmetrical 'side lobes' corresponding to turbulence at different altitudes. The $C_n^2(h)$ profile is again retrieved by fitting response functions. A large telescope (> 1 m) and sensitive detectors are required, as are bright binary stars of fairly equal magnitudes. This instrument was proven in site testing campaigns, for example at the ORM on La Palma [21]

2.4.2 SCIDAR instruments

In conventional SCIDAR the detector is optically conjugate to the telescope pupil Turbulence near the ground does not produce scintillation in this plane and therefore is invisible to the detector. To allow this turbulence to be sensed, the observation plane is moved to be conjugate to a distance below the ground (typically -2 km). This concept is known as *Generalised* SCIDAR (G-SCIDAR) [60], and allows for profiling of the full atmosphere.

Both classical and generalised SCIDAR require the use of large telescopes, and there have been two different modifications to allow for SCIDAR turbulence profiling on small (< 50 cm) telescopes.

Single star SCIDAR [61] attempts to retrieve the optical turbulence profile using only one star as a source. A star is observed using a small telescope, and the auto-covariance of the pupil intensity is measured. Response functions are then fitted to this auto-covariance. As there is only one peak, this presents problems fitting responses for different altitudes. The response functions are not orthogonal, and a rigourous fit requires high sampling of the auto–covariance, with the detector at different conjugate altitudes.

Low Layer SCIDAR (LOLAS) is a SCIDAR instrument to measure optical turbulence

profiles of the planetary boundary layer with high altitude resolution. It is a modification of the G-SCIDAR technique implemented on a 40 cm telescope and using very wide binary stars. As an example, observing a 200" binary star pair will yield an altitude resolution of 12 m up to a maximum sensing altitude of ~ 400 m [62].

Chapter 3

Simulation

This chapter describes the atmospheric and instrument computer simulation used for the work in chapters 4, 5, and 6. The methods for simulating atmospheric turbulence and performing Fresnel propagation are discussed. The simulation is verified against theoretical models for turbulence strength, centroid variance, and scintillation index on small and large scales. The sampling of the simulated data is discussed, to ensure that the results are appropriate for the applications. Finally the approximations made are discussed.

The simulations are written in Python (with extensive use of the Numpy and Scipy extensions), and C. They are implemented on an Ubuntu Linux workstation. An example SLODAR profile (corresponding to about 1 minute of data taken on sky), would take approximately six hours to simulate.

3.1 Methods for Computer Simulation of Atmospheric Turbulence

The simulation used for this work is based on widely used methods outlined by (for example) Ellerbroek and Cochran [63]. The atmosphere is modelled by a number of discrete phase screens at differing altitudes. In reality the turbulent layer will evolve with time. However we assume that Taylor's approximation holds, so that the patterns of aberrations are frozen as they move across the telescope pupil. In effect this implies the turbulence evolution

timescale is longer than the telescope crossing timescale.

3.1.1 Generating phase screens

The phase screens are produced from spatially filtered white noise, given by the formula

$$P(\boldsymbol{x}) = c \cdot \mathrm{Re}\left[\mathfrak{F}\left(\sqrt{\Phi(\boldsymbol{\kappa})}\left(r(\boldsymbol{\kappa}) + ir'(\boldsymbol{\kappa})\right)\right)\right] \tag{3.1}$$

where P is the phase screen, $\mathfrak{F}$ is the 2-d Fourier transform, Φ is the power spectrum of the turbulence, $\boldsymbol{\kappa}$ is a spatial frequency variable, r and r' are white noise functions, and c is a scaling factor to adjust the strength of the phase screens. For the von Karman turbulence spectrum the power spectrum Φ has the form

$$\Phi(\boldsymbol{\kappa}) = |\kappa^2 + (W/L_0)^2|^{-11/6} \tag{3.2}$$

A Kolmogorov spectrum can be obtained by setting $L_0 = \infty$. The scaling factor c_n for a layer n is defined by the expression

$$c_\mathrm{n} = 0.1517\sqrt{\frac{t_\mathrm{n}}{t_\mathrm{total}}}\left(\frac{W}{r_0}\right)^{5/6}\left(\frac{\lambda}{2\pi}\right) \tag{3.3}$$

where t_n is the turbulence strength in the layer n, t_total is the total turbulence, and r_0 is the Fried parameter (over all layers) at wavelength λ.

The simulated atmosphere consists of one or more of these discrete phase screens at different heights above the ground.

3.1.2 Geometric Propagation

Providing that the effects of Fresnel propagation are not required (i.e. no scintillation effects), then a simple geometric model of propagation can be used. For an atmosphere consisting of n phase screens at arbitrary heights, with an incident complex field from the star of $U_\mathrm{in}(\boldsymbol{x}) = A_\mathrm{in}(\boldsymbol{x})\exp(i\phi_\mathrm{in}(\boldsymbol{x}))$, and for each layer i undergoes a phase shift $\Delta\phi_i(\boldsymbol{x})$, which is implemented simply as a product of the input field and the complex exponential of the phase shift. Hence the phase measured at the ground after propagation through this

atmosphere is

$$\phi_{\text{ground}} = A_{\text{in}} \exp\left(i\phi_{\text{in}}\left(\boldsymbol{x}\right)\right) \sum_{i=0}^{n} \exp\left(i\Delta\phi_i\left(\boldsymbol{x}\right)\right). \tag{3.4}$$

Using a geometrical method means that the effects of Fresnel propagation and scintillation can not be investigated, however this method provides a large speed increase as convolutions are not required to propagate the wavefront through the atmosphere.

3.1.3 Fresnel Propagation

If the effects of atmospheric scintillation and the effect of propagation on the electric field are to be considered, then we must implement Fresnel propagation.

The complex field incident on a phase screen $U_{\text{in}}\left(\boldsymbol{x}\right) = A_{\text{in}}\left(\boldsymbol{x}\right)\exp\left(i\phi_{\text{in}}\left(\boldsymbol{x}\right)\right)$ undergoes a phase shift of $\Delta\phi\left(\boldsymbol{x}\right)$, which is implemented as a product of the input field and the complex exponential of the phase shift. As the complex field propagates through free space past this layer, the field at a distance z from the layer is given by the convolution (denoted $\otimes$)

$$U_{h-z}\left(\boldsymbol{x}\right) = U_h\left(\boldsymbol{x}\right) \otimes K\left(\boldsymbol{x}, z\right), \tag{3.5}$$

where $K\left(\boldsymbol{x}, z\right)$ is the point spread function of Fresnel propagation, and is defined for a propagation distance z as

$$K\left(\boldsymbol{x}, z\right) = \frac{1}{i\lambda z} \exp\left(ikz\right) \exp\left(\frac{i\pi\left|\boldsymbol{x}\right|^2}{\lambda z}\right). \tag{3.6}$$

We adopt a convention that positive z indicates a diverging spherical wavefront, and negative z a converging wavefront. The above step is repeated to model the effects of a multi layer atmosphere.

In the simulation this is implemented using the convolution theorem, which states that for two functions f and g,

$$\mathfrak{F}\left(f \otimes g\right) = \mathfrak{F}\left(f\right) \cdot \mathfrak{F}\left(g\right) \tag{3.7}$$

where $\mathfrak{F}$ denotes the forward Fourier transform. Hence equation 3.5 becomes

$$U_{h-z}\left(\boldsymbol{x}\right) = \mathfrak{F}^{-1}\left[\mathfrak{F}\left(U_h\left(\boldsymbol{x}\right)\right) \cdot \mathfrak{F}\left(K\left(\boldsymbol{x}, z\right)\right)\right] \tag{3.8}$$

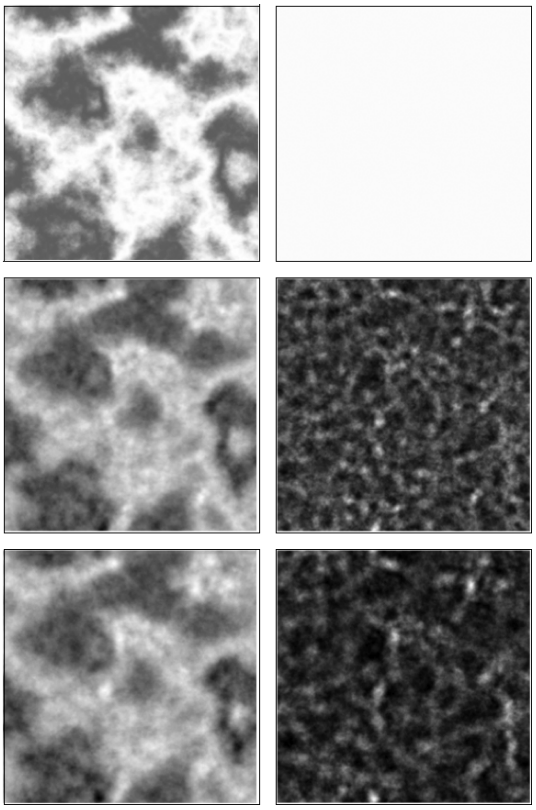

Figure 3.1: A diagram showing the effects of Frensel propagation on phase (left) and intensity (right) for a single phase screen. The propagation distances are 0 km (top), 4 km (middle), and 8 km (bottom). The propagation leads to the phase map 'smoothing', and to the development of spatial structure in the intensity patterns. Note the development of larger scale structure in the intensity images for larger propagation distances. The images are arbitrarily scaled for clarity.

where $\mathfrak{F}^{-1}$ is the inverse Fourier transform.

The effects of Fresnel propagation on both the phase and intensity patterns are shown in figure 3.1.

3.1.4 Sampling Limits

As we are using a numerical simulation, which is also discrete in terms of spatial sampling, certain sampling conditions must be met. The criteria in Johnston and Lane are used [64], and explained below. In Nyquist sampling a signal is sampled at twice the maximum frequency present. However, as the phase signal has in effect infinite bandwidth, to ensure

the phase screen is well sampled neighbouring array elements must have a phase difference of less than π. Using equations 2.3 and 2.7, we can write the expression

$$\left\langle \left|\phi\left(r\right)-\phi\left(r+\Delta r\right)\right|^{2}\right\rangle = 6.88\left(\frac{\Delta r}{r_0}\right)^{5/3} \leq \pi^2 \tag{3.9}$$

where $\phi(r)$ and $\phi(r+\Delta r)$ are adjacent elements of the phase screen, with a separation distance Δr. Numerically this gives a limit for the phase sampling of

$$\Delta r \leq 1.24 r_0. \tag{3.10}$$

In addition to adequately sampling the phase, the intensity pattern must also be Nyquist sampled. As the first Fresnel zone has the smallest scale, we must ensure this is well sampled. Each array element must sample half the smallest size of the irradiance fluctuation. We can therefore impose another condition on Δr,

$$\Delta r \leq \frac{\sqrt{\lambda z}}{2}. \tag{3.11}$$

To illustrate the suitability of the simulation parameters chosen with respect to the sampling criteria I present examples of the most 'extreme' uses of the simulation in the work of this thesis. In the work presented in chapter 4, a telescope diameter of 2.2 m is used, with 256 elements across the pupil diameter. This gives a scale of 0.9 cm per array element, and so to ensure the phase sampling is suitable the minimum value for r_0 is 0.7 cm. This corresponds to turbulence much stronger than is measured at typical observing sites.

In terms of scintillation we make the assumption commonly held for SCIDAR, that a distance of 2000 m is required for a strong scintillation signal to develop, and so the minimum Fresnel length to be measured will correspond to propagation over this distance. Using equation 3.11, and a wavelength of 500 nm, the criterion for the maximum array element size is 1.5 cm per element.

For the SLODAR simulations used in chapter 5, the smallest subapertue size is 4.75 cm, sampled by 8×8 array elements, yielding a scale of 0.6 cm per element. Using the phase criterion, the minimum value for r_0 that can safely be used is 0.5 cm, and the minimum

array element size from the scintillation criterion is again 1.5 cm.

3.2 Verification of the Simulation

3.2.1 Phase Screens

As the phase screens are generated using a spatial filter corresponding to the power spectrum of the turbulence, it is appropriate to verify the phase screens against the theoretical spatial phase structure function. There are two key reasons for this; (i) to ensure the power law and the scaling of the structure function are correct, and (ii) to establish over what spatial scales the phase screen is well characterised, as the finite spatial extent of the phase screens used introduces an implicit outer scale.

We can use a second independent test to verify both the turbulence strength of the phase screen, and the image formation code used for the Shack Hartmann wavefront sensor. The screen is divided into a grid of squares, each consisting of $n \times n$ array elements. An image is formed for each square, the resulting spot centroided. The theoretical variance of the centroids in the case of Kolmogorov turbulence across each image can be related to the turbulence strength [65] as;

$$\sigma_c{}^2 = 0.162\lambda^2 r_0{}^{-5/3} d^{-1/3}. \tag{3.12}$$

This equation yields a centroid variance in units of radians^2, where as any result from the simulation will give the variance in units of pixels^2. To convert between the two, we can simply say

$$\sigma_c\,(\text{radians}) = \frac{\lambda}{nd}\sigma_c\,(\text{pixel})\,. \tag{3.13}$$

The scaling is a consequence of the use of Fourier transforms to generate the image from the complex phase, and n is the oversampling factor used for the transform. In the simulations in this work, $n = 2$ is used to ensure Nyquist sampling of the phase aberrations for image generation.

The simulated and theoretical centroid variances are shown in figure 3.2. The centroid variances are generated for two subaperture diameters (4.75 cm, and 6.25 cm), corresponding to the first FA-SLODAR on La Palma, and the current SL-SLODAR and FA-SLODAR

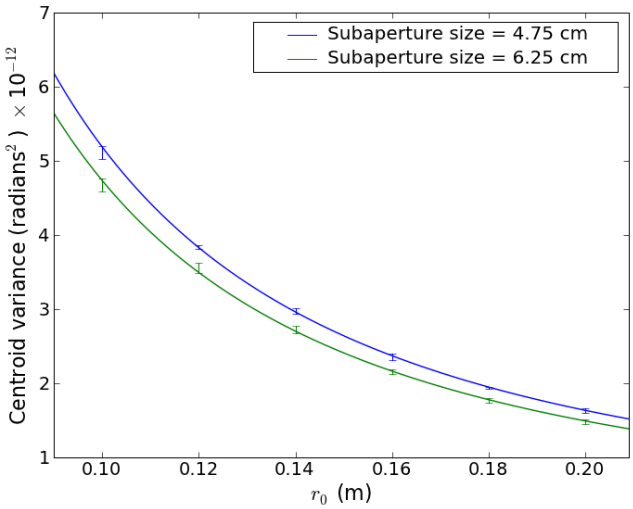

Figure 3.2: Simulation results showing centroid variance against r_0 for two different subaperture sizes (4.75 cm, and 6.25 cm). We use 16 pixels per subaperture on the phase screen, and only take measurements across the centre 50% of the screen to ensure there are no edge effects. The images are made using $\times 2$ oversampling to ensure Nyquist sampling, and the centroids are measured using a centre of mass algorithm. The theoretical values are plotted with the solid line, and the simulation as the data points. The uncertainty is estimated by the variance of different independent realisations of the Monte–Carlo simulation.

respectively. The supapertures both correspond to 16×16 pixels on the phase screen, we use Nyquist sampling to form the images, and a centre of mass algorithm to measure the centroid. To counteract any possible edge effects, only the middle 50% of each screen is used. From the figure it can be seen that the simulation and theory are in agreement, showing that both the phase screens, and the conversion between pixel variance and angular variance are physically appropriate.

3.2.2 Fresnel Propagation

As stated in equation 2.39 there is a clear dependence of the scintillation variance on both turbulence strength and altitude. This allows us to verify the strength of the phase screens, wavelength effects, and propagation distance. In addition, the effects of spatial averaging within an aperture can be verified against theory, as for large apertures the equation for

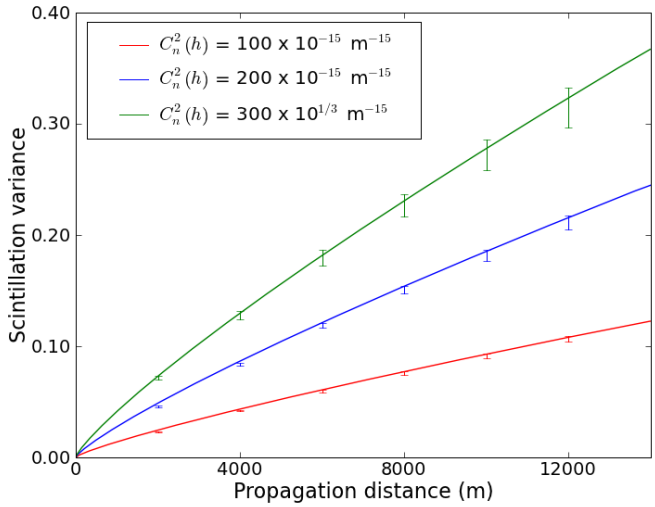

Figure 3.3: Simulation results showing scintillation variance against layer altitude, for three different values of C_n^2, demonstrating the $\sigma_I \propto h^{5/6}$ relationship for small apertures. The scintillation index is measured at the ground. The pixel size is 1 cm, and the wavelength is 500×10^{-9} m.

scintillation variance [8] is,

$$\sigma_I^2 \propto D^{-7/3} (\cos\gamma)^{-3} \int_0^\infty h^2 C_n^2(h)\, \mathrm{d}h \tag{3.14}$$

In figure 3.3 the simulated and theoretical scintillation variance for a phase screen with 1 cm pixels are shown. Independent realisations of each screen are placed at a given altitude, illuminated with planar light, and this is allowed to propagate to the ground where the intensity and its variance are calculated. The theoretical values for the scintillation variance are calculated from equation 2.39, and the two are shown to be in good agreement. Figure 3.4 shows the same process but spatially averaged into 50 cm apertures, to test the validity of our simulation in the regime described by equation 3.14. We only demonstrate the general trend by arbitrarily scaling the plot, rather than calculating the constant of proportionality, and again the simulation is shown to be in good agreement with theory.

The effects of Frensel propagation are calculated by a product in Fourier space, and this can lead to so called *edge effects*, as the finite extent of the phase screen can behave like an aperture. This exhibits itself as a series of diffraction fringes round the edge of the

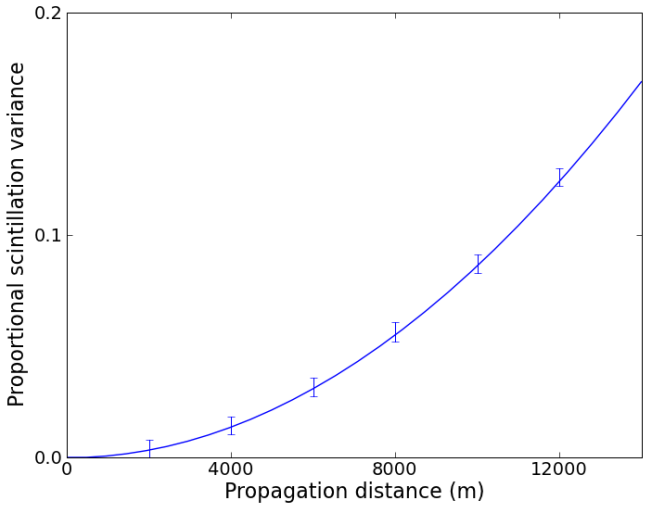

Figure 3.4: Simulation results showing scintillation variance against layer altitude, demonstrating the $\sigma_I \propto h^2$ relationship for large apertures. The scintillation index is measured at the ground. The aperture size is 50 cm, and the wavelength is 500×10^{-9} m.

propagated screen. To combat this, it is ensured that the phase screens are at least four times larger than the region of interest, and as the results above show this leads to good agreement between the simulation and theory.

3.3 Assumptions made

We make four key assumptions in the use of the simulation, and the accuracy and implications of these will be briefly discussed.

- *Thin turbulent layers.* There have been very few high resolution measurements ($\sim$ 10's of metres) for the upper layers of the atmosphere. SL-SLODAR however has shown that there is structure in the SL turbulence, and this suggests there might be similar structures in higher layers. In some cases direct measurements of C_n^2 made by weather balloons have measured turbulent layers up to 200 m thick, however in others the layers are only 10 m thick [66]. Hence whilst we make the approximation of thin layers (for computational reasons), high resolution profiling of the full atmosphere is required to confirm for how much of the time this approximation is valid. For thick high layers

the approximation will only break down for large fields of view, as the overlapping pupils will diverge through the layer, and so different parts of the layer will be not be sampled with the same overlap.

- *Kolmogorov statistics for the phase aberrations.* Turbulence in the free atmosphere is generally assumed to have a Kolmogorov power spectrum for the purposes of atmospheric simulation, for example [52, 67]. In some observations the value for β at the ground has been measured to be less than 11/3. This has been observed by the SL-SLODAR at Paranal, however the low β values typically occur for low wind speeds, as turbulence on longer spatial scales is not properly sampled.

- *Taylor approximation (frozen flow hypothesis).* As turbulence results from wind shear some velocity dispersion should be expected, however high resolution data is needed to investigate this, (high resolution in both altitude and time). We see well defined translating peaks when the temporal offset is applied to the SLODAR covariances (see figure 2.10) which implies that the approximation is at least partially accurate.

- *'Weak' turbulence.* Strong turbulence at high altitudes can lead to a saturation of scintillation. This is generally not true in good observing conditions at a good observing site. The turbulence profile is often 'bottom heavy', i.e. the strongest layer of turbulence is at the ground, so that scintillation is typically weak.

3.4 Conclusions

This chapter presented an overview of the Monte-Carlo simulation that will be used for work in this thesis, both to investigate the performance of instruments and methodologies, but also to provide calibration data for the free atmosphere fitting to SLODAR data shown in section 5.4.1. The methodologies for generating the turbulence were presented, as were a simple geometric, and a more complex (but physically accurate) Fresnel propagation method. The simulation outputs were tested against theoretical values for both scintillation index and phase variance. This check against phase variance also confirmed the correct angular scale for the phase screens.

Using the sampling conditions of Johnston and Lane, the simulation was shown to be fit for purpose, using examples of the most extreme cases in the following work. Finally the approximations used, and limitations were explicitly set out.

Chapter 4

Stereo-SCIDAR

4.1 Introduction

In this chapter we propose a new SCIDAR instrument, based on the instrument design used for Conjugate–Plane Photometry by Osborn *et al.* [68]. The incoming light from the double stars is fully separated onto two CCD detectors, each on independent arms of the instrument. This gives two advantages for SCIDAR, first the ability to normalise each pupil image before the correlation process, and to be able to change the conjugate altitude of the instrument dynamically to increase height resolution. For the work in this chapter, a system deployed on the Nordic Optical Telescope (NOT) in September 2010 is considered.

The theoretical altitude resolution for a SCIDAR instrument varies with altitude and is given by

$$\delta h\left(z\right) = 0.78\frac{\sqrt{\lambda z}}{\theta} \tag{4.1}$$

where z is the propagation distance to the turbulent layer, and θ is the angular separation of the double star [69]. The resolution for SCIDAR for three different star separations is shown in figure 4.1, showing that the resolution increases for both smaller conjugate distance and for wider double stars. It must be noted that for a given telescope diameter, the wider the star separation, the lower the total profiling altitude of the instrument. Conventional SCIDAR methods also require the double stars to be of similar magnitudes to prevent the

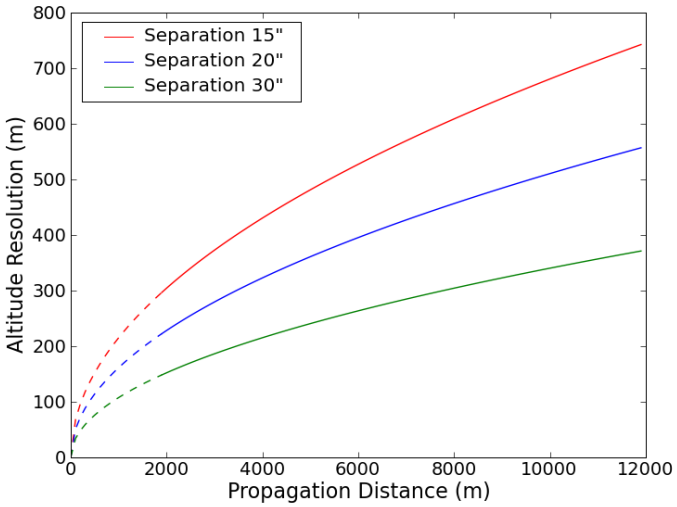

Figure 4.1: The effects of increasing the optical propagation distance on the altitude resolution of SCIDAR. We also show the effect of chaging the separation of the double star. Recall that SCIDAR is effectively blind to turbulence with a propagation distance of less than 2 km, and this portion of the curve is shown only for completeness. A wavelength of 500×10^{-9} m was used for this graph.

scintillation pattern from the brighter star swamping that of the dimmer. A sketch of the instrument configuration for Stereo SCIDAR is shown in figure 4.2.

The instrument under consideration was installed on the 2.2 m NOT, and two Andor Luca S cameras were used. A key consideration is the mapping of CCD detector position within the instrument. The telescope has an aperture diameter of 2.2 m and an effective focal length of 28.16 m. A collimating lens of focal length 3.2 cm leads to a beam diameter of 0.0025 m. The magnification of this system G is 880, and the shift in conjugate altitude Δh is related to the shift in detector position Δz by the equation [3]

$$\Delta h = G^2 \Delta z. \tag{4.2}$$

Hence a shift of the detector by 1.3 mm leads to a 1 km change in conjugate altitude.

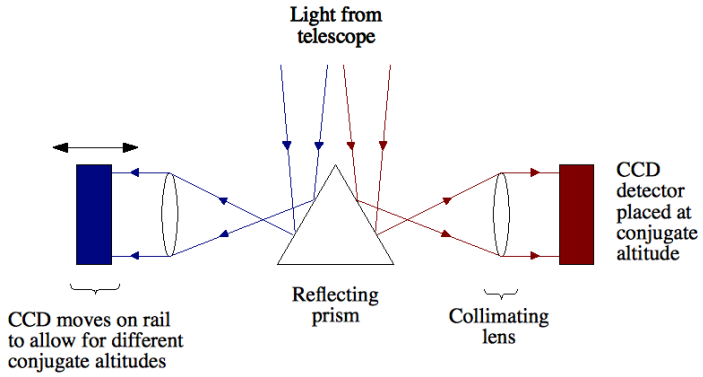

Figure 4.2: A schematic of the Stereo SCIDAR instrument. The reflecting prism in the centre sends the light from each star down two arms of the instrument. The light in each arm is then collimated, and the resulting intensity pattern in this plane is imaged on to the CCD detector. The collimating optics and CCD detectors are attached to a rail, and can move to allow for different altitude conjugates of the instrument.

4.2 Stereo-SCIDAR Response Functions

The quantity measured by the Stereo-SCIDAR instrument is the *normalised scintillation spatial covariance function* $B(\boldsymbol{r})$, where

$$B(\boldsymbol{r}) = \frac{\langle [I_1(\boldsymbol{x}) - \langle I_1 \rangle] [I_2(\boldsymbol{x}+\boldsymbol{r}) - \langle I_2 \rangle] \rangle}{\langle I_1 \rangle \langle I_2 \rangle}, \tag{4.3}$$

where $I_n(\boldsymbol{x})$ is the normalised intensity distribution in the pupil plane for a single star. The angled brackets denote an ensemble average. As the power spectrum of the intensity variations for both stars are identical, the cross covariance of the intensity patterns can be related to the power spectrum of the scintillation using the Wiener-Khintchine theorem. This states that a cross correlation corresponds to the Fourier transform of the power spectrum. The power spectrum is isotropic, so we can say $\langle I \rangle$ is time independent, and $B(\boldsymbol{r}) \equiv B(|\boldsymbol{r}|) \equiv B(r)$. Owing to this isotropic nature, the Fourier transform can be replaced with a Hankel transform

$$B(r) = 2\pi \int_0^\infty f \Phi_I(f) J_0(2\pi r f) \, \mathrm{d}f \tag{4.4}$$

where J_0 is a bessel function of the first kind. We rewrite $B(r)$ to take into account the altitude dependence of the turbulence

$$B(r) = \int_0^\infty B_h(r,h)\,\mathrm{d}h, \tag{4.5}$$

and from equations 2.31 and 4.4 we show

$$B_h(r,h) = 3.9\times10^{-2}2\pi k^2 C_n^2(h)\int_0^\infty f^{-8/3}\sin^2\left(\pi\lambda h f^2\right)J_0(2\pi r f)\,\mathrm{d}f. \tag{4.6}$$

This is the intensity fluctuation cross correlation density per unit altitude produced by a layer located at a distance h. We also define a further quantity $B'_h(r,h)$, corresponding to $B_h(r,h)$ for unit turbulence strength. This quantity is what we will define as the S-SCIDAR response function for unit turbulence at altitude h. As the altitude conjugation of this instrument can be changed dynamically, the propagation distance z becomes $h-h_{\mathrm{conj}}$, and so the measured double star cross covariance ($B_{**}(r,\theta)$) corresponds to

$$B_{**}(r,\theta) = \frac{1}{4}\int_h C_n^2(h)\,B'_h(r,h-h_{\mathrm{conj}})\,\mathrm{d}h. \tag{4.7}$$

A plot of S-SCIDAR response functions is shown in figure 4.3. We show three responses for differing propagation distance. As the propagation distance increases the cross covariance signal increases, but also becomes wider, with a larger number of visible side lobes. We hypothesise that by dynamically reducing the propagation distance of a turbulent layer to the detector via re-conjugation, the resolving power will increase due to the narrower response functions.

4.3 Data Reduction

The two detector images are first background subtracted, and then mean normalised so that each intensity pattern has an average of zero. This ensures that despite differing magnitudes of the stars, one doesn't dominate the other in the cross covariance. Additionally Avila and Cuevas have shown for G-SCIDAR stars with a large (< 1) difference in magnitude introduce

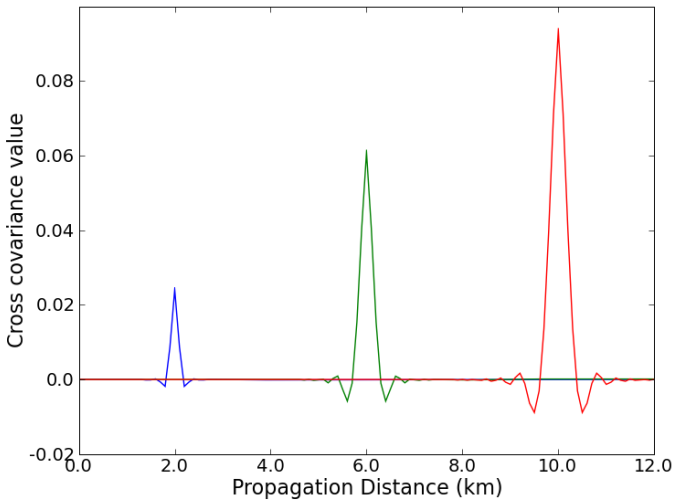

Figure 4.3: The effects of increasing propagation distance on the cross covariance response for S-SCIDAR. Three propagation distances are shown, 2, 6, and 10 km for a single turbulent layer, with strength 100×10^{-15} $\mathrm{m}^{1/3}$

significant errors into the measured turbulence profile [70], and by normalising each star we can ignore this effect.

Unlike G-SCIDAR each layer only contributes one peak in the covariance, corresponding to one of the side lobes in the familiar G-SCIDAR autocovariance pattern. To retrieve the turbulence profile we are required to solve the inverse problem, written in matrix form

$$B\left(r\right) = K_z\left(r, h\right) C_n^2\left(h\right) \tag{4.8}$$

where $B\left(r\right)$ is the measured scintillation cross covariance, and $K_z\left(r, h\right)$ is the matrix of S-SCIDAR responses to unit turbulence at different heights, for a given conjugate altitude z. Unlike G-SCIDAR there is no noise term in the expression: as we take a cross covariance of two independent detectors there will be no noise correlation assuming random noise. In our case the inverse problem is solved using a non negative least squares inversion, to retrieve an estimate for the $C_n^2\left(h\right)$ profile [71].

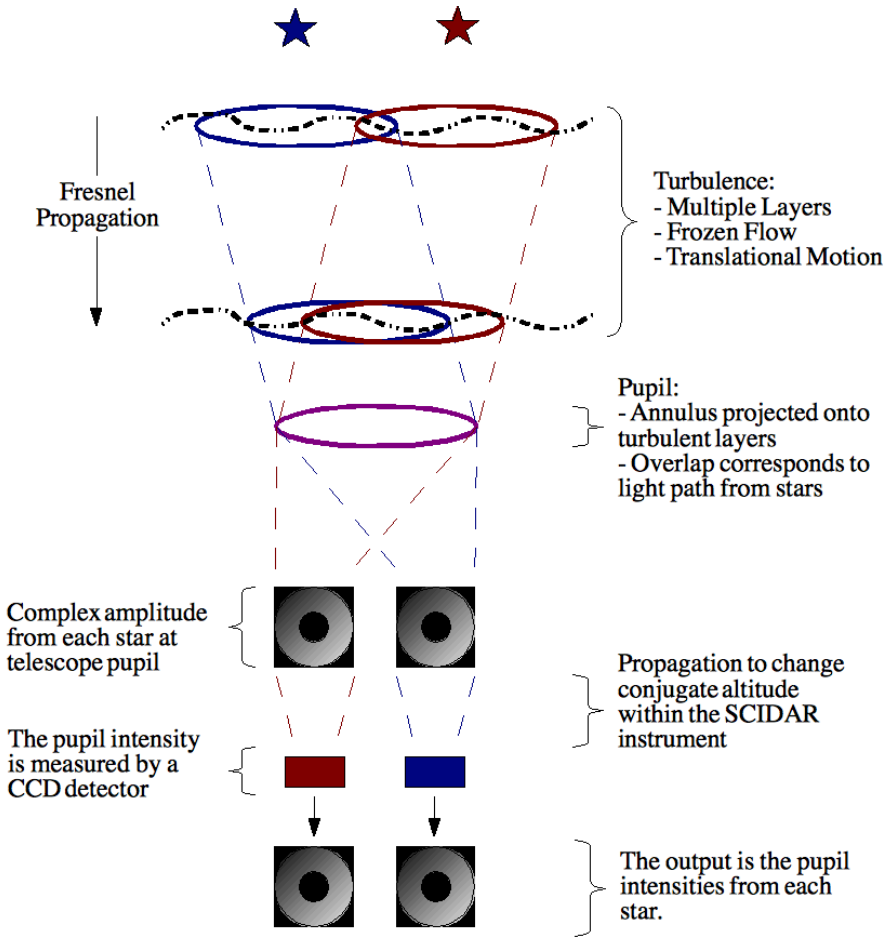

Figure 4.4: A schematic overview of the SCIDAR simulation, showing the phase screens, natural reference stars, and the telescope pupil projection onto the phase screens. It also shows the reconjugation of the instrument.

4.4 Results from Simulation

The performance of S-SCIDAR is explored using a Monte-Carlo simulation of the instrument, as outlined in the previous chapter. A telescope pupil is projected on to the atmospheric phase screens, and the light from the two stars is allowed to propagate through the atmosphere. The light from each pupil is then further propagated in either a forward or backward direction to model the conjugation altitude of the instruments. Pupil images are formed on two detectors, and the photon intensities are scaled to appropriate levels. A schematic of the simulation is shown in figure 4.4.

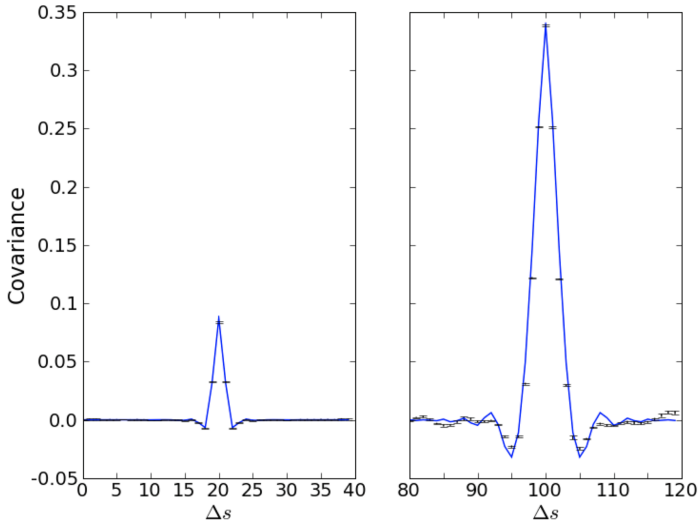

Figure 4.5: Plots of theoretical SCIDAR response functions (solid line) against Monte Carlo simulations for layers with a propagation distance of 2 km (left) and 10 km (right). Both layers have strength 362×10^{-15} $m^{1/3}$.

4.4.1 Response to a single layer

As the S-SCIDAR response functions are calculated theoretically, we first verify that the suppression of the scintillation cross covariance as the propagation distance to a layer decreases, as well as the corresponding narrowing of the response, are the same for both theory and simulation. Figure 4.5 shows that the response functions match the cross covariance data from the Monte-Carlo simulation. It can clearly be seen for the 2 km conjugate distance that the simulated results match the side lobes much better than that for 10 km, and there is much less scatter in the cross covariance.

Figure 4.6 shows the peak cross covariance values for both the theoretical and Monte-Carlo simulated response, for a set of three conjugate altitudes, and a range of layer altitudes. These peak values have good agreement across the parameter space, and the figure clearly shows how the signal drops to zero if the instrument is conjugate to a turbulent layer, making such turbulence "invisible" to the instrument.

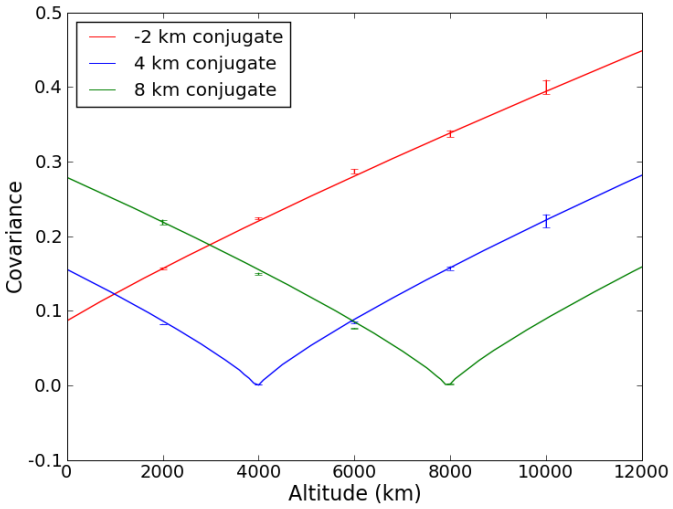

Figure 4.6: Plots of theoretical (solid line) and simulated peak SIRF values for a variety of turbulent layer altitudes and for conjugate altitudes of -2, 4, and 8 km. It can be clearly seen that the turbulent layer becomes "invisible" when the instrument is conjugate to the turbulent altitude, and good agreement is shown in all cases between the simulation and calculated values. The layers have strength 362×10^{-15} $m^{1/3}$.

4.4.2 Closely spaced layers

One of the key hypotheses for the S-SCIDAR instrument was the ability to resolve more closely spaced turbulent layers than G-SCIDAR. However we first must define what we take to mean a resolved layer. As the profile fitting is analogous to finding peaks in an image, we shall say for the sake of this paper that a peak is significant when it is 3σ above the background noise as suggested by [72]. In the case of a closely spaced double layer, the background will be taken as the value for the bin between the two peaks in the C_n^2 profile.

We present three cases, all have a total atmospheric turbulence strength of 362×10^{-15} $m^{1/3}$, distributed in two layers with altitudes 8057.2 m and 8258.7 m. The separation between these layers is chosen such that the distance corresponds to exactly one pixel in the S-SCIDAR cross covariance. In the first case the turbulence is distributed in a 50:50 ratio between the layers, in the second a 40:60 ratio with the higher layer containing a greater turbulence strength, and the third 30:70 again with the higher layer being the stronger. We show the fitted profile for differing conjugate altitudes from -2 km (showing the resolution

we would expect for G-SCIDAR), to 6 km (allowing for a minimum propagation distance of 2 km as discussed earlier). The profiles are shown in figures 4.7, 4.8 and 4.9. The error on the profile fitting is generated using an iterative resampling method using errors from multiple examples of the monte-carlo simulation. Using our 3σ rule, we can say that for the 50:50 case the two layers can be resolved with a 4 km conjugate (4 km propagation distance), however in the 40:60 case they can only be resolved by conjugating to 6 km (a 2 km propagation distance). For the 30:70 case two layers begin to appear for conjugate altitudes for 5 km and 6 km. However they are not significant when compared against our error criterion, and can only be truly resolved for a propagation distance of 1 km. The signal becomes very week, and it may be impractical to use this propagation distance.

From the two figures it can be seen that as the propagation distance decreases the peaks become much clearer (as hypothesised due to the narrowing of the response functions). All the fitted profiles were generated from the same number of phase screen realisations, and being conjugate closer to the layer also yields a secondary benefit. The error on each value for the fitted profile is reduced by fitting the smaller and narrower response.

Despite the differing turbulence distributions in the profile, the total measured turbulence strength for all the plots in figures 4.7, 4.8 and 4.9 should be identical, and on investigation to the fitted profiles all measure the correct integrated turbulence to within the standard error.

4.4.3 Determining the altitude of a Single Layer

Again we consider a simple case, five independent realisations of an atmosphere consisting of a single layer with a height of 4028.6 m. However in each case the layer is shifted so that it lies between two resolution elements in the cross covariance. We consider shifts of 0, 0.2, 0.4, 0.6, and 0.8 pixels. If we assume 'rectangular' resolution elements, for a shift of 0.2 pixels, 80% of the turbulence strength should appear in the lower bin, and 20% in the higher, with similar arguments used for the other cases. In this test also we investigate with a -2 km conjugate, and a 2 km conjugate to investigate the effects of the narrower response function. The results for this example are shown in table 4.1. The data are presented for differences in altitude corresponding to shifts of 0.2 pixels in the cross covariance. There

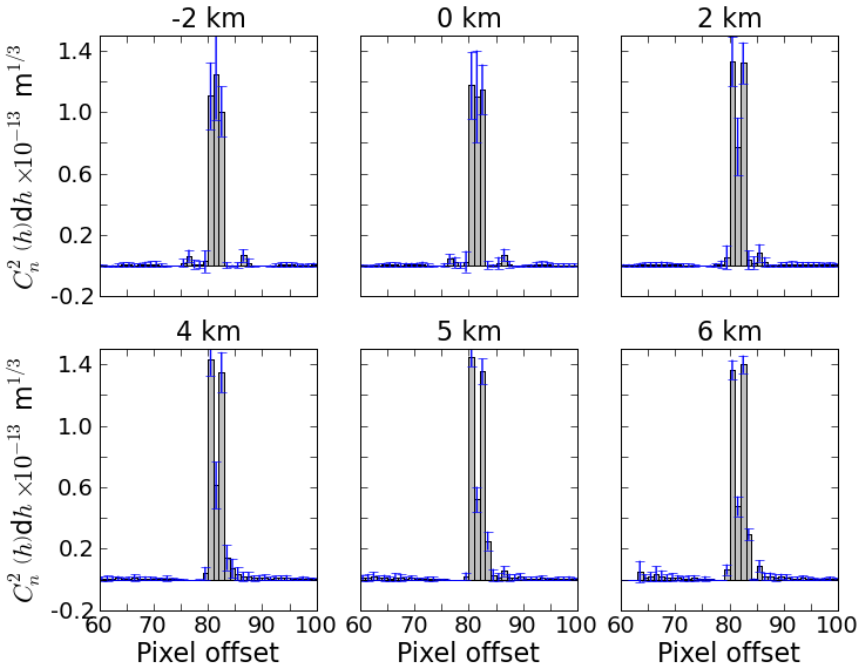

Figure 4.7: Simulated S-SCIDAR profiles for a range of conjugation distances, for a two layer atmosphere (layers at 8057.2 m and 8258.7 m with turbulence distributed 50:50 between the two layers. The errors are calculated from independent realisations of the Monte-carlo phase screen.

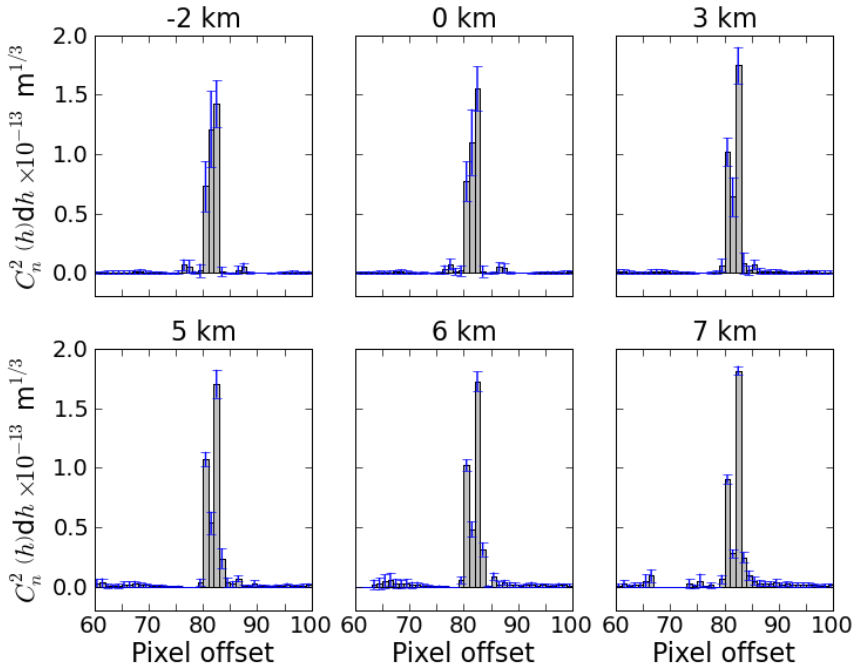

Figure 4.8: Simulated S-SCIDAR profiles for a range of conjugation distances, for a two layer atmosphere (layers at 8057.2 m and 8258.7 m with turbulence distributed 40:60 between the two layers. The errors are calculated from independent realisations of the Monte-carlo phase screen.

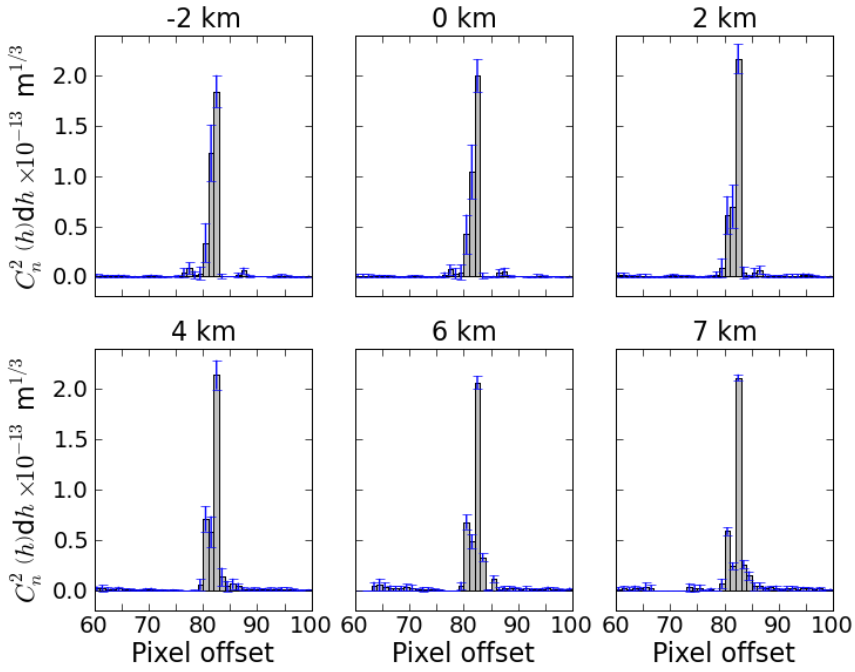

Figure 4.9: Simulated S-SCIDAR profiles for a range of conjugation distances, for a two layer atmosphere (layers at 8057.2 m and 8258.7 m with turbulence distributed 30:70 between the two layers. The errors are calculated from independent realisations of the Monte-carlo phase screen.

	Measured Altitude (m)	
Actual Altitude (m)	$h_{conj} = -2000$km	$h_{conj} = 2000$km
4029	4025 ± 2	4027 ± 1
4049	4045 ± 1	4050 ± 1
4069	4064 ± 1	4068 ± 1
4089	4084 ± 1	4086.0 ± 0.4
4109	4104 ± 1	4105 ± 1

Table 4.1: The effects of re-conjugating the S-SCIDAR instrument to pin-point the altitude of a single turbulent layer. The altitudes chosen correspond to fractions of a pixel, 4029 m being a pixel centre, and the other altitudes corresponding to shifts of 0.2, 0.4, 0.6 and 0.8 pixels. A slight systematic offset can be seen, where the S-SCIDAR measures slightly higher altitudes. There is a slight increase in accuracy for the measured altitude for a closer conjugate.

are systematic offsets where the S-SCIDAR measures slightly higher altitudes, however both the systematic and random errors on the measured altitudes are very small, compared to the resolution defined in equation 4.1.

It is theoretically possible to resolve a single layer in practice, hence the limiting factor is the ability to distinguish closely spaced layers.

4.4.4 Effects of misconjugation

As the two arms of the instrument move independently, when we re-conjugate the detectors it is important to ensure that both are placed accurately at the appropriate position. The geometry of the instrument ensures that the turbulence is measured in the correct location, as the pupil positions on the detector do not vary with conjugate altitude. However as the response functions are dependent on the conjugate distance, the turbulence strength will not be measured accurately. We show two examples from simulation, again with a layer at 4028.6 m. This time we take our expected conjugate altitudes to be 0 km, and 2 km, however we deliberately misconjugate each detector above and below this altitude, in our example ±200 m, and ±400 m (corresponding to errors in 0.25 and 0.5 mm in the physical location of the detectors), the results of which are shown in figure 4.10. Table 4.2 shows the suppression of the peak in the turbulence profile, and also the reduction in the integrated turbulence strength. We see that for relatively small misconjugation the effect on the measured turbulence is quite marked, more so in the case with a smaller propagation

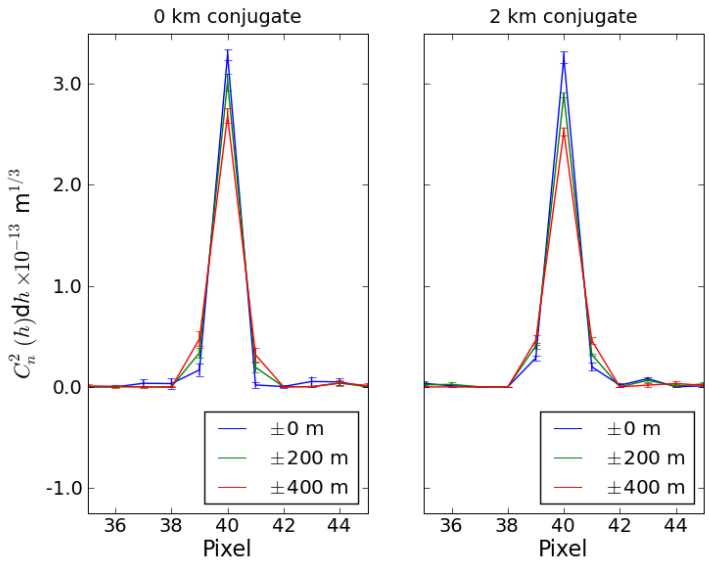

Figure 4.10: The effects of misconjugating the two detectors of the S-SCIDAR instrument. The titles of the figures correspond to the assumed conjugate altitude.

	4 km propagation		2 km propagation	
misconjugation (m)	Peak	Integrated	Peak	Integrated
0	100%	100%	100%	100%
±200	95%	99%	88%	96%
±400	82%	99%	77%	87%

Table 4.2: The effect of misconjugating S-SCIDAR on the peak and integrated turbulence for a single layer. The peak and integrated turbulence are compared to the profile for no misconjugation.

distance. For the 4 km propagation distance there is minimal reduction in the integrated turbulence, however for a ±200 m misconjugate the peak is reduced by 5%, and for ±400 m the peak reduces by 18%. For the 2 km propagation a misconjugation of ±400 m, the peak in the profile is reduced by 23%, and the integrated strength to 87%. It is clear that for accurate measurement of the turbulence profile the instrument must be conjugated as accurately as possible, especially for short propagation distances. One effect that can also be noted is the broadening of the measured profile due to this misconjugation, as the shape (as well as the altitude) of the cross covariance peak differs from that of the response function.

4.4.5 Effects of β on S-SCIDAR

The current SCIDAR response functions are derived assuming a Kolmogorov model of turbulence. However as we will see in the discussion on SLODAR in section 6.3.1 values for β have been measured to be less than 11/3. There is evidence that this is a result of improper averaging of the centroid data, especially for lower wind speeds. However if this effect is a physical property of the atmosphere, it is useful to investigate how the S-SCIDAR responds to such conditions. The generalised power spectrum for turbulence is defined in equation 2.13, however it is useful to rewrite it using Rao *et al.*'s formulation [15],

$$\Phi_\phi(\kappa) = B_\beta \Omega_n^2(h)\, \kappa^{-\beta}. \tag{4.9}$$

In the above equation β is the power law, $\Omega_n^2(h)$ is the index structure constant along the path of propagation, and has units $\mathrm{m}^{3-\beta}$, and B_β is a normalisation constant to keep consistency between the power spectrum and structure function. In the case of Kolmogorov turbulence $\Omega_n^2(h) \equiv C_n^2(h)$. The constant B_β is defined for a given β as

$$B_\beta = \frac{1}{4\pi^2}\Gamma(\beta-1)\sin\left(\pi\left(\frac{5-\beta}{2}\right)\right) \qquad (3<\beta<4). \tag{4.10}$$

We can now present a modified expression for $B_h(r,h)$ (equation 4.6) for generalised power spectrum,

$$B_h(r,h,\beta) = 1.2\times10^{-1} 2\pi k^2 \Omega_n^2(h)\, B_\beta \int_0^\infty f^{1-\beta}\sin^2\left(\pi\lambda h f^2\right) J_0(2\pi r f)\,\mathrm{d}f \tag{4.11}$$

and then the response functions can be calculated from 4.7 as before.

Two examples of SCIDAR response functions are shown in figure 4.11, one with $\beta = 3.667$, and the other with $\beta = 3.222$, both for a single layer with equivalent integrated $\Omega_n^2(h)$, and the result of fitting the Kolmogorov response to non–Kolmogorov turbulence. The example here considers turbulence with an altitude of 8 km, however the profile and responses are both normalised. We see that the non–Kolmogorov response has a lower amplitude than the Kolmogorov case, however the 'side lobes' match very well. The comparison of profile fitting shows that fitting a Kolmogorov response to non–Kolmogorov turbulence leads to an

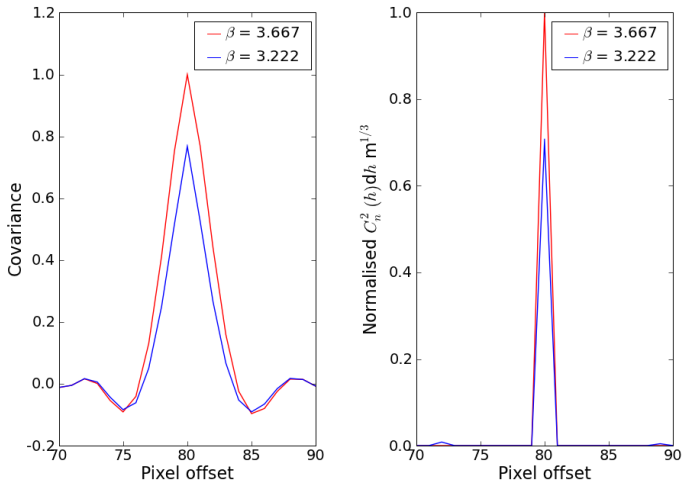

Figure 4.11: Comparison of Kolmogorov and non Kolmogorov responses (left), and profile fitting (right) for S-SCIDAR. Note the non–Kolmogorov response has a smaller amplitude than the Kolmogorov, however the shapes of the side lobes of the two responses have good agreement. When Kolmogorov responses are fitted to non Kolmogorov turbulence, we see an underestimation of turbulence strength, and two small side lobes either side of the central peak.

underestimate of turbulence strength, and two small side lobes around the central peak. In this particular example the side lobes are 1.1% of the amplitude of the centre peak. This however is only one example. In figure 4.13 we show a comparison of a set of response functions for different β values. These response functions have an integrated $\Omega_n^2(h)$ of 100 m$^{4-\beta}$ and generated for a -2 km conjugate, and the value of the peak of the response function is plotted. We see that for $\beta > 3.444$ the values differ only minimally, and even for $\beta = 3.333$ with a 14.8 km propagation distance the non–Kolmogorov response is only suppressed by 12%. We conclude that in the case of S-SCIDAR observing non–Kolmgorov turbulence, the effect would be an underestimation of integrated turbulence strength, but with no significant distortion of the relative turbulence profile.

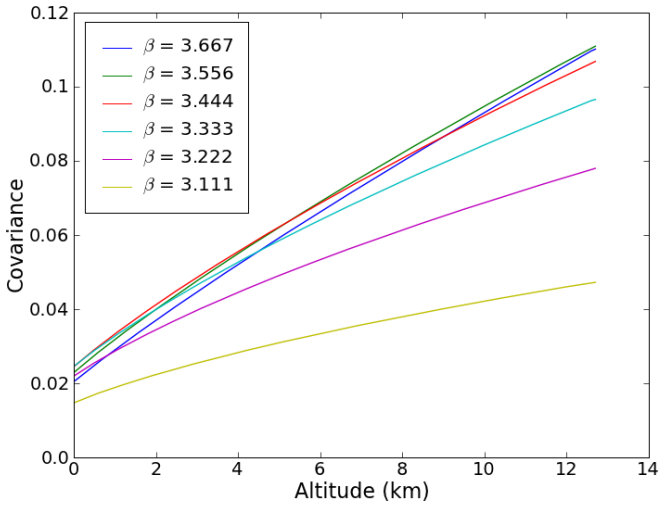

Figure 4.12: Suppression of the S-SCIDAR response functions for different β values. The examples shown has a conjugate altitude of -2 km, and the peak response values for a single layer with integrated $\Omega_n^2(h)$ of 100 $\mathrm{m}^{4-\beta}$ is plotted. For $\beta > 3.444$ the responses are in good agreement with the Kolmogorov case, and for $\beta = 3.333$ the suppression of the response for a 12.8 km layer is only 12%.

4.5 Comparison with G-SCIDAR

4.5.1 Simulation and data reduction of G-SCIDAR simulations

Generalised SCIDAR can be simulated with only a small modification to the method discussed in section 4.4. After the two pupil images are formed, each one is further propagated to ensure a -2000 m conjugate altitude, and the two pupil images are superimposed on a detector, separated by a distance corresponding to $x = h_{\mathrm{conj}}\theta$. Unlike the S-SCIDAR discussed above, the profile is retrieved from an autocovariance as opposed to the cross covariance, and hence the central peak will contain a noise term in addition to the scintillation signal. The data are normalised using the method explained in Klückers *et al.* [73]. For this reason, when the G-SCIDAR response functions are fitted to the autocovariance data, the central peak is omitted from the fit.

The G-SCIDAR response functions have a distinctive shape, with a central peak and two side lobes. The side lobes are equivalent to the peaks in the S-SCIDAR response, and the pair of peaks is a consequence of the symmetry of the autocovariance. The measured

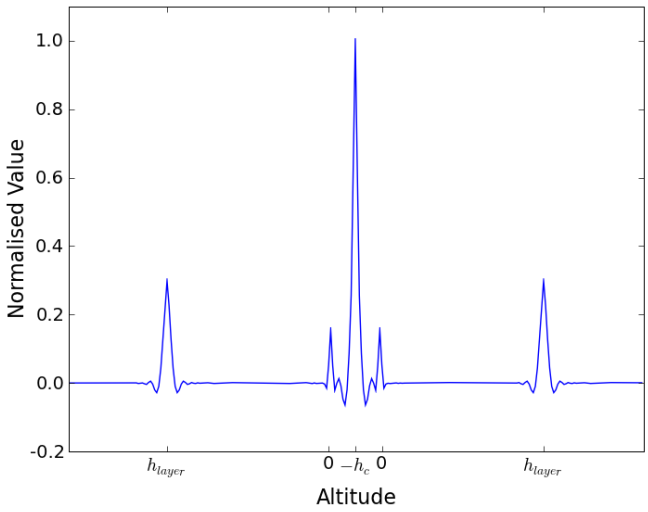

Figure 4.13: A slice through a G-SCIDAR autocovariance for a two layer atmosphere, with layers at the ground and h_{layer}. In this example $\Delta m = 0.5$, and the ground layer is twice as strong as the high layer. The central peak in the autocovariance contains information about both layers, and note in this example it has an effect on the peak corresponding to the ground layer. (h_{c} corresponds to the conjugate altitude of the G-SCIDAR.)

double star autocovariance for G-SCIDAR is

$$\begin{aligned} B_{**}(r,\theta) &= \int_h C_n^2(h)\Big[aB'_h(r, h-h_{\text{conj}}) \\ &+ b\big\{B'_h(r-\theta(h-h_{\text{conj}}), h-h_{\text{conj}}) \\ &+ B'_h(r+\theta(h-h_{\text{conj}}), h-h_{\text{conj}})\big\}\Big]\mathrm{d}h, \end{aligned} \tag{4.12}$$

where $B'_h(r,h)$ is the intensity fluctuation cross correlation for unit turbulence strength as defined in equation 4.6. The coefficients a, and b scale the response functions to the difference in intensities between the two pupil images, and

$$a = \frac{1+\alpha^2}{(1+\alpha)^2}, \qquad b = \frac{\alpha}{(1+\alpha)^2}.$$

In the equations above $\alpha = 10^{-0.4\Delta m}$, where Δm is the difference in stellar magnitudes of the binary pair. An example of a slice through a G-SCIDAR autocovariance for a two layer atmosphere is shown in figure 4.13.

4.5.2 Example simulation results from G-SCIDAR

Our hypothesis is that the S-SCIDAR method can more accurately resolve closely spaced turbulent layers in the atmosphere than the existing implementation of G-SCIDAR. Figure 4.14 shows example two layer atmospheres for four different separations of turbulent layers, each with equal strength of 270×10^{-15} m$^{-1/3}$ in each layer. The simulation parameters are chosen to correspond to the S-SCIDAR simulations above, with layer separations of 201.4 m, 302.1 m, 352.4 m and 402.8 m, corresponding to 1, 2, 2.5 and 3 pixels in the cross covariance respectively. We choose $\Delta m = 1$.

With layer altitudes corresponding to adjacent pixels there is no evidence for a two layer atmosphere, as for the separation of 2 pixels. When the separation is increased to 2.5 we see two distinct layers, however the fitting introduces an artefact where the turbulence strength appears to 'bleed' over two bins. We conclude that the resolution for G-SCIDAR is inferior to that for S-SCIDAR, where it is possible to resolve between layers that have a less than 2 pixel separation, as predicted from equation 4.1. In the plots for both the 2.5 and 3 pixel separations the implications of fitting the wide response functions to two layers can be observed as it is impossible to conclude whether these layers are thin or have vertical structure. The measured integrated turbulence strength between each of these plots varies by more than 10%, far larger than that expected from the standard error.

4.6 On sky example

An example of the capabilities of the S-SCIDAR technique can be seen from the prototype instrument mounted on the Nordic Optical Telescope, the design of which can been seen in figure 4.15. Due to adverse weather conditions only a small amount of data could be taken on the night of 24th September 2010. The star pair observed during these measurements has a separation of 34.2 arcseconds, yielding a maximum sensing altitude of 15400 m, with each pixel in the covariance corresponding to 116 m. The data was taken at a range of conjugate altitudes, however due to the effects of wind shake on the telescope only data taken at conjugates of -2, 0, and 10 km were suitable for profile fitting.

The results of this profile fitting are shown in figure 4.16. The figure shows a layer of

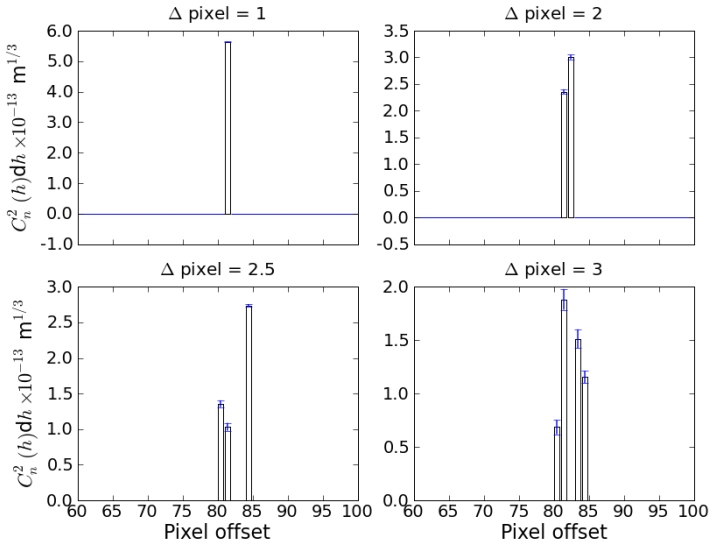

Figure 4.14: Example simulated profiles of G-SCIDAR measuring a 2 layer atmosphere, with a -2 km conjugate latitude. Clockwise from upper left there are separations of 201.4 m (1 pixel), 302.1 m (2 pixels), 352.4 m (2.5 pixels), and 402.8 m (3 pixels). The layer is resolved for separations of greater than 251 m, although integrated turbulence strength is not conserved between measured profiles.

turbulence at approximately 7 km throughout the measurement period, intermittent earlier on, and then becoming dominant. The layer appears for all the conjugate altitudes as expected. In addition for the -2 and 10 km conjugate zones, we see a thin but strong ground layer. After -0.4 hours UT, a sudden shift in the distribution of the free atmosphere turbulence can be observed. The layers at 6 km, and 7 km appear to invert their strength.

The transition between -2 km, and 0 km conjugate appears to occur seamlessly, however there is an error in the adjustment between 10 and -2 km. The ground layer appears in the correct location in both, however the free atmosphere turbulence appears to be displaced by +1 km, evidenced by matching the $\sim$ 7 km and $\sim$ 12 km turbulent layers. During this time, there was a high degree of wind shake on the telescope, and so each cross covariance frame had to be re-centred, potentially introducing this error when the profile was fitted.

We can now look further at the profile, and demonstrate that these signals do all arise from genuine turbulent layers, rather than from some instrumental artefact. For the entirety of the -2 km conjugate data, a covariance matrix was calculated and shown in figure 4.17.

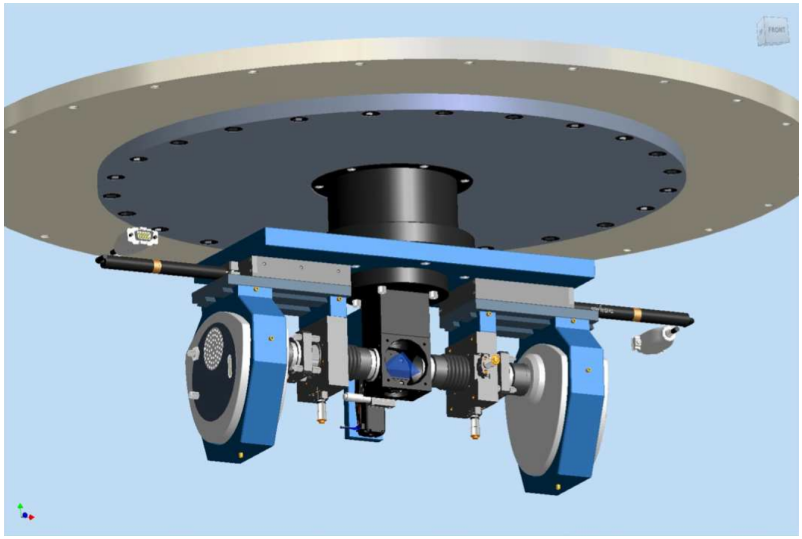

Figure 4.15: Diagram of the conjugate-plane photometer from which the S-SCIDAR measurements were made. The reflecting prism can be seen in the centre, and the two arms contain the re-conjugating optics, leading into two Andor Luca cameras. The device is shown mounted on the Cassegrain focus of the NOT. Image from [74]

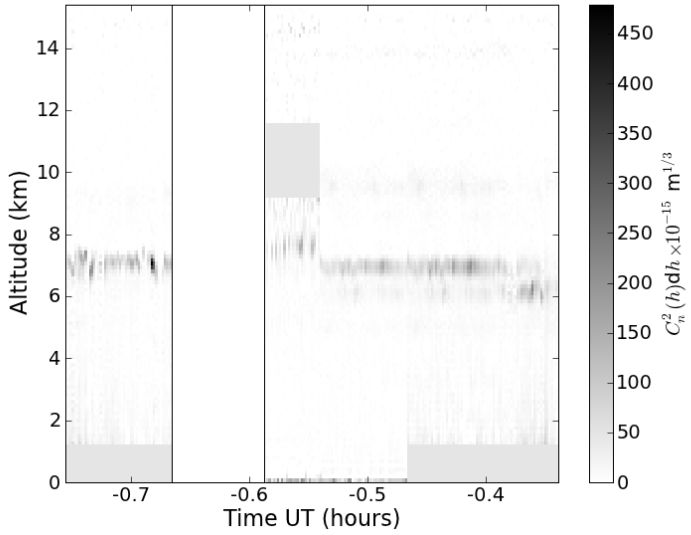

Figure 4.16: Profile of the NOT S-SCIDAR for several conjugate altitudes between 23:15 and 23:40 UT, 24th September 2010. Between -0.76 and -0.66 hours UT, the conjugate altitude was 0 km, between -0.59 and -0.54 hours UT the conjugate was 10 km, -0.54 to -0.47 hours -2 km, and -0.47 to -0.34 hours another set of measurements at 0 km. Note the shaded regions for ± 1 km around the conjugate altitudes. These regions are not fitted, because the relevant response functions have a value of zero, and therefore an inverse is undefined in these regions.

In the first frame, the centre pixel corresponds to a ground layer of turbulence, and altitude increases in the downward direction. In this frame, we see seven distinct layers of atmospheric turbulence. In subsequent frames an increasing temporal offset is introduced into the cross covariance and each of these peaks shows behaviour indicating genuine turbulence. These layers all exhibit translational motion, and additionally each layer exhibits either wind shear, as shown by the peaks splitting into two turbulent layers of differing velocities, or dispersion, shown by the layer 'blob' expanding over the cross covariance movie. This high clarity is due to the fact that it is possible to normalise both stellar scintillation images before taking the covariance. The clarity is not the only advantage the independent normalisation brings, Avila and Cuevas note that in the case of G-SCIDAR a separation of 1 stellar magnitude between the double star pair can lead to a 21% error in the turbulence profile [70]. The S-SCIDAR is limited only by signal, meaning larger stellar magnitude separations can be used, increasing the number of potential targets available.

An average profile is fitted to this covariance, shown in figure 4.18, showing two dominant turbulent layers and many weaker layers, including the complex structure of the turbulent atmosphere up to 10 km. The errors are calculated from the standard error from the time averaged cross covariance.

More data is required to demonstrate the technique showing increased resolution.

4.7 Conclusion

This chapter presents a modification of SCIDAR christened Stereo SCIDAR (S-SCIDAR). The light from each star is incident on two separate CCD detectors, by means of a reflecting prism, and the altitude conjugate for each arm can be set dynamically. The covariance map is then generated using a cross covariance as opposed to auto covariance, so that no correlated noise (for example the effects of shot noise) is introduced. As the intensity patterns on each detector can be normalised independently, stars with quite different magnitudes can be used. Response functions for this form of SCIDAR are calculated and verified against simulation.

We show using simulation that the re–conjugation technique allows the identification of closely spaced turbulent layers, and the closer one can conjugate to these layers the more

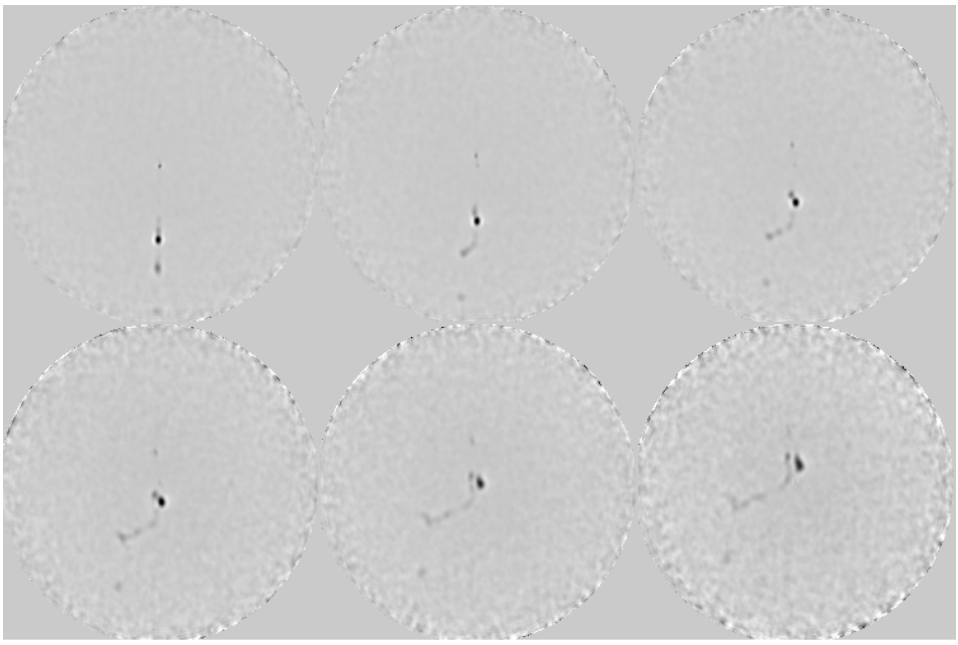

Figure 4.17: Cross covariance movie for the NOT S-SCIDAR. The image in the top left corner corresponds to zero temporal offset, and the offset increases from left to right. The centre pixel corresponds to zero altitude, and increasing altitude in a downward direction, clearly showing several layers of atmospheric turbulence. As the temporal offset increases, each layer demonstrates either wind shear or dispersion. The different frames have been independently scaled for clarity. The corresponding turublence profile for this covariance map is shown in figure 4.18

.

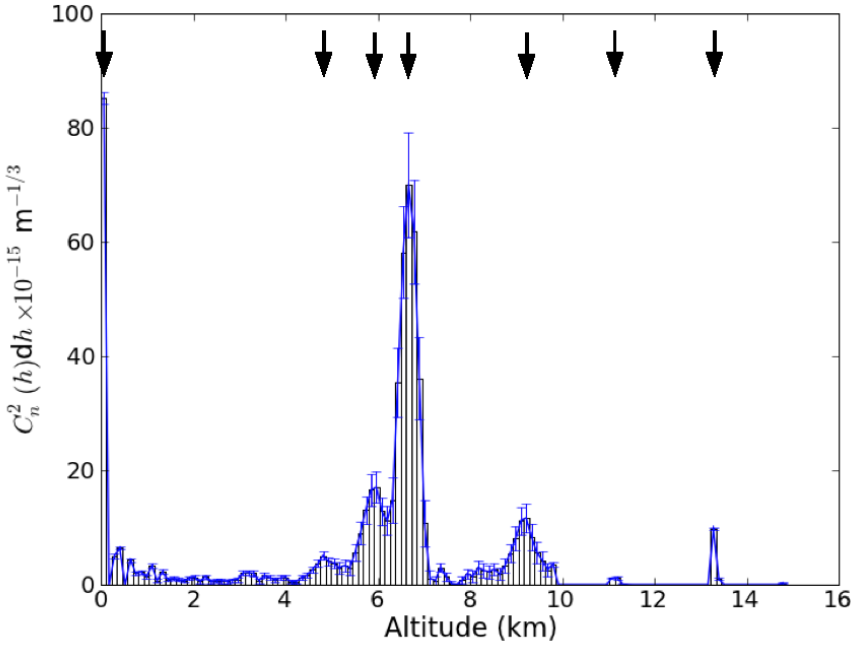

Figure 4.18: Example turublence profile from the NOT S-SCIDAR for a -2 km conjugate altitude, using the covariance map shown in the top left panel of figure 4.17. The complex structure of the turbulent atmosphere at this time can clearly be seen, including two dominant layers, one at the ground, and one at 6.5 km. Additionally a number of weak layers are resolved in the profile. The resolved layers are confirmed by observing their translational wind velocities in the spatio–temporal cross covariance and are indicated by the arrows.

marked the separation. It is also shown that it allows close layers of non equal strengths to be resolved. If the detectors are misconjugated relative to each other then the altitude of the turbulence can still be retrieved, however the peak and integrated turbulence strength is underestimated. The the peak strength is reduced by more than the integrated strength.

The effect of non Kolmogorov power spectra ($\beta < 11/3$) on the SCIDAR instrument is investigated by generating response functions for non Kolmogorov turbulence. The non Kolmogorov response functions have reduced amplitude, however the shape of the 'side lobes' still match well. The only significant effect for fitting Kolmogorov response to non Kolmogorov turbulence will be an underestimation of turbulence strength, and we show that this only has a significant effect for $\beta < 3.444$.

Finally we present a limited on sky example application of this technique, and a covariance matrix showing seven turbulent layers. The layers are verified to be genuine turbulence by adding a temporal offset to the covariance leading and observing either wind shear or dispersion. A turbulence profile is presented for the limited time on sky.

Chapter 5

Whole Atmosphere SLODAR

5.1 Introduction

The current SLODAR methodology does not account for the effects of propagation on the response functions, or on measurements of seeing taken directly from centroid variance. For previous SLODAR systems, such as the SL-SLODAR [47] and the measurements of the Ground Layer at Mauna Kea [75] and SALT [76] this has not had a significant effect, as the effects of Fresnel propagation require of order 2 km to fully develop. However when profiling the whole atmosphere, these propagation effects become significant. Two modifications to the SLODAR technique are proposed: the first is fitting response functions calibrated for Fresnel propagation; the second is fitting both the strength and altitude of turbulence above the direct sensing range using the centroid variance as well as scintillation data from the spots of the Shack Hartmann patterns.

Védrenne *et al.* have also proposed turbulence profiling techniques using both phase and scintillation data with techniques such as Coupled SLODAR-SCIDAR (CO-SLIDAR). Their technique uses the covariance of both the scintillation and phase data from Shack Hartmann wavefront sensors to recover the turbulence profile for directly sensed altitudes, yielding increased altitude resolution [77]. The complimentary method described here uses the phase covariance and scintillation variance simultaneously to measure high altitude turbulence in the region **above** the maximum altitude for direct (crossed beams) profiling.

It is useful to recall two key results from the introduction. If a turbulent layer at altitude h is measured from the ground then the effects of propagation cause suppression of the PSD of phase aberrations at spatial frequencies corresponding to the layer's Fresnel length $r_f = (\lambda h)^{1/2}$. The measured power spectrum at the ground is given by

$$W_{\phi_0}(f) = 9.7 \times 10^{-3} k^2 f^{-11/3} \int_0^\infty C_n^2(h) \cos\left(\pi \lambda h f^2\right) \mathrm{d}h. \tag{5.1}$$

Fresnel propagation also leads to fluctuations of intensity at the ground known as scintillation. For small apertures such as the subapatures of a Shack Hartmann sensor, the scintillation index (intensity variance) can be related to turbulence strength and height as

$$\sigma_I^2 = 19.2 \lambda^{7/6} (\cos\gamma)^{11/6} \int_0^\infty h^{5/6} C_n^2(h) \mathrm{d}h. \tag{5.2}$$

where γ is the zenith angle of the target [8].

5.2 Methodology

5.2.1 Calculating propagation corrected SLODAR Impulse Response Functions (SIRFs)

The theoretical covariance of wavefront slopes between two apertures can be expressed as an integral involving the phase structure function $D_\phi(\boldsymbol{r})$ of the phase aberrations. In the case of SLODAR the phase is measured relative to the aperture mean, as piston has no effect on a Shack Hartmann sensor. Tip-tilt subtractions are also made, averaged across the telescope aperture, to remove any common motion, for example telescope tracking error and wind shake. The method for generating response functions from the phase structure function is described in [54], and is followed in this work.

As there is no theoretical form for a structure function corresponding to the modified power spectrum, one must be calculated [78]. A brief method is outlined below. The power spectra defined in equation 2.32 is for two dimensional fields. We define a 1-D energy

spectrum by performing the circular integral

$$E_{\phi_0}(f) = \int_0^{2\pi} W_{\phi_0}(\boldsymbol{f})\, f \mathrm{d}\theta. \tag{5.3}$$

If the field is statistically isotropic then $W_{\phi_0}(\boldsymbol{f}) = W_{\phi_0}(f)$, so $E(f) = 2\pi k W(f)$. A modified form of the Wiener-Khinchin theorem is used to calculate a structure function which accounts for the effects of Fresnel propagation. The theorem states that the power spectrum is a Fourier transform of the autocorrelation function of a field. For a 2-D field the structure function is

$$D_\phi(\boldsymbol{x}) = 2 \iint_{R^2} \left[1 - \cos\left(2\pi \boldsymbol{f} \cdot \boldsymbol{x}\right)\right] W_{\phi_0}(f)\, \mathrm{d}\boldsymbol{f}. \tag{5.4}$$

Now the vector notation is substituted with a polar representation, where $\boldsymbol{x} = \binom{x_x \cos\phi}{x_y \sin\phi}$ and $\boldsymbol{f} = \binom{f_x \cos\theta}{f_y \sin\theta}$

$$D_\phi(\boldsymbol{x}) = 2 \iint_{R^2} \left[1 - \cos\left(2\pi f x \cos\left(\theta - \phi\right)\right)\right] W_{\phi_0}(f)\, f \mathrm{d}\theta \mathrm{d}f. \tag{5.5}$$

Using Parseval's integral, and substituting the scalar power spectrum we can define an expression for the corrected structure function

$$D_\phi(\boldsymbol{x}) = 4\pi \int_0^\infty \left[1 - J_0\left(2\pi f x\right)\right] f W_{\phi_0}(f)\, \mathrm{d}f. \tag{5.6}$$

This modified structure function is used to generate the SIRFS, as discussed in section 5.3.1.

5.2.2 Fitting unresolved turbulence

By taking the auto-covariance of the centroid motion for each of the Shack Hartmann patterns from the SLODAR instrument, the total turbulence strength is contained within the data, whereas the cross covariance contains information only up to the maximum sensing altitude sampled by the crossed beam. The scintillation index can also be measured from the intensity variance of the spots in the Shack Hartmann images. We know the $C_n^2(h)$

values and the approximate turbulence heights for each layer from the SLODAR data reduction, and this allows us to calculate the residual variance of the scintillation contributed by unresolved turbulence as follows,

$$\sigma_I^2\,(\text{unres}) = \sigma_I^2 - 19.12\lambda^{7/6}\sum_{i=1}^{n} {h_i}^{5/6} C_n^2\,(h_i) \tag{5.7}$$

$$= 19.12\lambda^{7/6} h_{\text{unres}}^{5/6} C_n^2\,(h_{\text{unres}}) \tag{5.8}$$

where σ_I^2 is the measured scintillation index, n is the number of SLODAR bins, and h_i is the height of the centre of the i^{th} bin. By assuming that the unresolved turbulence is contained within a single layer, and by measuring the scintillation index an estimate can be made for the product $h_{\text{unres}}^{5/6} C_n^2\,(h_{\text{unres}})$. Although the value for this expression can be determined it is a product of two unknowns, and so further processing must be done to provide estimates for these two values.

The SLODAR auto covariance response functions corresponding to the turbulence strength in the resolved profile are subtracted from the measured auto covariance, leaving a residual from the unresolved turbulence. SIRFSs of varying heights h_{test} above the resolved region are fitted to this residual auto covariance, giving an estimated value for $C_n^2\,(h_{\text{test}})$, from which $h_{\text{test}}^{5/6} C_n^2\,(h_{\text{test}})$ can be then be calculated. We can then calculate scintillation indices for these test quantities, and construct a set of χ^2_{test} values corresponding to each of these strength altitude pairs. The minimum χ^2_{test} value is used as the estimator for the strength and altitude of the turbulent layer.

A flowchart illustrating this process is shown in figure 5.1.

5.3 Results

5.3.1 Corrected SIRFs

The corrected SIRFs were generated using the method outlined in the paper of Butterley *et al.* [54]. The structure function was generated using equation 5.6. As no analytic solution for this integral could be found, it was performed numerically using a trapezium rule method. As the modified power spectrum is unique for turbulence of a given height, it is necessary to

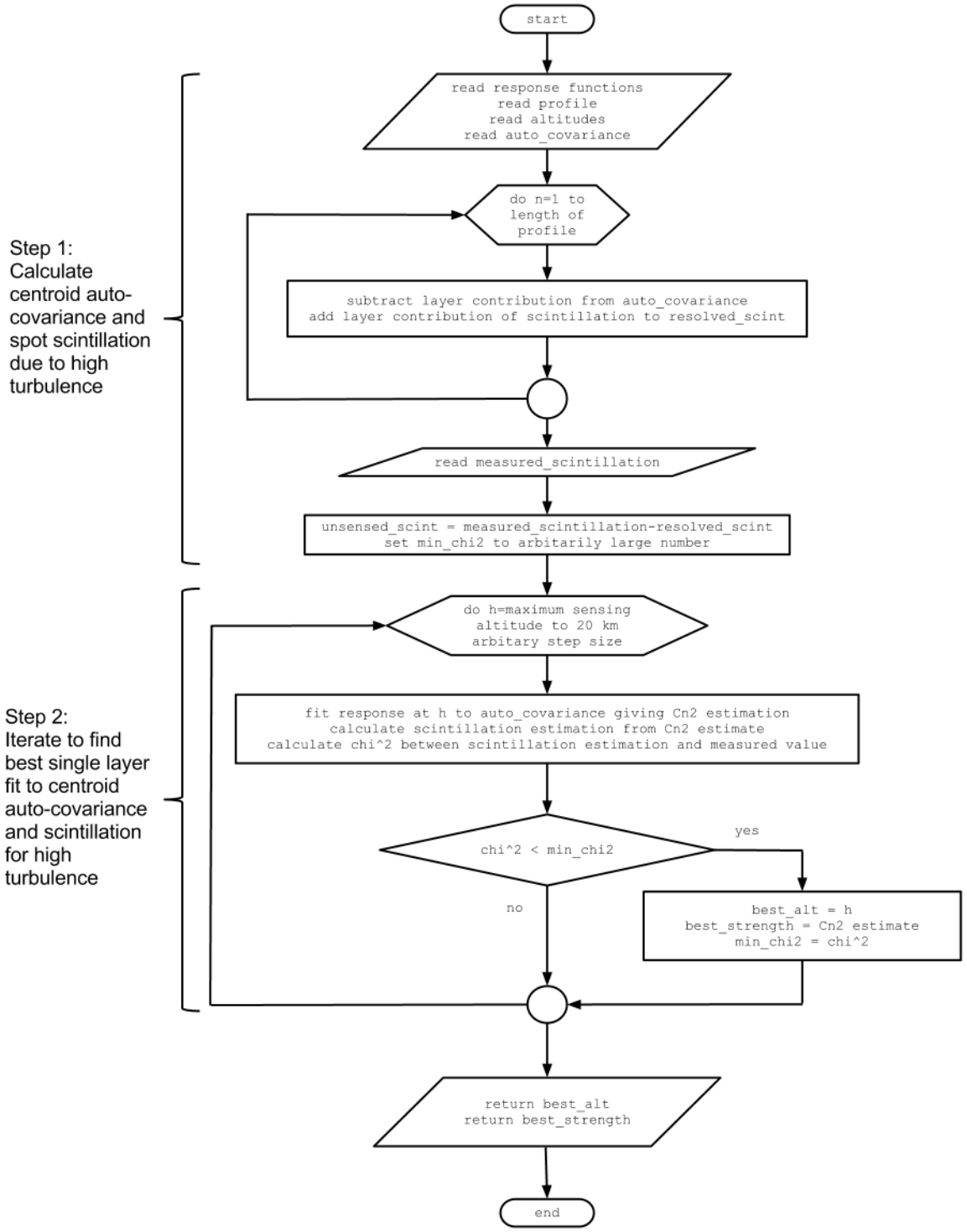

Figure 5.1: Flowchart showing the fitting method for FA-SLODAR.

generate a structure function for every bin height (which changes as the telescope tracks over the sky). For each height, the structure functions are calculated for separations up to 3 times the telescope diameter, with 8 data points per sub-aperture to ensure adequate sampling. The integration limits were chosen to be the inertial range of atmospheric turbulence, i.e. between $1/l_0$ and $1/L_0$. For the data presented below, 10 m was chosen for the outer scale, and 1 mm for the inner scale, but the effect of misestimating the outer scale will be presented later in this section. A comparison of the uncorrected and corrected response functions is shown in figure 5.2, for a SLODAR system on a telescope with an effective diameter of 38 cm with 8×8 sub-apertures, with a resultant sub-aperture diameter of 4.75 cm. A double star width is chosen such that the height resolution is 1 km. These parameters were chosen to match a SLODAR instrument deployed on La Palma in the latter half of 2010. The effect of propagation is immediately noticeable on the response functions: the peak value is decreased and the responses are broadened. This corresponds to a reduction in the contribution to centroid variance from high layer turbulence. This figure also shows a comparison of the corrected SIRFS with Monte-Carlo simulations and the calculated and simulated SIRFS are shown to be in good agreement.

Orthoganality plots for the Fresnel corrected SIRFS are shown in figure 5.3. The plots clearly show the asymmetric nature of the corrected response functions, and whilst there is some altitude dependence on the response functions as illustrated in figure 5.2, the response functions are close to orthogonal. This allows the generalised inverse of the matrix of response functions to be used to fit a turbulence profile to the measured cross covariance. The invertability of these matrices of response functions has been explicitly checked. These particular responses are generated for a sub aperture size of 4.75 cm, and for an altitude of 1000 m per sub aperture offset.

Effect of the outer and inner scale on corrected SIRFs

The numerical integral to generate the structure function is performed over an inertial range corresponding to the spatial frequencies of $1/L_0$ and $1/l_0$, and then further processed using Butterley's method [54] to generate a response function. However, as the values for the inner and outer scales vary within some typical range, any effects on the impulse response

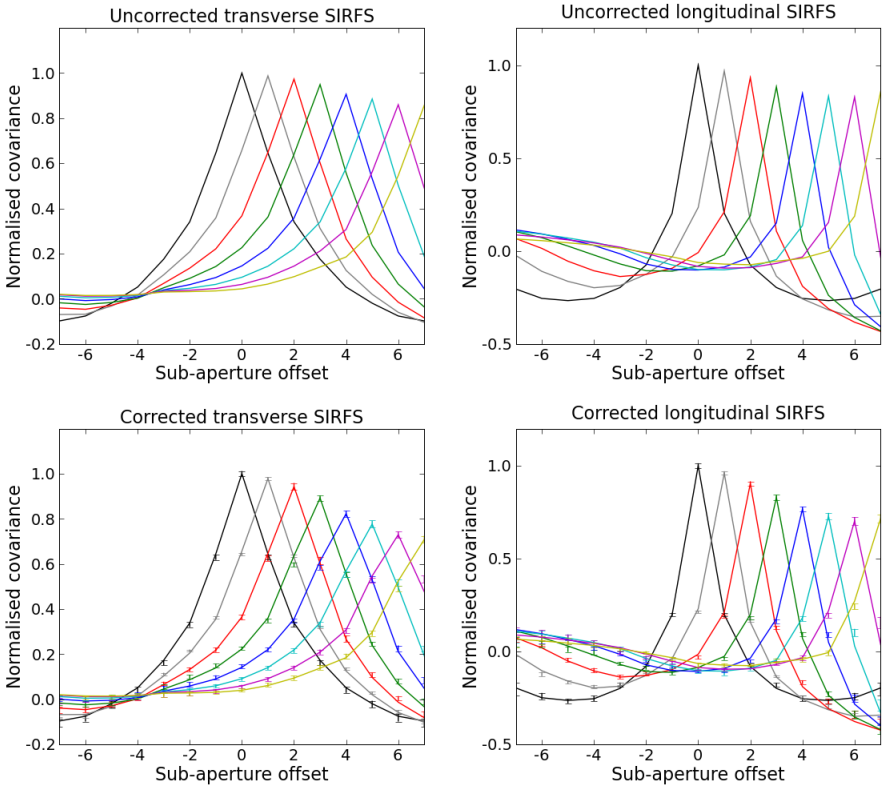

Figure 5.2: A comparison of SLODAR Impulse Response Functions with and without Fresnel propagation correction. Each sub-aperture offset corresponds to an increase in altitude of 1 km. The top two figures show the response functions derived without any propagation effects, and the bottom two figures show the response functions with those effects included. The solid lines show data from the numerical integration of the structure function, and the data points are the results from Monte-Carlo simulation. The reduction in peak values and broadening relative to the non–propagated case can be seen.

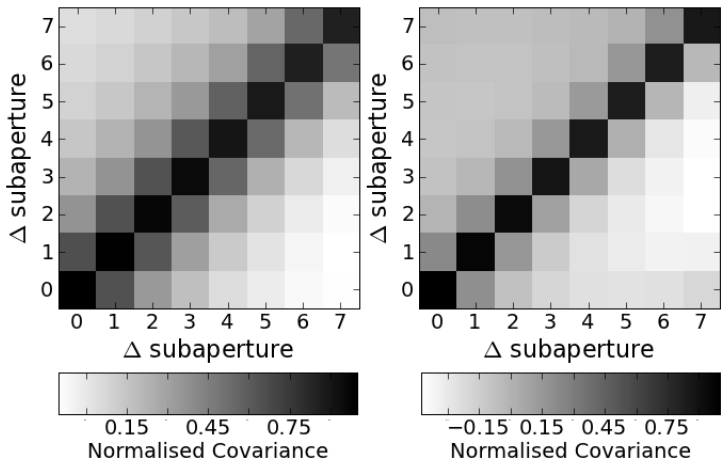

Figure 5.3: Orthoganality plots for Fresnel corrected SIRFS, transverse (left) and longitudinal (right). The response functions were generated for an altitude of 1000 m per sup aperture offset.

functions must be investigated.

A large range of measured values for the outer scale have been reported dependent on the observatory site, from 5-8 m in La Palma [79], 22 m at Paranal [10], with the outer scale thought to reach 100 m at the edge of the troposphere [8]. SLODAR response functions are calculated with limits corresponding to $l_0 = 4$ mm, and $L_0 = 4$, 8, 20, and 100 m to span the values from literature. We verify that for this range of outer scales, there is negligible effect on the SIRFS. The results are presented in figure 5.4.

The values for the inner scale are more constrained however, from the order of 1 mm at the ground to 1 cm at the top of the troposphere. Again we generate different values for the SIRFs, with constant $L_0 = 16$ m, and $l_0 = 0.1$, 1, and 10 mm. It can be seen that there is negligible effect on the form of the SIRFs. Any large effect only occurs when the inner and outer scales are of the same order as the sub-aperture diameter. This is only relevant for small sub-apature diameters, common when using small telescopes, or high order wavefront sensors, as the Fresnel propagation effects are averaged out when using larger sub-apatures. Provided that sub aperture diameters larger than the inner scale and smaller than the outer scale are chosen, there is no significant effect on the form of the SIRFS.

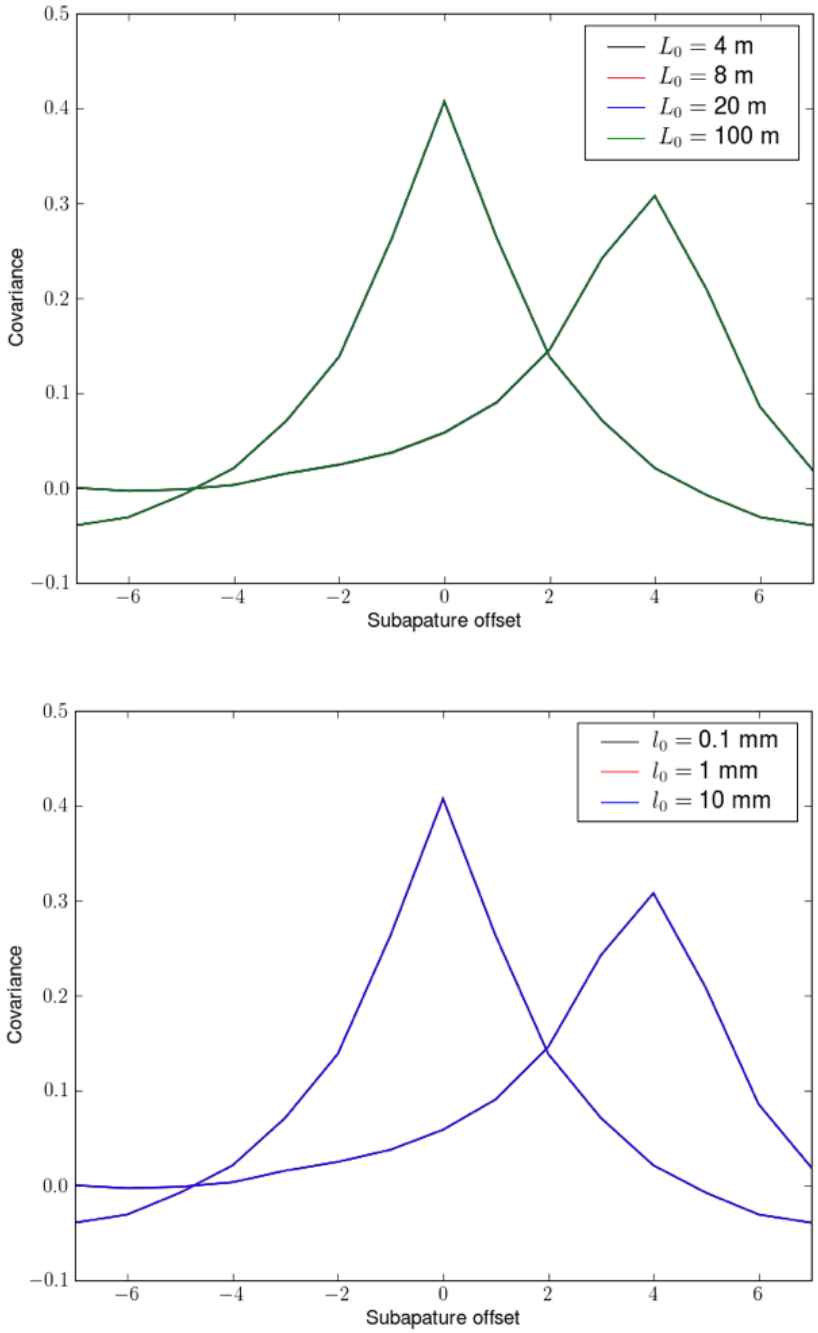

Figure 5.4: Effect of differing inner and outer scale on the generation of SLODAR impulse response functions, showing the ground and 4 km response for clarity. The upper figure shows differing outer scales with a constant inner scale of 4 mm, and the lower shows differing inner scales at a constant outer scale of 16 m. There is no appreciable variation of the SIRFs visible in either case.

Fitting the corrected SIRFs

Having presented corrected SIRFs, it is necessary to fit these response functions to some sample SLODAR data to check for an improved fit. As a result of the difference in shapes between the corrected and uncorrected response functions, we can hypothesise that fitting a high atmosphere layer with the uncorrected response should lead to an underestimation of turbulence strength, and a broadening of the fit, causing it to smear into neighbouring altitude bins. As we can not perform this test on sky (as it is not possible to know beforehand the strength of the turbulent layers), again Monte-Carlo simulations are used.

Figure 5.5 shows the effects of fitting old and new SIRFs on an atmospheric model picked to show the key features of the fit. This model contains two turbulent layers, one at the ground and one at 4 km. For a turbulent layer at the ground the new and old response functions fit the same turbulence strength, as is expected because there is no propagation distance for any Fresnel effects to occur. For higher layers it can be seen not only that the peaks for the new response functions have the correct amplitude, but also in the fitted profile the peaks are narrow, and bins where there is no turbulence have a value of zero. This contrasts with the fit using the old response functions where the peaks in the profile are greatly reduced, smear into adjacent bins, and often have negative values somewhere in the profile.

5.3.2 Fitting un-sensed turbulence

We now verify the method to fit free atmosphere turbulence, using the SIRFs generated above, along with propagation corrected responses for the auto covariance. Again this is verified against the Monte-Carlo simulation, both to check the calibration and to fit profiles.

Checking calibration for altitude and strength

It is first necessary to check the calibration for fitting the unresolved layers. The SLODAR setup modelled has an altitude resolution of 1000 m, and a maximum resolving altitude of 7000 m (to match typical parameters expected from the system on La Palma described in section 5.3.1). To check the altitude fitting, first we consider single layer profiles. Turbulence

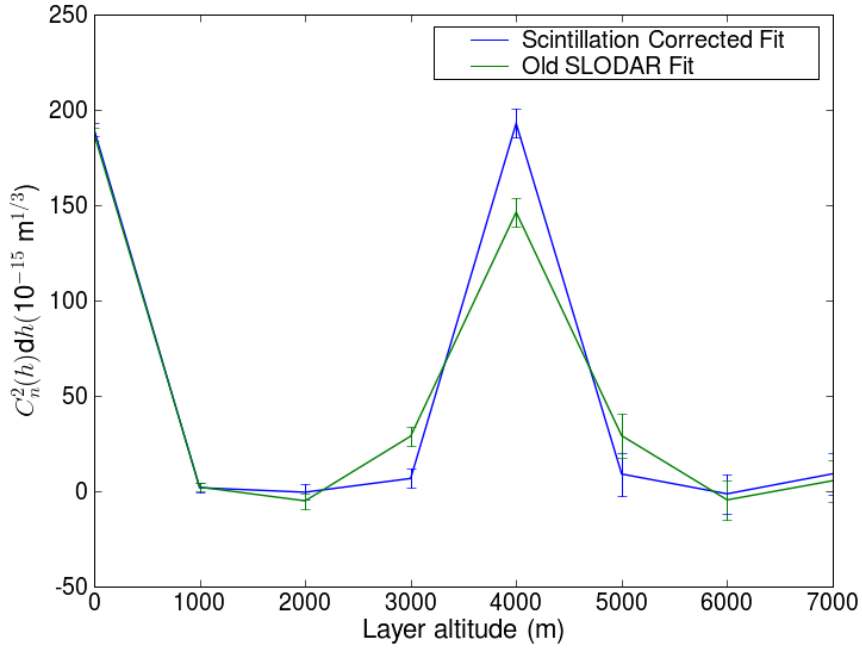

Figure 5.5: Fitting Fresnel and non Fresnel corrected impulse response functions to a two layer atmosphere (0km and 4km), with a strength of 193×10^{-15} $\mathrm{m}^{1/3}$ per layer. Both responses cause a correct fit for the ground layer as there is no propagation distance, but the old response underestimates the turbulence strength by approximately 25%. The new response functions also reduce the effect of broadening of the turbulence profile.

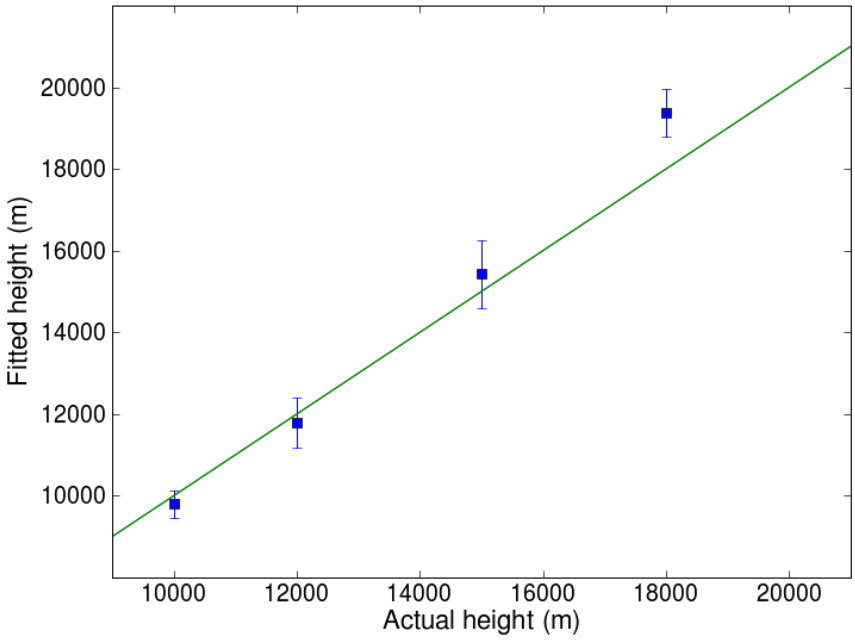

Figure 5.6: Fitting the height of a single layer of unresolved turbulence using corrected impulse response and scintillation variance. The maximum direct sensing altitude of the SLODAR system modelled is 7 km

of strength of 385×10^{-15} $m^{1/3}$ at altitudes of 10, 12, 15, and 18 km was modelled, and is shown in figure 5.6. It can be seen that for the lower unresolved layers the fitted height corresponds to the actual height within the Monte-Carlo error, and it is only at the very high 18 km layer (where there will be a high scintillation variance and low phase variance) that the altitude is overestimated. Very strong or very high altitude layers of turbulence can lead to a saturation of scintillation causing the scintillation index to deviate from the value calculated in equation 5.2. This scintillation saturation however is not normally encountered at a good observing site.

Similarly to fit the turbulence strength one layer at 10 km is chosen, with turbulence strengths of 260×10^{-15}, 356×10^{-15}, 450×10^{-15}, and 600×10^{-15} $m^{1/3}$. The current SLODAR system can provide an estimate for unresolved turbulence by subtracting the summed profile, up to the maximum profiling altitude, from an estimate of the total integrated turbulence taken from the absolute centroid variance. This is not corrected for

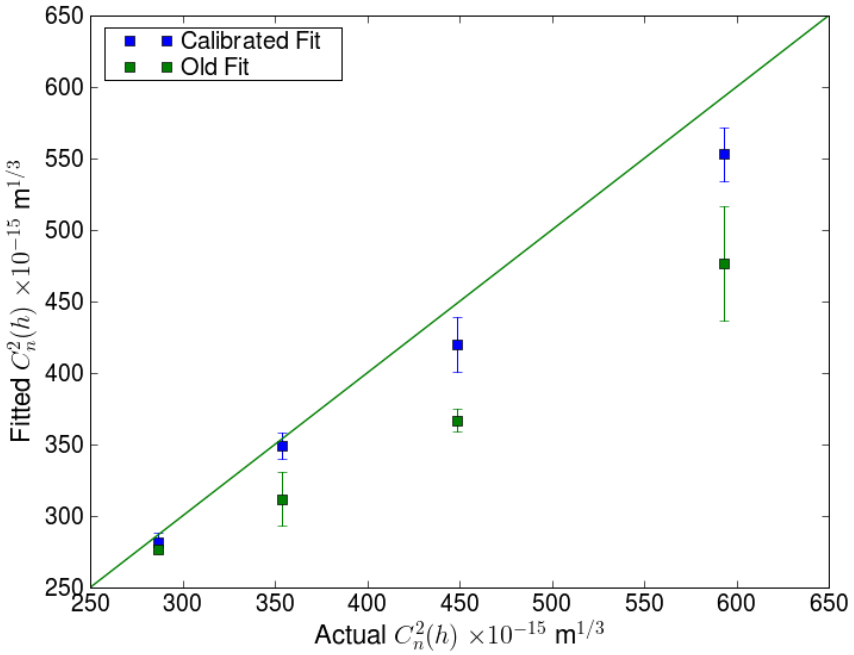

Figure 5.7: Fitting the strength of a single layer of unresolved turbulence using both corrected impulse response and scintillation variance, and also uncorrected response and absolute centroid variance as with the current SLODARs. The maximum sensing altitude of the SLODAR system modelled is 7 km

Fresnel propagation. The results are shown in figure 5.7. On this plot the estimate for the unsensed turbulence using the current method is also shown. Both methods underestimate the strength of the unresolved turbulence, but the new method provides a much closer estimate.

Fitting profiles

To test the fitting of two layer profiles (one 'sensed', one 'unsensed'), we model an atmosphere with equal strength layers of 193×10^{-15} m$^{1/3}$. The unsensed layer has an altitude of 10 km (3 km above the maximum sensing altitude of the simulated SLODAR system), and different altitudes for the sensed layers are chosen; 0, 2, 4, and 6 km. The profiles are shown in table 5.1.

The method described assumes a single turbulent layer above the maximum resolved

Input layers		Fitted High Layer	
Low Layer (m)	High Layer (m)	Fitted Height (m)	Fitted $C_n^2(h)$ ($m^{1/3}$)
0	10000	10198 ± 860	$(179 \pm 13) \times 10^{-15}$
2000	10000	9531 ± 667	$(187 \pm 17) \times 10^{-15}$
4000	10000	9498 ± 408	$(173 \pm 13) \times 10^{-15}$
6000	10000	8998 ± 725	$(184 \pm 19) \times 10^{-15}$

Table 5.1: High layer fitting for a two atmosphere model with a low resolved layer, and an unresolved layer at 10 km. Both layers have strength 193×10^{-15} $m^{1/3}$. It can be seen that the fit is much better for an unresolved layer, when the resolved layer is close to the ground (a common scenario), although potentially useful estimates can still be made in the case of higher resolved layers.

height of the SLODAR instrument. Based on SCIDAR profiling data from La Palma [80] it was clear we should anticipate significant turbulence above the maximum sensing altitude (approximately 7 km). The average profiles show a high layer at approximately 13.5 km, however these are statistical averages, and individual profiles are likely to exhibit more than one high altitude layer on occasion, so it is important to investigate how the algorithm behaves under those circumstances. A simulation was run with two layers one at 10 km, and the second at 15 km, both with a turbulence strength of 193×10^{-15} $m^{1/3}$. The fitting measured a turbulence strength of $383 \pm 8 \times 10^{-15}$ $m^{1/3}$ at an altitude of 11764 ± 664 m. This contrasts with the current uncorrected estimation which measures a turbulence strength of $322 \pm 5 \times 10^{-15}$ $m^{1/3}$ and no estimation of the turbulence height. With the phase and scintillation fit the correct turbulence strength was determined, and the measured altitude was between that of the two turbulent layers. Hence, even in such conditions, useful estimates can be made for parameters such as the isoplanatic angle (as in section 5.4.4).

5.4 On sky testing of this method

The work described above was based on the La Palma SLODAR pre–2011. Since then the telescope has been upgraded to a 50 cm model, matching that used for the SL-SLODAR at ESO Paranal. It is important that this method is tested in simulation for the larger telescope, as the subapertures are now 6.25 cm wide as opposed to 4.75 cm. There are two different regimes for scintillation variance as described by equations 2.39 and 3.14. The methodology remains the same and the method for generating the SIRFS has been shown to

be robust for different inner and outer scales, providing that those values are much smaller and much greater than the subapature size respectively.

5.4.1 Simulation results for 50 cm telescope

After the upgrade, the subapertures are significantly larger, 6.25 cm sides as opposed to 4.75 cm. This represents an increase in area of 1.73 times, and so the validity of the $\sigma_I^2 \propto h^{5/6}$ relationship must be checked. The use of the 4.75 cm subapertures appears to be at the limit of validity for equation 2.39 from simulation results shown in figure 5.8. Over the range of propagation distances shown, there is no more than 20% discrepancy for the 2 km propagation distance. For propagation distances of over 6 km, the discrepancy is only 7%, reducing for longer propagation distance. We conclude that for this configuration and high altitude profiling this approximation is valid. However the discrepancy appears to take the form of a characteristic h^2 dependence, requiring investigation of the 6.25 cm subapertures.

Using the Monte Carlo simulation, a series of measurements were made for the scintillation index for differing altitudes and turbulence strengths, and a fit was made to the altitude dependence. The scintillation indices are plotted against a theoretical curve using equation 2.39, and fitted to a $\sigma_I^2 \propto h^2$ curve as described in equation 3.14. We can see the scintillation indices for this aperture follow the squared dependence on height.

However the theoretical model for this large aperture scintillation index doesn't include a constant of proportionality, and is stated for a circular aperture. If we are to make use of this relationship to fit free altitude turbulence, it is necessary to determine a value for this constant of proportionality, in addition to the effect of a square aperture, which for a given size (either diameter or length of side) will have a collecting area 1.3 times greater than the system with 4.75 cm sub–apertures, and be able to measure spatial fluctuations up to a scale $\sqrt{2}$ times larger. We rewrite equation 3.14 to include a constant of proportionality C, and make the ansatz that the modification to account for a square wavefront sensor aperture instead of the circular aperture depends only on the aperture size D, represented by the arbitrary function $f(D)$,

$$\sigma_I^2 = f(D)C\left(\cos\gamma\right)^{-3}\int_0^\infty h^2 C_n^2\left(h\right)\mathrm{d}h. \tag{5.9}$$

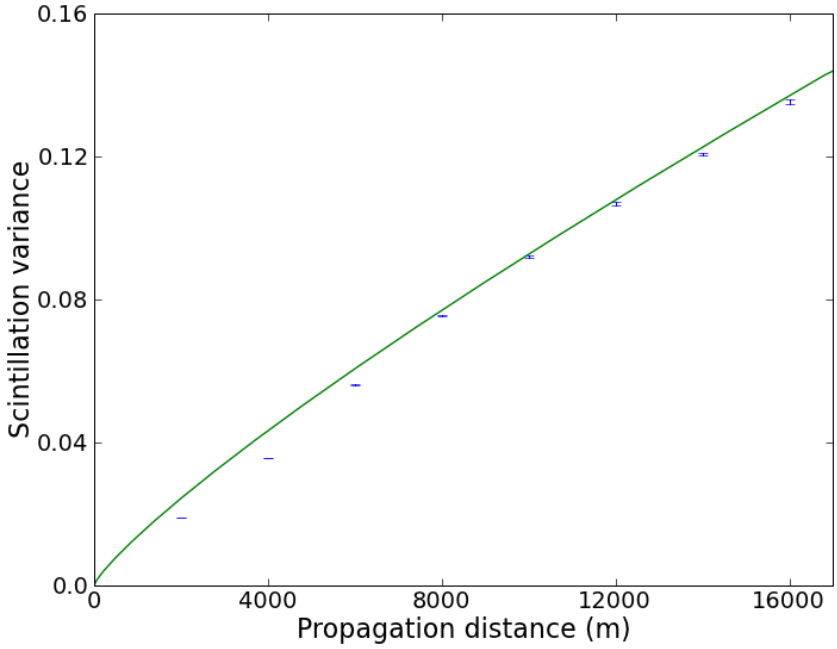

Figure 5.8: Plot showing theoretical and Monte Carlo simulation results for FA-SLODAR with subaperture diameter of 4.75 cm. The example shown has turbulence strength 100×10^{-15} $m^{1/3}$, at a wavelength of 500 nm. The solid line represents the theoretical variance from equation 2.39, and the dotted line that from Monte Carlo simulation. For propagation distances greater than 6 km they show good agreement, however for shorter distances the simulation shows a distinctive h^2 relationship.

In section 3.2 there is an extensive test of the behaviour of the Monte-Carlo simulation used throughout this work, and it is shown to be in good agreements with a range of theoretical tests, crucially those involving the phase aberrations, and Fresnel propagation, and that the h^2 dependence is valid for square apertures. Therefore using the simulation this free altitude fitting can be calibrated by 'measuring' the product $f(D)C$, not only for the constant of proportionality, but any differences owing to the differing aperture geometries. We measure this to be $4166\binom{+297}{-260}$, averaged across a number of independent Monte-Carlo simulations with turbulence strength between 50×10^{-15} $m^{1/3}$ and 450×10^{-15} $m^{1/3}$. An example is shown in figure 5.9 for turbulence strength 250×10^{-15} $m^{1/3}$, showing the strong h^2 dependence, and the effect of the measurement error of the constant. The agreement breaks down for propagation distances of greater than 12 km.

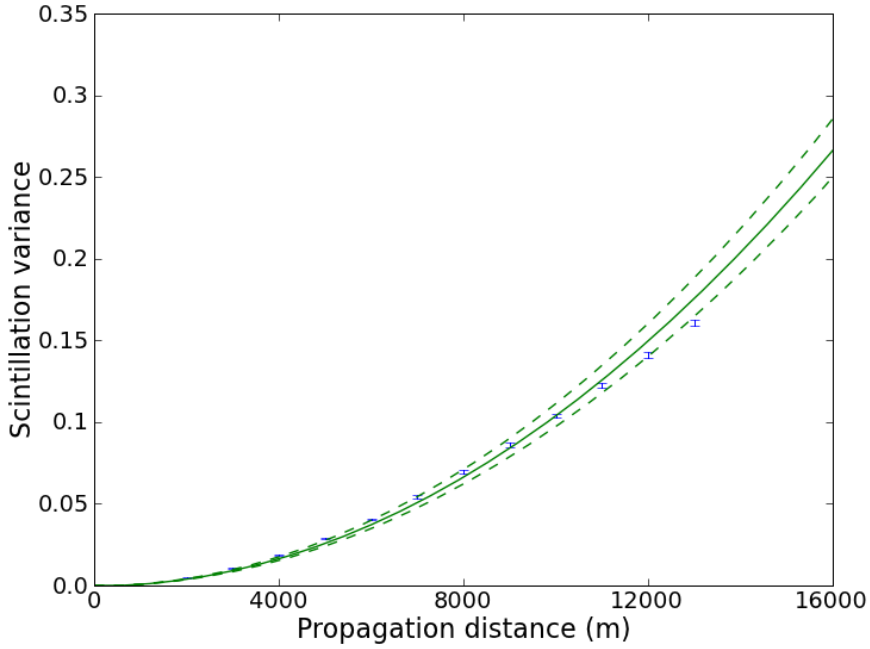

Figure 5.9: Plot showing theoretical and Monte Carlo simulation results for FA-SLODAR with subaperture diameter of 6.25 cm. The example shown has turbulence strength 250×10^{-15} $m^{1/3}$, at a wavelength of 500 nm. The solid line represents the theoretical variance, and the dotted line the errors on the theoretical variance from the measurement of $f(D)C$. Up to 12 km, the two are in agreement within error, however it can be seen that the simulated values do not exactly fit the h^2 power law, and the agreement breaks down beyond 12 km.

As the method is calibrated using the Monte-Carlo simulation, it would be inappropriate to attempt to verify this method using the simulation itself, so it must be tested on sky.

5.4.2 Comparison with MASS

In order to test the results produced by the full atmosphere SLODAR it is useful to have another turbulence profiler with which to compare. The SL-SLODAR at Paranal operates in conjunction with a MASS profiler. We extract a characteristic turbulence altitude from the MASS data to compare with SL-SLODAR used in FA-SLODAR mode.

Binning MASS data

As for SLODAR and SCIDAR, the MASS also has response functions, showing the instruments sensitivity to turbulence at a given altitude. For a given altitude in the profile, h_i, the response function is a triangle, centred on h_i, and going to zero at h_{i-1} and h_{i+1}. Typically MASS has bin centres at 0.5, 1, 2, 4, 8, and 16 km, so these response functions correspond to logarithmic bins. The response functions are plotted in figure 5.10.

We wish to compare the altitude produced from the full atmosphere SLODAR with a characteristic altitude from the MASS turbulence profile. The simplest method is to take a weighted centre of mass from the MASS, so the characteristic altitude of the MASS turbulence is

$$h_{\mathrm{MASS}} = \frac{\sum_i^h h_i C_n^2(h_i)}{\sum_i^h C_n^2(h_i)}. \tag{5.10}$$

This approach however has limitations. Firstly we are not taking into account the response functions shown earlier, the fact that they are non symmetric, and more importantly their width. Each bin has a width of $\frac{3}{2}h_i$, meaning that the 16 km bin contains signals covering a range of 24 km. The bins also overlap, so that a turbulent layer at 12 km will be measured in both the 8 and 16 km bins. This leads to a large uncertainty in the averaging, and a bias towards high altitudes.

Instead we use a centre of mass technique taking into account the shape of the response functions. First the MASS responses are scaled by the turbulence in the measured profile, and the linear sum of these responses is projected along the height axis. The centre of mass

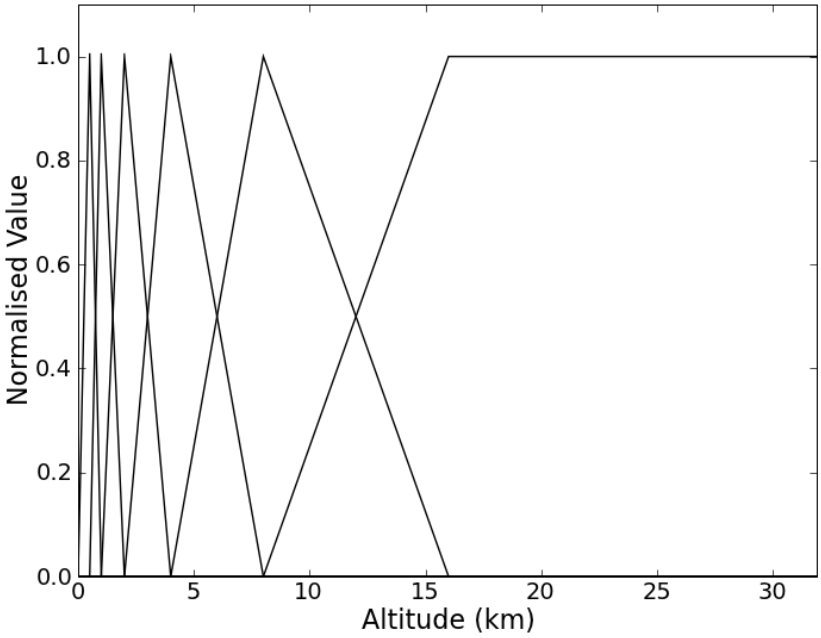

Figure 5.10: MASS response functions for a typical instrument. Each bin is centred at $h =$ 0.5, 1, 2, 4, 8, 16 km, with zeros at the centre of adjacent bins. The logarithmic altitude response, and the large overlap between bins can be clearly seen.

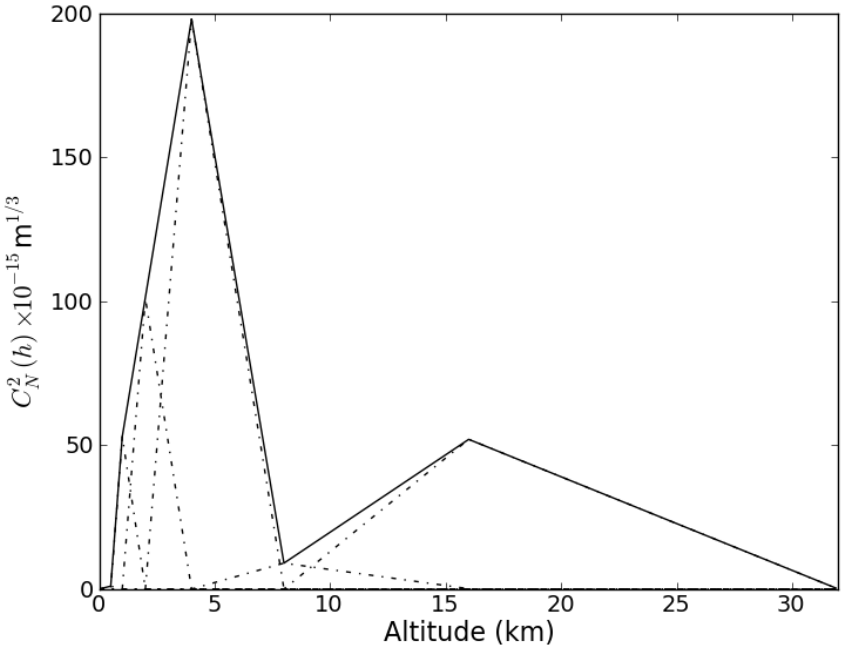

Figure 5.11: Mass profile for 1:00 UT, 18/03/2011 at Paranal Chile. The scaled MASS response functions are shown with dotted lines, and the sum of the responses along the height axis are shown. Using the simple centre of MASS technique the characteristic height would be 5 ± 2 km, and using the sum of the responses technique the altitude is 10 ± 3 km.

is then found for this distribution. An error on the altitude can then be found by calculating the standard error of the centre of mass measurement. The effect of this technique as opposed to a standard centre of mass is illustrated in figure 5.11, taking data from the Paranal MASS, at 1:00 UT on the 18/03/2011. The figure shows the responses scaled to the turbulence, and also the sum along the height axis. For this example, a standard weighted average of the MASS data gives a mean altitude of 5 ± 2 km. From the figure it can be seen that any contribution from the high layer is underestimated, owing to the closeness in altitude of the lower bins. By performing this calculation using the response function, the altitude retrieved is 10 ± 3 km, which is clearly more appropriate. However in the case shown, in addition to taking into account the higher altitude turbulence, the width of the 16 km bin may cause a bias towards a higher altitude.

The logarithmic nature of the bins mean that the MASS data could easily be biased

towards higher altitudes when using this analysis, and indeed the error on the characteristic altitude will be large, meaning care must be taken with any comparison to SLODAR.

This bias can be illustrated by considering a single layer of turbulence increasing in altitude. A single layer MASS profile is generated using the response functions, and is measured using the method outlined above. As seen in figure 5.12 this measurement is biassed, and the altitude of the turbulent layer is overestimated by 16%. Initially one would assume that as we are both generating and measuring the profile using response functions that the input and measured altitudes would be equal. However we assume no *a priori* knowledge or estimates of the turbulence profile when calculating an average height, and as the triangular bins are asymmetric, when the profile is retrieved the altitude of the single layer is biased towards the higher altitude. The altitude is overestimated by 17%.

Note that we use a different technique for interpreting the MASS data than that used by Lombardi [81]. He proposes rebinning the data using rectangles with edges at the crossing points of the triangular functions. This is unsuitable for our needs as it takes into account neither the shape of the response functions, nor the fact they overlap.

5.4.3 Description of the Surface Layer SLODAR at Paranal

The telescope itself is a 0.5 m modified Dall-Kirkham design, with a diffraction limited field of view of 18 arcminutes. The pupil images from each star are diverted using a reflecting prism along the two arms of the instrument into two Shack Hartmann wavefront sensors, each projecting 8×8 subapertures across the telescope pupil. The wavefront sensor cameras are Andor Luca S658M EMCCD devices. They have 658×496 pixels, of size 10 μm, with a peak quantum efficiency of 50% at 500 nm. The maximum EM gain is 200, resulting in a rms read noise of less than 0.1 electron [82]. The detector is 2×2 binned, giving an image scale of 1.225 arcseconds per binned pixel. Typically star separations of about 16' are used, giving 10 m altitude resolution up to a height of 80 m. This provides an excellent testbed for the method of fitting unsensed turbulence as, in addition to the comparison to MASS, this particular instrument has a large blind spot above its resolving range. The instrument is shown in figure 5.13.

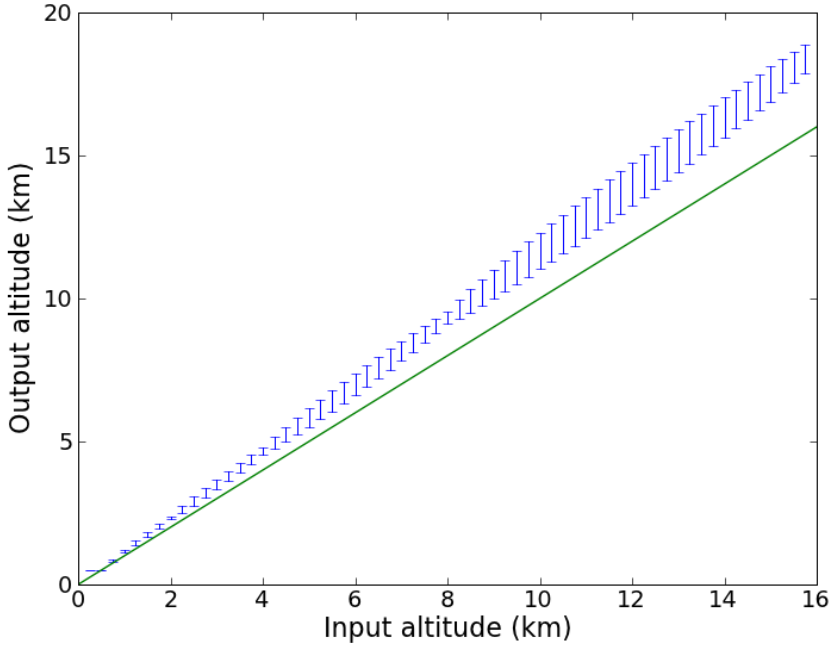

Figure 5.12: Illustration of bias when retrieving a single altitude from a MASS profile, with no *a priori* knowledge. The solid line has a gradient of 1, and the error bars are taken from the standard error on the mean. The retrieved altitude is overestimated by 17%.

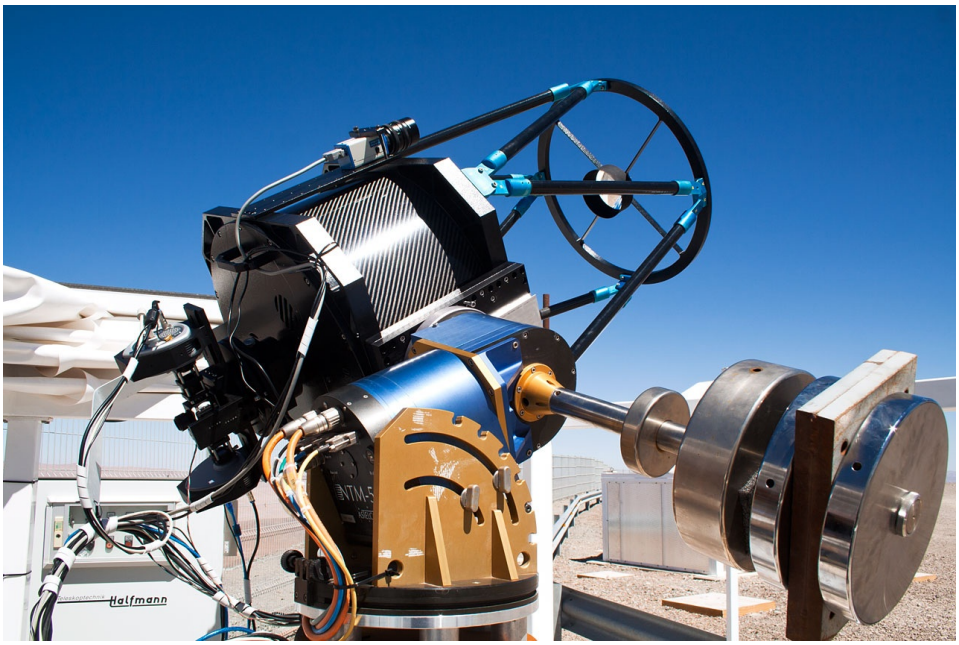

Figure 5.13: Photo of the SL-SLODAR instrument on the VLT platform at ESO Paranal. The telescope is a 0.5 m modified Dall-Kirkham. At the focus of the telescope is the mount holding the reflecting prism, and the two arms of the instruments holding the lenslet array and Luca cameras can be seen. (Photo credit; Tim Butterley (University of Durham) / ESO).

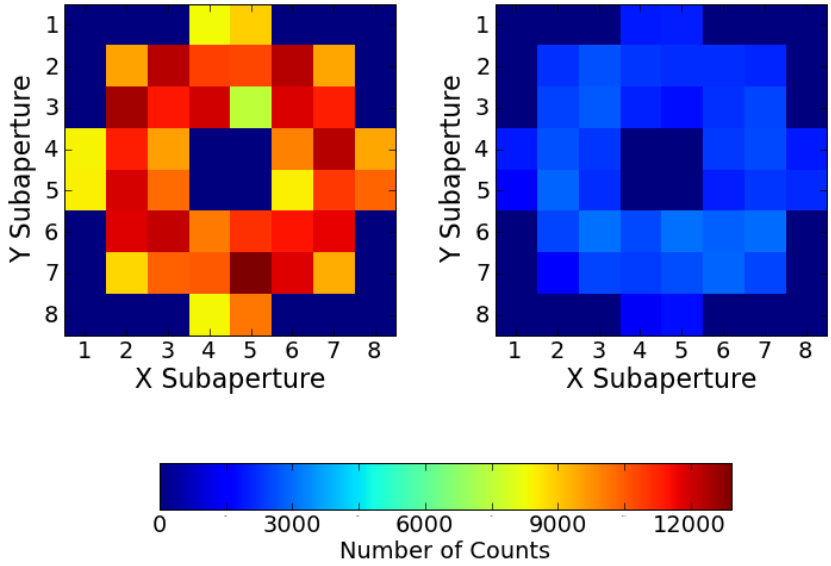

Figure 5.14: Map of average subaperture illumination for the SL-SLODAR with binary components of magnitudes 4.48 (left) and 5.74 (right). The data is averaged over 58 seconds. The effect of vingetting can be seen in the pairs of subapertures at the edge of both images, as well as those surrounding the central obscuration. Note the large difference in measured intensity between both images. The right hand image hints at a non uniform illumination for this particular target.

5.4.4 Comparison with MASS

The FA-SLODAR method when applied to the SL-SLODAR instrument has been calibrated for square subapertures of size 6.25 cm. When measuring the scintillation index, we must be careful to ensure that only fully illuminated subapertures are used. Figure 5.14 shows an average example illumination, averaged over 3000 frames of data. The reduction in flux caused by vingetted subapertures can be seen in rows and columns 1 and 8 in both images, and also for those surrounding the central obscuration.

For each frame of data, the 20 fully illuminated subapertures are chosen. The subapertures away from the edge of the pupil and the central obstruction are chosen to minimise any effect of non uniform illumination. The subapertures used to measure the scintillation index are shown in figure 5.15.

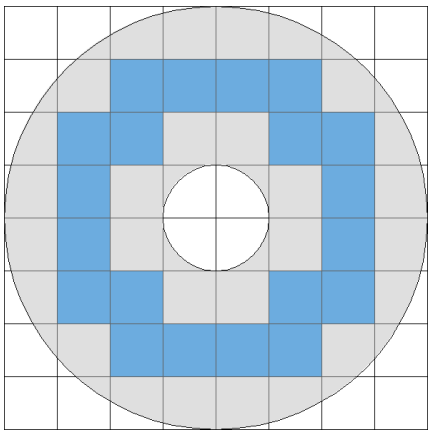

Figure 5.15: Illustration of the telescope aperture for SL-SLODAR projected onto an 8×8 wavefront sensor (grey annulus). The subapertures used to measure the scintillation index for the FA-SLODAR are highlighted in blue

The most obvious comparison is to simply plot the free atmosphere turbulence predicted by the SLODAR against that measured by the MASS. The current incarnation of the SL-SLODAR instrument has been observing at Paranal since March 2011. The following analysis considers data from this date up to February 2012 inclusive. In total 222 nights of data are considered in the analysis. This is shown in figure 5.16. The plot shows a significant correlation between the FA-SLODAR and MASS, however with a lot of scatter. The technique shows promise, but we need to understand the obvious bias at higher altitudes. Observing over the course of a night, the MASS and SLODAR observe different targets, and the SLODAR observes over a large variation of zenith angles. Whilst the SLODAR data is corrected for airmass as in equation 5.9, there may be a large projected separation when the SLODAR and MASS pupils are projected onto high altitude turbulence. For example if both instruments operate at a zenith angle of 22.5 degrees, orientated in opposite directions to each other, for a turbulent later at an altitude of 5 km the two projected pupils will be separated by 4.1 km, meaning different turbulent regions will be observed. Additionally, as the atmospheric turbulence is generated by a random process, there will be inherent scatter between the two measurements. This is discussed further in section 6.3.2.

The measured strengths for MASS and the SLODAR free atmosphere can also be compared, and these are shown in figure 5.17. The MASS value is taken from the integrated turbulence across all six of the MASS turbulence bins. Again there is general correlation,

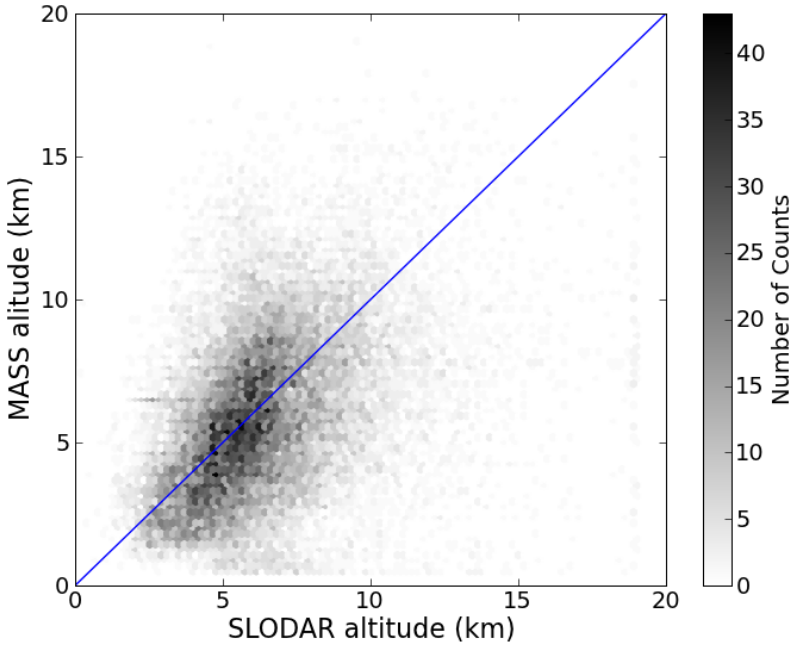

Figure 5.16: Free atmosphere height measured by FA-SLODAR plotted against height measured by MASS at Paranal, for 222 nights of data between March 2011 and February 2012. It can be seen the turbulence strength at Paranal is generally located at an altitude below 10 km, and there is significant correlation between the SLODAR and MASS. The straight line on the graph represents SLODAR = MASS.

but a large scatter in values.

The current implementation of SL-SLODAR at Paranal provides an estimate of the unsensed seeing by subtracting the integrated turbulence strength in the resolved profile from the whole atmosphere seeing measurement as measured from the auto-covaraince. However as discussed in 5.3.2 the effect of Fresnel propagation leads to centroid variance suppression, and an underestimate of the total turbulence strength. We therefore expect by fitting using the Fresnel corrected response functions to measure a greater unresolved turbulence than with the simple difference method.

The average altitude of free atmosphere turbulence measured by the SLODAR over all the data taken from Paranal is 6 ± 2 km, and from this it is possible to predict a factor by which we expect the SLODAR to currently underestimate the turbulence. This factor can be calculated from the ratio of the peaks in the current and scintillation corrected

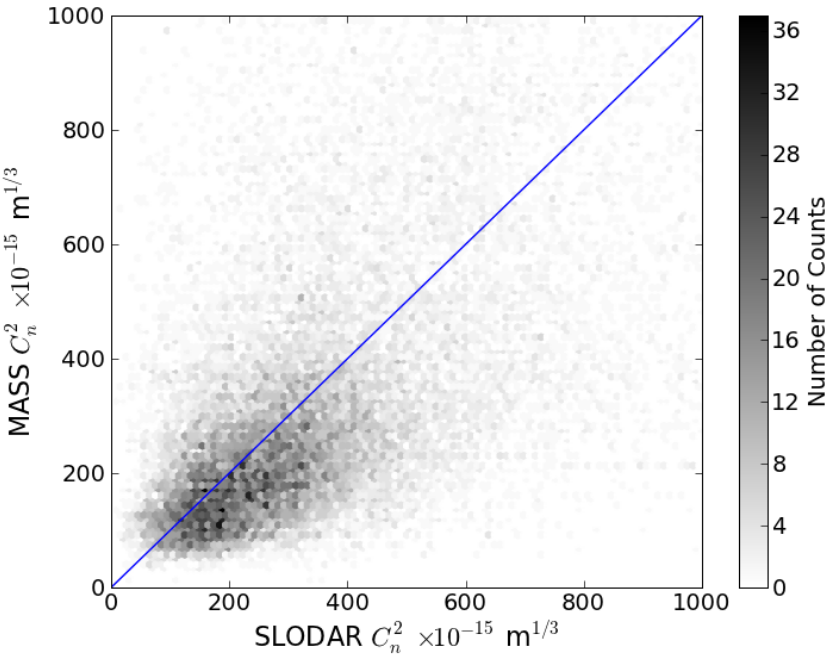

Figure 5.17: Free atmosphere turbulence strength measured by FA-SLODAR plotted against the integrated strength measured by MASS at Paranal, for 222 nights of data between March 2011 and February 2012. The straight line on the graph represents SLODAR = MASS.

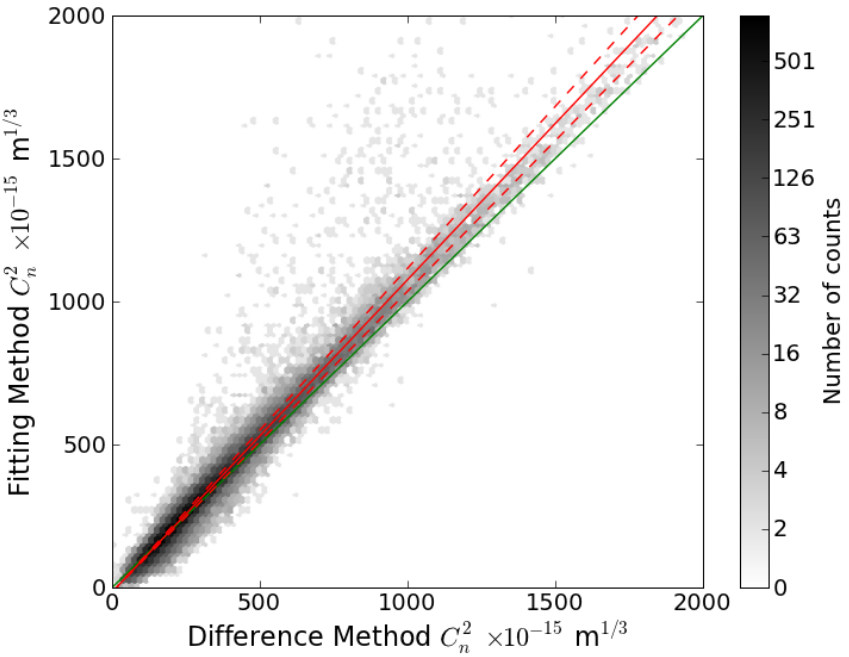

Figure 5.18: Free atmosphere turbulence strength measured by FA-SLODAR (fitted method) against the prediction made by the current SL-SLODAR (difference method). The green line has a gradient of 1, the red line the least squares fit to the data, and the dotted lines the error on this fit. The underestimation of turbulence strength for the difference method can clearly be seen. Note also the logarithmic binning, this has been chosen so the data for stronger turbulence, and the scatter at weaker turbulence can clearly be seen. In a small number of cases the fitting significantly overestimates the value for the turbulence strength.

autocovariance response functions. Currently, on average we expect the SL-SLODAR free atmosphere strength measurement to be (91±4)% of the true turbulence strength. This value will vary for altitude of turbulence, the strength estimate for lower atmosphere turbulence will be more accurate. The two values for turbulence strength (fitted and difference) for each datum are plotted over the full data sets in figure 5.18, and by performing a least squares fit we determine that currently the seeing is underestimated by $(92 \pm 1)\%$, showing that the free atmosphere fit performs in line with the theoretical predictions.

Section 2.1.2 introduces the *isoplanatic angle*, an important concept in adaptive optics. With an instrument that measures the altitude and strength of high altitude turbulence, it is easy to make a prediction for the value of the isoplanatic angle using equation 2.10. There have been previous studies of the isoplanatic angle at Paranal, for example with scintillation

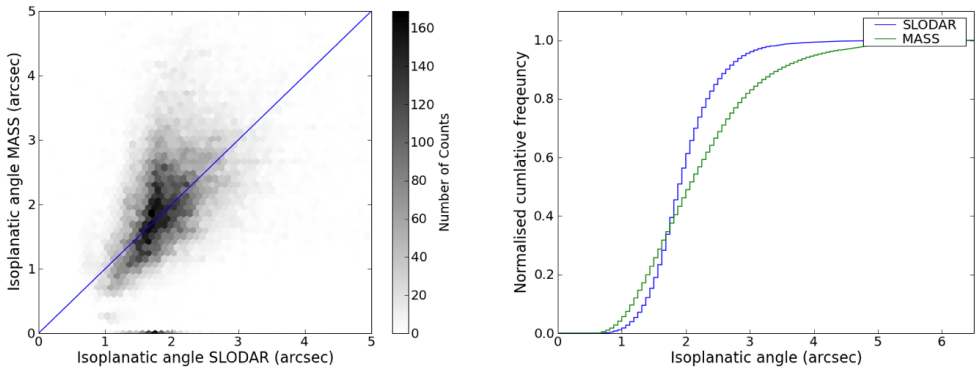

Figure 5.19: Scatter plot (left), and cumulative frequency histogram (right) showing the estimates for isoplanatic angle made by SL-SLODAR and MASS at Paranal. Below the point where MASS measures a ~ 2.5 arsecond isoplanatic angle, the two instruments are in reasonable agreement, however above this the MASS tends to measure a greater isoplanatic angle than SL-SLODAR.

	SLODAR (arcseconds)	MASS (arcseconds)
1^{st} quartile	1.64	1.55
median	1.93	2.06
3^{rd} quartile	2.27	2.63
interquartile range	0.63	1.08

Table 5.2: Upper and Lower quartiles and median isoplanatic angles measured by SL-SLODAR and MASS. The lower quartile and median values show a reasonable agreement, however the significant differences in the upper quartile and interquartile range show increased discrepancy for larger isoplanatic angles.

measurements from DIMM [83], and G-SCIDAR [84]. In addition the MASS-DIMM also provides a measurement for the isoplanatic angle, and we compare our measurement to this. Figure 5.19 shows both a scatter plot of the isoplanatic angle estimated by SLODAR and MASS, and a cumulative frequency histogram showing the distributions of the isoplanatic angle for the two instruments. For smaller isoplanatic angles the two instruments are shown to be in reasonable agreement, although when the angle is larger the SLODAR is 'reluctant' to measure these values. The FA-SLODAR does however sometimes measure large isoplanatic angles, as we can see from the figure there are SLODAR estimates of 5 arcseconds. Considering the cumulative frequency histogram, we see a marked difference in the distribution of estimated values for the isoplanatic angle from the two instruments. The median and quartiles for this distribution are shown in table 5.2.

Looking at the comparison of isoplanatic angles, one might initially conclude that the scintillation variance in the SL-SLODAR apertures may be saturating, as observed by the FA-SLODAR tending not to fit high altitudes as shown in figure 5.16. The distribution of scintillation variance used in the above fits was determined and illustrated in figure 5.20. The distribution of the variance measurements is continuous, suggesting no saturation of scintillation. If this were the case, one would expect a sharp drop to zero in the high scintillation end of the distribution. Large values for the isoplanatic angle will tend to occur for either very weak high layer turbulence, or for profiles dominated by turbulence in the lower atmosphere. From figure 5.16 we see for low altitude turbulence SLODAR measures systematically higher altitudes than MASS, having the effect of biasing the values for SLODARs measurement of isoplanatic angle to be smaller than that of MASS. Figure 5.20 shows SLODAR measures very little scintillation variance below 0.05, and possibly this lack of low variance signals in our subapertures introduces the bias to smaller isoplanatic angle.

5.5 Conclusions

A method for calculating SLODAR Impulse Response Functions taking into account the effects of Fresnel propagation has been developed using a semi-analytical method. These have been shown to match the expected shapes and amplitudes predicted from Monte Carlo simulations of the turbulent atmosphere and SLODAR, and the improvements to fitting atmospheric turbulence have been demonstrated. Moreover the numerical part of the method has been demonstrated to be robust over a wide range of integration limits (of the spatial frequencies), corresponding to measured values of the inner and outer scales of turbulence from a variety of observing sites. These measured values range over an order of magnitude for the outer scale, and two orders of magnitude on the inner scale.

A technique to utilise all information from the Shack Hartmann sensor has been presented to extend the utility of SLODAR beyond its direct sensing altitude, by simultaneously fitting residual autocovariance and residual scintillation variance to the unsensed turbulence. This method has been verified using simulation for the SLODAR at the WHT, and shown to

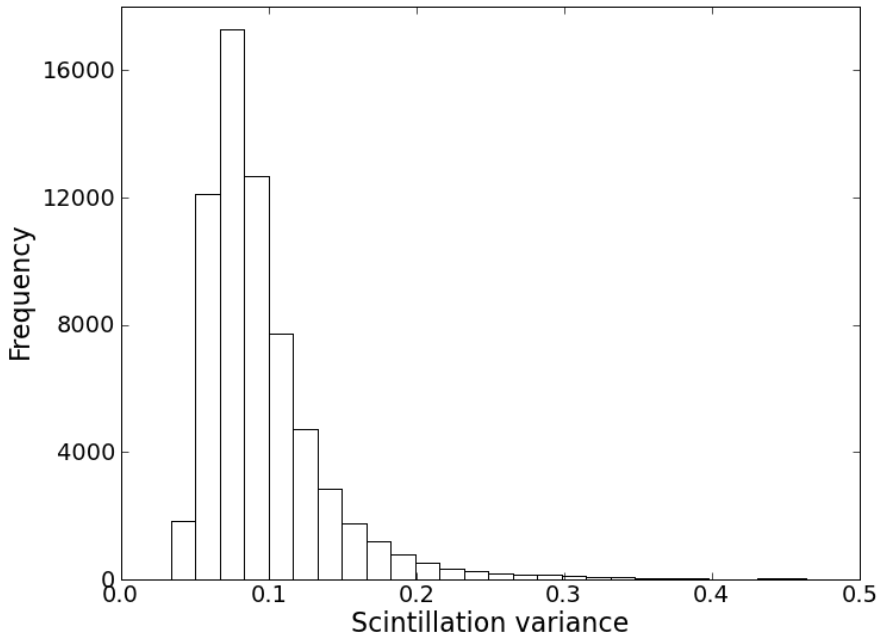

Figure 5.20: Distribution of scintillation variance as measured by the FA-SLODAR subapertures. The continuous distribution implies that the scintillation variance measurement does not saturate.

provide accurate estimations for turbulence altitude and strength in the typical case of one ground and one free atmosphere layer.

However the SLODAR system has since been upgraded, and the larger subapertures mean that the instrument is now in a regime where there is no exact analytical expression for scintillation variance. The Monte Carlo simulation was instead used to calibrate the instrument, after testing described in section 3.2.

This technique was applied to the SL-SLODAR at Paranal, where the data produced could be compared with MASS, and has been demonstrated to be a reliable method to retrieve information about turbulence in the upper atmosphere. This allows the SL-SLODAR to become an 'all in one' instrument for predicting AO performance: the high surface layer resolution allows detailed investigation of the performance of ground layer adaptive optics; the free atmosphere information predicts the isoplanatic angle for conventional AO.

Chapter 6

Practical SLODAR

6.1 Introduction

In this chapter we present data from SLODAR systems at two observatories, the surface layer SLODAR at Paranal, and a system on the roof of the WHT on La Palma. Results from the La Palma observing campaign are presented with data from 50 nights between September 2011 and April 2012. The SLODAR seeing measurements are compared with concurrent measurements provided by the ING DIMM, and the results are compared with data from the ING weather station.

We then discuss practical concerns with the implementation of SLODAR instruments. (i) SLODAR has appeared to measure non Kolmogorov turbulence in the surface and ground layers, and in this chapter we show that this is indistinguishable from inadequate sampling caused by low wind speeds. (ii) Due to the random nature of atmospheric turbulence and limited sampling there is a limiting uncertainty to which turbulence strength can be measured. (iii) Inadequate temporal sampling can lead to SLODAR being unable to measure velocities and directions of fast moving turbulent layers, however the strengths of such layers can be determined. (iv) Dome and tube seeing has been shown to be present in SLODAR systems, and the solution of applying a temporal filter to the data is discussed, along with other mitigation strategies. (v) A SL-SLODAR specific concern is addressed regarding the rotational offset of the two CCD detectors.

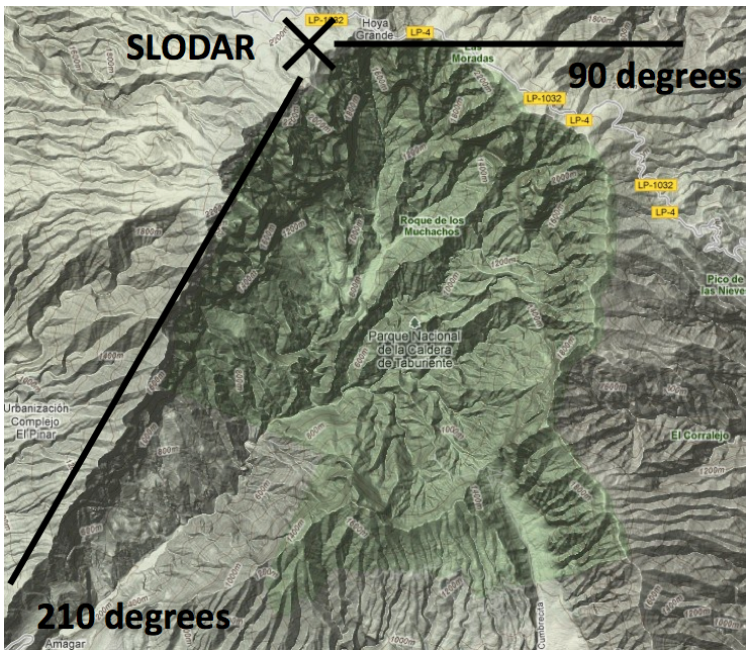

Figure 6.1: Map showing the location of the SLODAR instrument on the top corner of the Caldera de Taburiente. The directions 90, and 210 degrees have been marked on, and it is clear that they run along the top and left edges of the caldera respectively. (Map of Caldera de Taburiente, La Palma, Spain, retrieved on Feb 2, 2012 from website http://maps.google.co.uk/).

Finally using case studies of Paranal and La Palma, from SLODAR data the implications of weather conditions and local topography on atmospheric turbulence are discussed.

6.2 The La Palma SLODAR

The SLODAR system on La Palma was designed to provide turbulence profiles to support the observing runs for the CANARY MOAO demonstrator on the WHT. The La Palma SLODAR has had two incarnations, the first being the SALT SLODAR, and the second a specific instrument 'pt5m', a multi purpose instrument to perform turbulence profiling and transient astronomy, operated by the Universities of Durham and Sheffield.

6.2.1 Description of the instrument

The current incarnation of the FA-SLODAR is located on the roof of the WHT, as a part of the 'pt5m' project, which is a dual use turbulence profiler and transient astronomy instrument. The telescope itself is a 0.5 m modified Dall-Kirkham design with a diffraction limited field of view of 18 arcminutes. An Andor iXon EMCCD device is used as the wavefront sensor camera. In its typical mode of operation, binary pairs of between 9 and 14 arcseconds width are used, allowing a maximum sensing altitude of between 7 and 11.5 km depending on target elevation.

The telescope is equatorially mounted, to remove the need to de-rotate the images. We use an Andor iXon DV885LC EMCCD camera. It has 1004×1002 pixels, of size 8 μm, with a peak quantum efficiency of 65% at 600 nm. The maximum EM gain is 1000, resulting in an effective rms read noise of less than 0.1 electron [85]. The system is controlled by two Linux workstations, used for data acquisition and reduction, and telescope control. The FA-SLODAR wavefront sensor consists of a collimating lens and lenslet array directly attached to the camera. The lenslet array is optically conjugate to the telescope pupil and provides a 8×8 subaperture WFS. The CCD detector is 2×2 binned, with an image scale of 0.85 arcseconds per binned pixel.

6.2.2 Profiling Campaign

A La Palma SLODAR profiling campaign ran between September 2011 and April 2012, taking data for 50 nights in that period. For these nights there were also concurrent measurements with the ING DIMM, providing an independent measure for the integrated seeing.

6.2.3 Comparison with DIMM

As the ING DIMM can provide an independent measurement of the seeing angle, it is useful to compare the measurements from SLODAR with that of the DIMM.

As with the FA-SLODAR, the simplest form of comparison is to plot the seeing as measured by the SLODAR against that measured by DIMM. This is shown in figure 6.3. We see good agreement up to a strength (measured by DIMM) of 1.5 arcseconds, and beyond

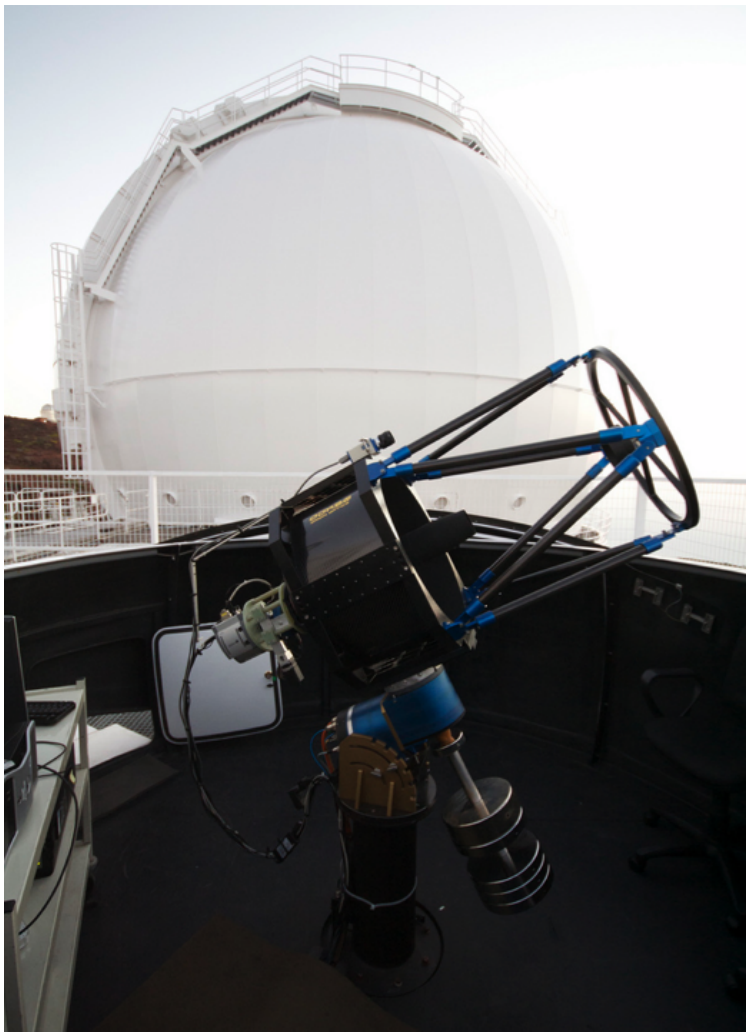

Figure 6.2: Photo of the pt5m instrument in front of the WHT dome. The telescope is a 0.5 m modified Dall-Kirkham. At the focus of the telescope the Andor iXon wavefront camera can be seen at the furthest left point, and on the inside of that the slider to move the fast photometry camera in place. To the left of the image just in frame are the Linux PC's used for data acquisition and reduction, and telescope control. (Photo credit; Vik Dhillon (University of Sheffield))

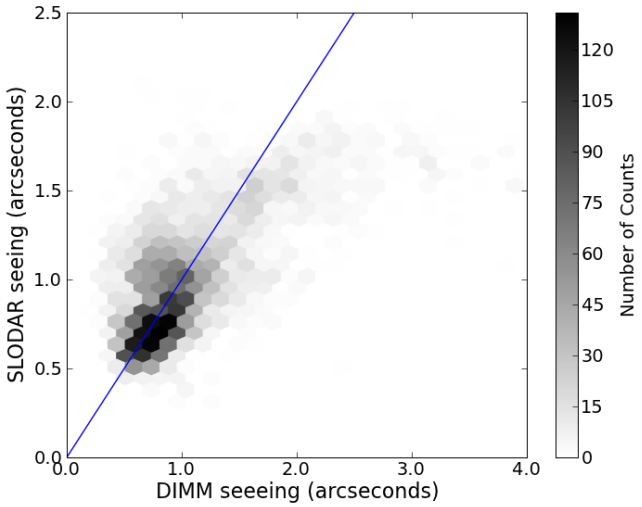

Figure 6.3: The WHT SLODAR v DIMM seeing. It can be seen that the two measurements are in good agreement to a turbulence strength of 2 arcseconds. Beyond this, the DIMM measures higher seeing, and the SLODAR appears to asymptote. This discrepancy occurs for less than 6% of the total number of measurements. The straight line indicates SLODAR = DIMM.

this the SLODAR measurement asymptotes. From the figure, one can also see that only a small fraction of the results occur in this divergent regime, and we measure this to be 6% of all measurements. There are several hypotheses to explain this discrepancy; (i) there is a sampling issue, possibly due to low wind speeds, (ii) the SLODAR seeing measurements are saturating, (iii) this is a real difference in the seeing angle measured at the two locations.

(i) Firstly the effect of wind speed on these discrepancies will be addressed. For safety reasons the SLODAR only operates when the wind speed is less than 12 ms^{-1}. The SLODAR-DIMM pairs are divided into categories corresponding to low ($v < 3$ ms^{-1}), medium (3 $\mathrm{ms}^{-1} \leq v < 9$ ms^{-1}) and high ($v \geq 9$ ms^{-1}) wind speeds. The SLODAR and DIMM seeing measurements are replotted in figure 6.4 including the wind speed. There is a homogenous distribution of wind speed in both the regions where the two measurements agree, and the region where they diverge, so we may conclude there is no wind speed effect on this disagreement between the two values. However one interesting result is the amount of scatter between the SLODAR and DIMM measurements is reduced for higher wind speeds. In conditions where the power spectrum of the measured turbulence is non Kolmogorov, or

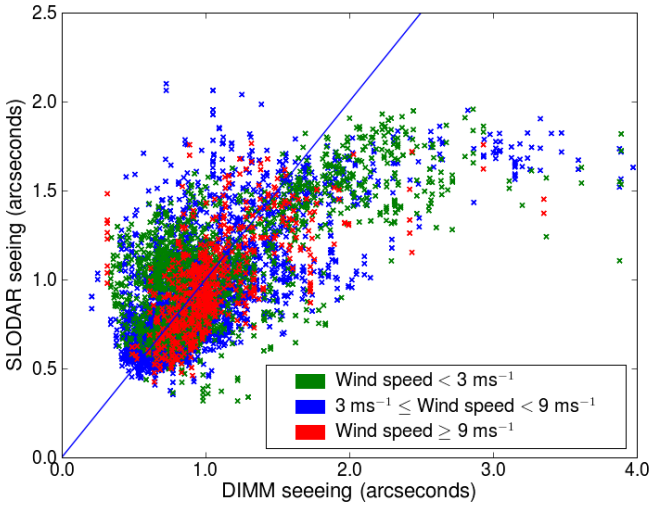

Figure 6.4: WHT SLODAR v DIMM seeing, showing low ($v < 3$ ms^{-1}), medium (3 ms^{-1} $\leq v < 9$ ms^{-1}) and high ($v \geq 9$ ms^{-1}) wind speeds. There is no wind speed dependency on the discrepancy between SLODAR and DIMM. The straight line indicates SLODAR = DIMM.

appears to be non Kolmogorov (section 6.3.1) the SLODAR will measure less turbulence, and the DIMM will measure more.

(ii) Now consider the effect of wind direction on this discrepancy between the two measurements. First the average seeing for each wind angle is plotted for both DIMM and SLODAR in figure 6.5. From this graph, there are two clear results. For a wind direction between SSW (205°) and East (90°) the SLODAR and DIMM are in excellent agreement, and they diverge when the wind is between East and SSW. This latter regime occurs in conditions of worse seeing. Referring to figure 6.1 these directions can clearly be seen to correspond to the edge of the Caldera de Taburiente, and the worse seeing conditions and high discrepancy occur when the prevailing wind blows through this caldera. With this in mind, another version of the scatter plot is shown in figure 6.6, identifying the wind directions (from the Caldera and from all other directions). Again it is clear that for 'weak' seeing the wind direction has no effect on the agreement, it only occurs in strong seeing conditions when the wind is blowing from the caldera. This can be seen more clearly in figure 6.7, where the turbulence for the mean first profile bin, and the integrated turbulence for the rest of the atmosphere can be seen. We see that the vast majority of the turbulence strength

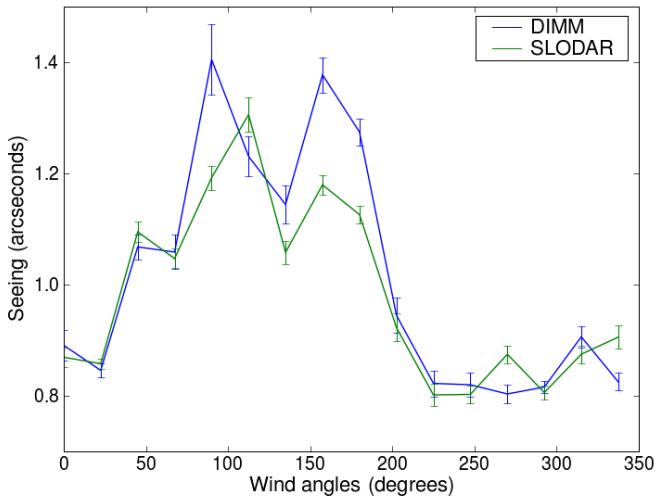

Figure 6.5: The average WHT SLODAR and DIMM seeing for each given wind direction as measured by the ING weather station. The SLODAR and DIMM measurements are shown to have excellent agreement, apart from the region between 90° and 205°. This region of discrepancy also has a worse average seeing.

occurs within 500 m of the ground, and so the discrepancy between DIMM and SLODAR occurs in this region, implying effects of local geography. We see also that turbulent structure in the higher atmosphere tends to occur when the wind direction is between 90° and 270°, although the ground layer turbulence dominates the free atmosphere turbulence.

(iii) At the start of this section it was suggested that the SLODAR seeing measurement may be saturating. When seeing is described as saturating, this implies that the measurement reaches an asymptotic value despite the strength of the actual turbulence. For any turbulence strength one would expect the distribution of wavefront slopes (and hence the centroids) measured by a Shack Hartmann sensor to obey a Gaussian distribution [65]. The assumption is made therefore, that if the seeing measurement saturates, the SLODAR will no longer measure a Gaussian distribution of wavefront slopes. Taking only the SLODAR measurements from when the wind is blowing from the caldera, we fit a Gaussian function to each individual distribution of wavefront slopes. Before performing the fit, each distribution of centroids is binned into 20 bins, and the sum of the histogram is scaled so the sum of all bins is one. This enables direct comparisons to be made despite the turbulence strength. If

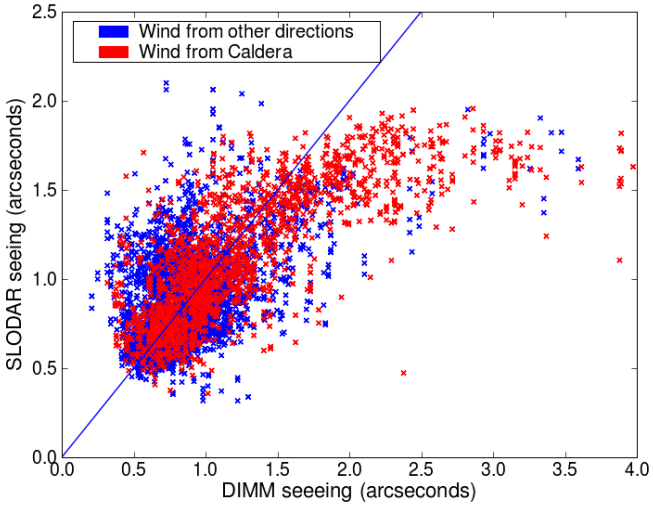

Figure 6.6: WHT SLODAR v DIMM seeing, indicating the results as the wind blows from the caldera, and from all other directions. The large discrepancies are almost wholly when the prevailing conditions come through the caldera, and only for bad seeing as measured by DIMM. For weaker seeing the wind direction appears to have little effect on the measurements.

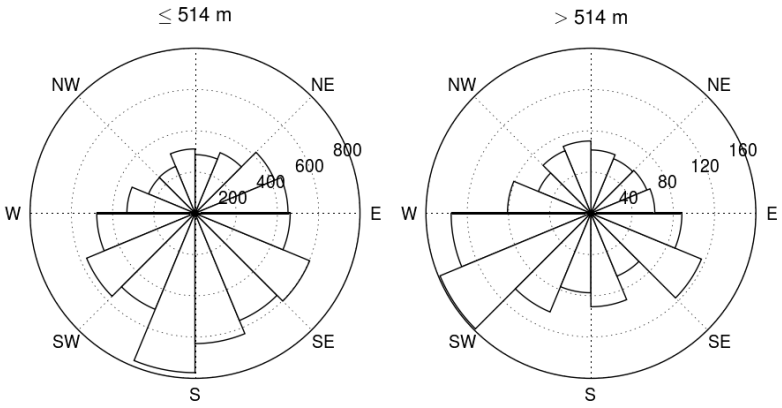

Figure 6.7: The effects of wind direction on the turbulence profile at the ORM, showing the integrated turbulence below 514 m (left), and above 514 m (right). The azimuthal axis indicates from which direction the wind blows, and the radial axis the integrated turbulence strength in units of $\times 10^{-15}$ $m^{1/3}$. Note the change in scale between the two plots. The vast majority of turbulence strength occurs in the ground layer, and it is this turbulence that will cause discrepancy between SLODAR and DIMM. The free atmosphere turbulence also tends to be stronger when the wind is from between 90° and 270°.

seeing does saturate we would expect a much worse fit for high seeing angles. To provide a parameter of goodness of fit, Pearson's χ^2 statistic is calculated for each fit. Across a series of n data points, the value for χ^2 is given by

$$\chi^2 = \sum_{i=0}^{n} \frac{(D_i - f_i)^2}{f_i} \tag{6.1}$$

where D_i is the measured data value, and f_i is the value for the fit at point i. The χ^2 values corresponding to each fit are recorded, and then plotted against seeing angle. If the seeing saturates there would then therefore be a higher value for larger seeing angle. These results are shown in figure 6.8, and the median Pearson's χ^2 statistic is fairly homogenous over all seeing angles. However this plot only compares the fits with each other, and gives no clear picture of how Gaussian these distributions are. Figure 6.9 shows an example of the Gaussian fit to centroid distribution for arbitrary examples of the lower quartile ($\chi^2_{\mathrm{LQ}} = 0.004$), median ($\chi^2_{\mathrm{Med}} = 0.009$), and upper quartile ($\chi^2_{\mathrm{UQ}} = 0.022$) values of the total distribution of χ^2 values. These results are shown in figure 6.9, and we see the Gaussian distribution provides a good fit to the centroid distribution in all cases. The conclusion therefore is that this discrepancy due to the differing wind directions is a real effect, and this allows speculation to be made on likely causes, and a proposal for an experiment to investigate this.

6.2.4 Turbulence profiles

As the SLODAR is the only turbulence profiler currently at the ING, the profiles can be presented, however no meaningful comparison can be made as the DIMM only measures integrated turbulence strength. An average profile is shown in figure 6.10. The average ground layer shows an exponential distribution of turbulence, with a scale height of 760 m.

A previous long term SCIDAR campaign was run by García–Lorenzo and Fuensalida taking 211 nights of data between February 2004 and August 2009, on the 1 metre Jacobus Kapteyn telescope (JKT) [86]. They present median turbulence profiles, showing a dominant ground layer of turbulence, contained within the first kilometre of the atmosphere. The SCIDAR operated in a high resolution mode (summer), and low resolution mode (winter).

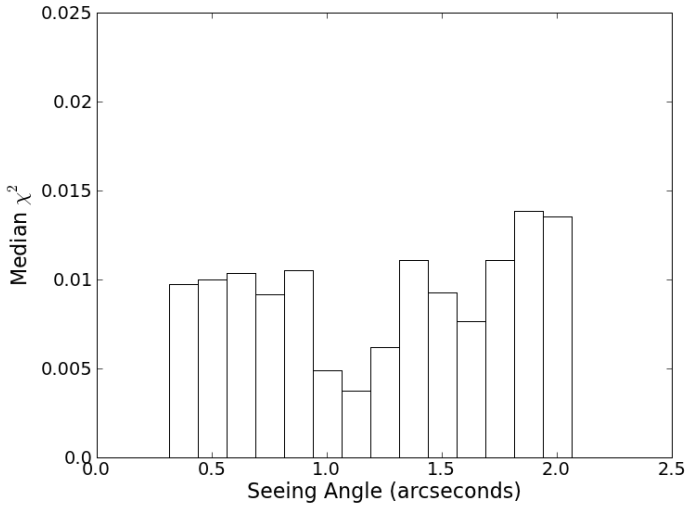

Figure 6.8: Pearson's χ^2 for the Gaussian distribution of wavefront slopes measured by the La Palma SLODAR as a function of seeing angle. The quality of the Gaussian fit is similar across all seeing angles, excepting a better fit between 1.0 and 1.3 arseconds.

The winter observations showed a very weak layer between 3 and 10 km in altitude, with strength 2.5% of the ground layer. The summer observations show a stronger turbulent layer at these altitudes.

After a technical upgrade the La Palma SLODAR ran for three nights in August 2012 (i.e. in the summer, as opposed to the previous campaign which was mainly in winter) to provide support for a CANARY observational run, and this free atmosphere layer was observed. Hence for the data taken we can broadly agree with the results of García–Lorenzo and Fuensalida.

6.3 Real world effects on a SLODAR instrument

6.3.1 Beta

In the generation of SLODAR impulse response functions we make the assumption that the atmospheric turbulence obeys a Kolmogorov power law. Recall that the Kolmogorov spatial spectrum has the form

$$\Phi_\phi(\kappa) \propto \kappa^{-\beta} {r_0}^{-5/3} \qquad (\beta = 11/3) \tag{6.2}$$

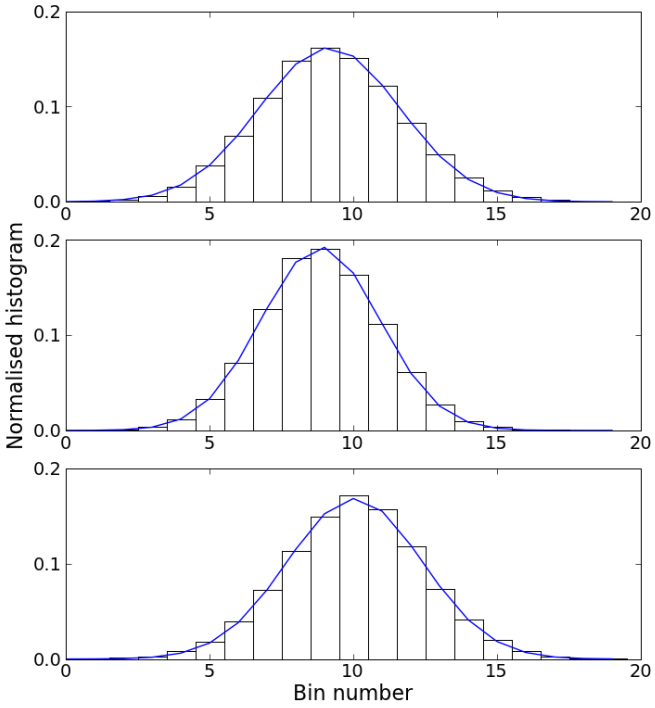

Figure 6.9: Three examples of the fitting of Gaussian distribution to wavefront slopes measured by the La Palma SLODAR. We show the fitting (line), and data (bar) for arbitrary examples corresponding to the Lower Quartile (top), median (middle), and upper quartile of the distribution of all measured χ^2 values.

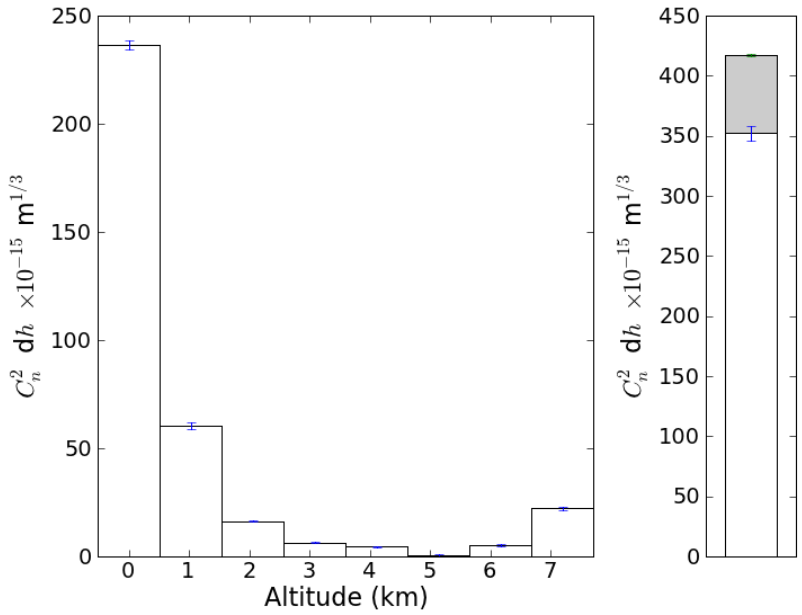

Figure 6.10: Average profile from the La Palma SLODAR for 50 nights of data between September 2011 and April 2012. The left hand plot shows the resolved turbulence profile, with a large amount of turbulence in the ground layer, and very little in the resolved portion of the free atmosphere. The right hand plot shows the integrated average profile, with integrated resolved turbulence in white, and the unresolved turbulence in grey. The ground layer ($<$ 4 km) fits a exponential distribution with a scale height of 760 m.

and for high altitude turbulence this appears to be a valid assumption to make. However for the surface layer $\beta < \frac{11}{3}$ is often measured. We can hypothesise three explanations for this effect

- *Time averaging* In low wind speeds the larger spatial scales (lower spatial frequencies) are not properly sampled. In such conditions the SLODAR appears to see an excess of high spatial frequencies, resulting in a measured $\beta < \frac{11}{3}$.
- *Dome turbulence* The dome and telescope causes turbulent effects which do not obey Kolmogorov statistics.
- *Atmospheric turbulence* The surface layer turbulence often has a non Kolmogorov power law.

Before discussing these items, we look at the effects of this smaller power spectrum coefficient on the SLODAR data reduction.

Figure 6.11 shows SLODAR impulse response functions for a ground layer of Kolmogorov and non-Kolmgorov turbulence, and the effect of fitting Kolmogorov SIRFS to non Kolmogorv turbulence. The peak for the non Kolmogorov turbulence can clearly be seen to be sharper, and also less negative at the extremes. From the figure, the effect of fitting Kolmogorov response functions to the non Kolmogorov turbulence can be observed, and it manifests as distinctive negative 'side lobes' in the profile.

There have been studies suggesting that non Kolmorogov turbulence appears in the Surface Layer [87], however analysis of SLODAR data suggests there are other factors that may lead to false readings of non Kolmogorov turbulence. Figure 6.12 plots wind speed against average measured β values for both the La Palma SLODAR and the Paranal SL-SLODAR. We see for low wind speeds the measured β value is much lower than for high wind speeds in both cases. However note the y axis scaling in both cases, with the La Palma SLODAR measuring a lower average value for β than the Paranal system.

Considering the Paranal system, where the measured turbulence tends towards Kolmogorov for wind speeds above 4 ms^{-1}, we have the opportunity to compare the trend against simulation. In figure 6.13 the simulation results are plotted against the SL-SLODAR data and we see that the real instrument measures slightly lower values for β for all wind

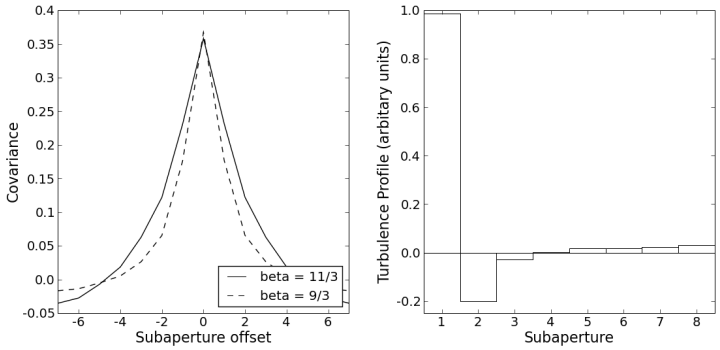

Figure 6.11: Figure showing Kolmogorov and $\beta = 9/3$ SLODAR response functions for a ground layer of turbulence (left), and the effect of fitting a Kolmogorov response to a single layer of non-Kolmogorov atmospheric turbulence (right). The difference in shape between the two response functions can clearly be seen. When a Kolmogorov response is fitted to non-Kolmogorov turbulence, distinctive negative 'sidelobes' can be seen in the profile. (We fit to $\beta = 9/3$ turbulence in this case.)

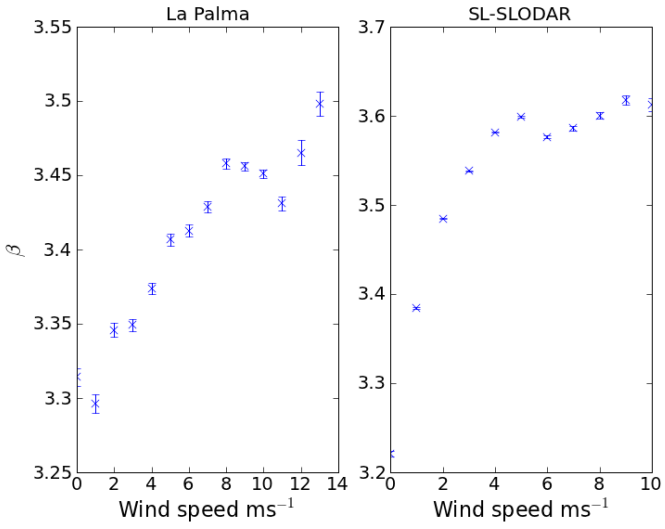

Figure 6.12: Effect of wind speed on the measured value for β, using the La Palma SLODAR (left), and the Paranal SL-SLODAR (right). We see that for low wind speeds the measured β is much lower, and the La Palma SLODAR tends to measure lower values for β than the Paranal system.

speeds. However the shape of both curves match, suggesting that for an instrument using the parameters of the SL-SLODAR we can say with some confidence that a wind speed of 4 ms^{-1} ensures sufficient averaging to measure the power spectrum of the turbulence.

This effect of low wind speed is not confined to SLODAR, and will have implications for other turbulence profiling instruments, as there are practical reasons making it difficult to fully sample low spatial frequencies at lower wind speed. To fully sample the turbulence at low windspeeds requires data to be taken over a long period of time (many minutes), whilst simultaneously making measurements at a high frequency so the small spatial frequencies can be sampled. This can lead to an impractical volume of data for existing systems. Additionally the requirements for such profilers is often to produce a profile per minute, which gives an insufficient sampling time. Using existing instruments such as DIMM and SLODAR we can not distinguish between this process and measuring a true non Kolmogorov power spectrum of turbulence. It is known that in apparent non Kolmogorov turbulence the DIMM will over estimate the integrated turbulence strength. Berdja concludes from DIMM data that non Kolmogorov turbulence does exist [87], however with no consideration of wind speed. In the light of the results from on sky SLODAR data at both Paranal and La Palma, combined with the Monte-Carlo simulations of wind speed, this is a significant omission. This 'apparent' non Kolmogorov turbulence owing to low wind speed will be seen by the DIMM also, meaning that the conclusion of Berdja can't be made with full confidence.

6.3.2 Convergence of Measurements

As we sample independent realisations of atmospheric turbulence for a finite amount of time there will be inherent uncertainties in the measurement of turbulence strength made. We show this using a simulation choosing parameters for the La Palma SLODAR, in which measurements are made of two independent atmospheres of the same strength. A geometrical simulation is used, with a wind speed of 7 ms^{-1} to ensure appropriate sampling of the low spatial frequencies, with turbulence strength directly measured from the centroid variance. A random sample of 'input' r_0 values is chosen, between 0.08 m, and 0.4 m, but r_0 is always set equal for the two atmospheres. The measured r_0 for the two independent realisations are plotted against each other. For the 240 input turbulent straights, the best fit gradient of

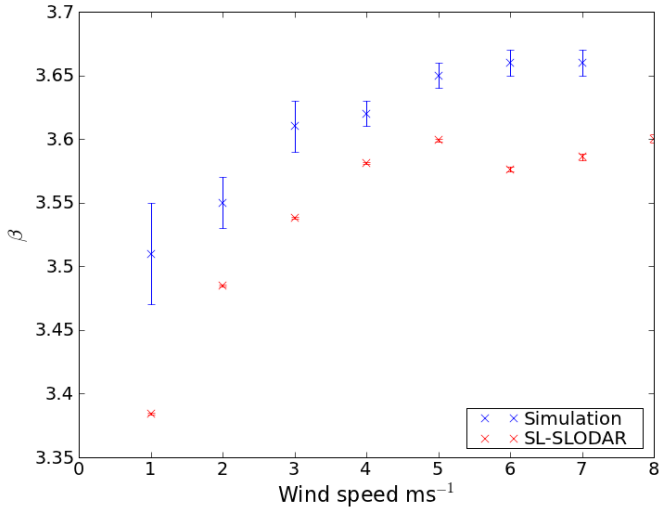

Figure 6.13: Comparison of the wind speed vs. β plots for SL-SLODAR data and Monte-Carlo simulation. Even though the SL-SLODAR measures a systematically lower β value than the simulation, we see they both hit their asymptotic values at a wind speed of approximately 4 ms^{-1}, suggesting this is the minimum speed required for sufficient averaging when using the SL-SLODAR parameters. The measured values for beta are still slightly lower than 11/3, probably due to the small but significant quantity of dome seeing observed by the instrument.

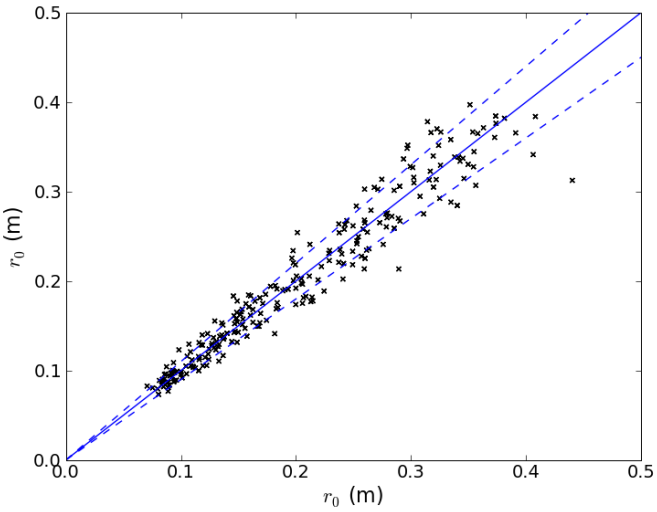

Figure 6.14: Plot of two simulated SLODAR measurements of r_0, for independent realisations of a turbulent atmosphere with identical strengths. The dotted line shows the best fit to the data, of gradient 1, and the dotted line the standard deviation between the two measurements of 0.1.

the graph is 1.00 ± 0.01. However a more useful result is the average standard deviation of the ratios between the measured strength for the two phase screens. The standard deviation has a value of 0.1, implying a measurement of r_0 is only accurate to within $\sim 10\%$ for any turbulence strength.

6.3.3 Temporal Sampling

To measure the speed and direction of atmospheric turbulence in the cross and auto covariances, the time between Shack Hartmann image frames must be smaller than the time it takes the turbulence to cross the telescope (see equation 2.47). The La Palma SLODAR has an operating frequency of 37 Hz, and the SL-SLODAR of 57 Hz. Figure 6.15 shows the maximum wind speed that can be measured by these two instruments, for both 40 and 50 cm telescopes. The FA-SLODAR currently can only detect wind speeds of 66.6 kmh^{-1} (18.5 ms^{-1}), and the SL-SLODAR of 103 kmh^{-1} (29 ms^{-1}). It is important to note that the high altitude turbulence can still be sensed from measurements of the auto–covariance.

This problem has come to light during the La Palma SLODAR observing campaign,

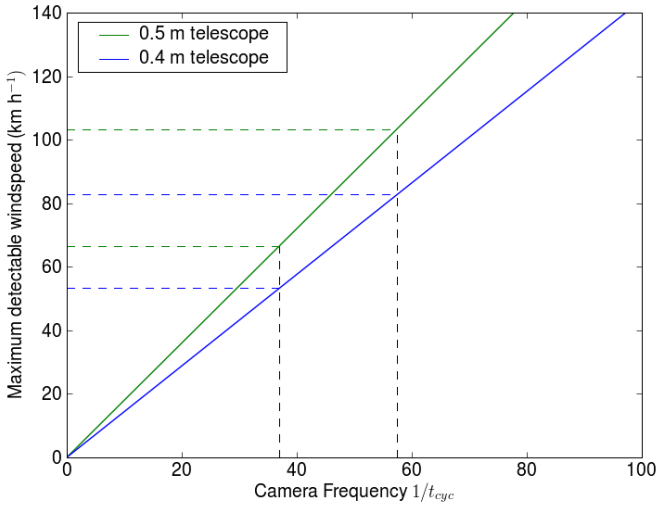

Figure 6.15: Maximum wind speed detectable by SLODAR for a 40 cm and 50 cm telescope. The maximum detectable windspeed for given camera frequencies is shown. FA-SLODAR operates at 37 Hz, and SL-SLODAR at 57 Hz, leading to maximum detectable windspeeds of 67 kmh^{-1} and 103 kmh^{-1} respectively.

where turbulence has been observed in the unresolved bin, however only one layer with measurable velocity can be observed in the auto-covariance.

In theory this issue is also present when applying temporal offsets to SCIDAR covariances. However, as SCIDAR is typically applied to large telescopes, the wind speed would have to be unphysically high not to be sensed.

6.3.4 Dome and Tube turbulence

In section 2.2.8 the concept of *dome seeing* was introduced, with the example of the CFHT. This phenomena however is also seen on the small telescopes used for SLODAR turbulence profiling. This turbulence often produces a narrow peak in the SLODAR covariance function, and exhibits very slow temporal evolution. Figure 6.16 shows one example auto covariance, with a fast layer moving toward 'eleven o'clock', and a slower towards 'two o'clock'. In the centre we see a peak corresponding to either dome or telescope tube turbulence, identified by the fact that no clear translational velocity is seen, and in many cases appears to simply 'decay' as the temporal offset is increased.

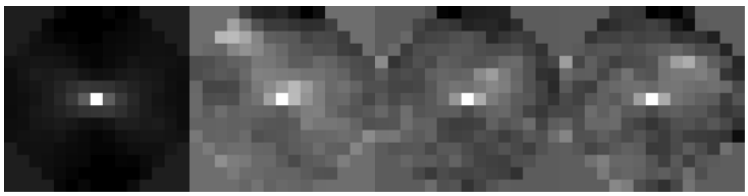

Figure 6.16: An illustration of the effect of dome and tube seeing on SLODAR auto covariance. The temporal offset increases from left to right. The are two atmospheric layers evidenced by the moving 'blobs', and dome or tube seeing manifesting as the central peak, with no motion and a slow decay. Each frame is independently scaled.

Various incarnations of SLODAR, for example that deployed by Goodwin *et al.*, apply a 1 or 2 Hz temporal filter to the centroid variance to remove the effect of dome seeing [88]. However this has the additional effect of removing low spatial frequency components of measured atmospheric turbulence. This can be illustrated with a simulated example using the parameters of the current La Palma SLODAR, which runs at a frame rate of 37 Hz. Using a geometric simulation with two translating phase screens at 7 ms^{-1} (25 kmh^{-1}), and two turbulent layers, temporal filters of 1 Hz and 2 Hz are applied, and the effect on the profile are measured. These results are shown in figure 6.17, and for a 1 Hz filter the peaks are supressed by 11%, and for the 2 Hz filter the suppression is 22%, showing that the application of a temporal filter has a significant effect on the measured atmospheric turbulence, and should be avoided where possible.

However, dome turbulence has a significant impact for SLODAR observations, and so it is important to consider how to prevent it occurring, and how to minimise any effects it may have.

The La Palma SLODAR exhibits significant dome seeing. It is likely that heat sources in the dome contribute to this effect, in addition to poor ventilation to clear the heat. Due to logistics there are multiple PC's and a telescope controller located in the dome, all acting as a heat source. In addition all these heat sources sit below the height of the open dome, and the dome itself is sheltered by the lift shaft and telescope dome of the WHT building. The WHT building itself will also radiate heat through the roof.

In contrast however, there is substantially less tube and dome seeing at Paranal. The telescope enclosure is open sided, allowing the wind to clear out any slow moving turbulence

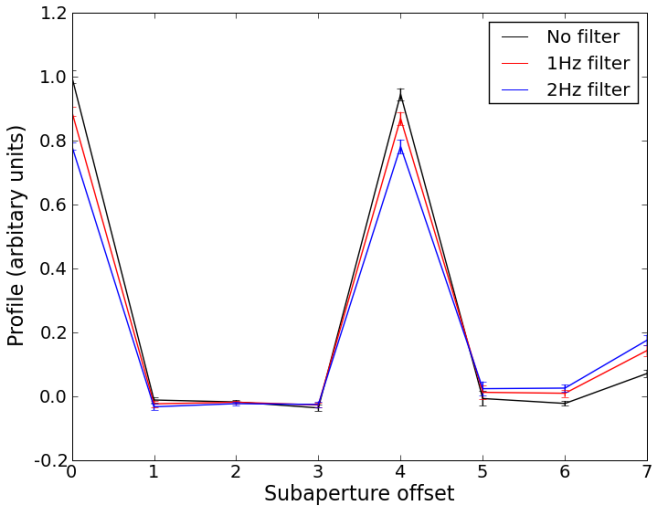

Figure 6.17: An example of temporal filtering on a SLODAR turbulent profile, generated from a geometric simulation using parameters from the current La Palma SLODAR, including a frame rate of 37 Hz. The application of temporal filters causes a marked suppression in the measured turbulence strength. Each layer has a speed of 7ms^{-1}. The uncertainties are found from multiple independent realisations of the Monte Carlo phase screens.

and rising heat. In addition the computers and telescope controller are located in a cabinet away from the telescope itself. A unique property of the surface layer at Paranal is its weakness when the wind blows from a southerly direction. This can be observed in figure 6.18, and because of this we can conclude that the dome seeing is also very weak. No temporal filtering is applied to the data.

Clearly the Paranal setup substantially reduces dome seeing, and measures are now being taken to improve the environment of the La Palma SLODAR.

6.3.5 SL-SLODAR specific considerations

Currently the SL-SLODAR instrument at the VLT is in the process of being *Paranalized*, that is being upgraded into an ESO facility instrument. The simulation tools discussed earlier in the thesis can help resolve practical considerations during the course of the upgrade. One particular consideration is the effect of rotational misalignment of the two CCD detectors. The two detectors have to be accurately aligned to ensure a correct cross correlation between the two spot patterns. There is a manufacturing tolerance of $\pm 1^\circ$ on the alignment

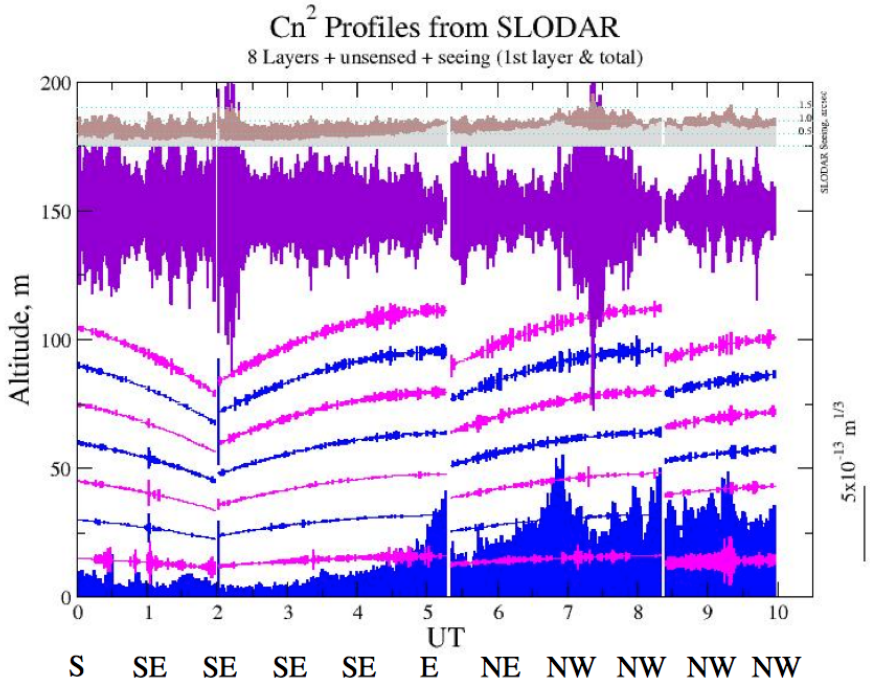

Figure 6.18: An example of SL-SLODAR turbulence profile showing an absence of dome seeing and surface layer of turbulence for the early part of the night, along with the wind directions. The surface layer of turbulence only develops at 5 UT, as the wind moves away from the South and South East. As no temporal filtering is applied to the data, we conclude there is very little tube or dome seeing present at this instrument. (Turbulence profile plot, retrieved on Aug 2, 2012 from http://www.eso.org/gen-fac/pubs/astclim/paranal/asm/slodar/Paranal/2012-03/slodar-fxl-2012-03-06.jpg. The wind direction annotations added by the author.)

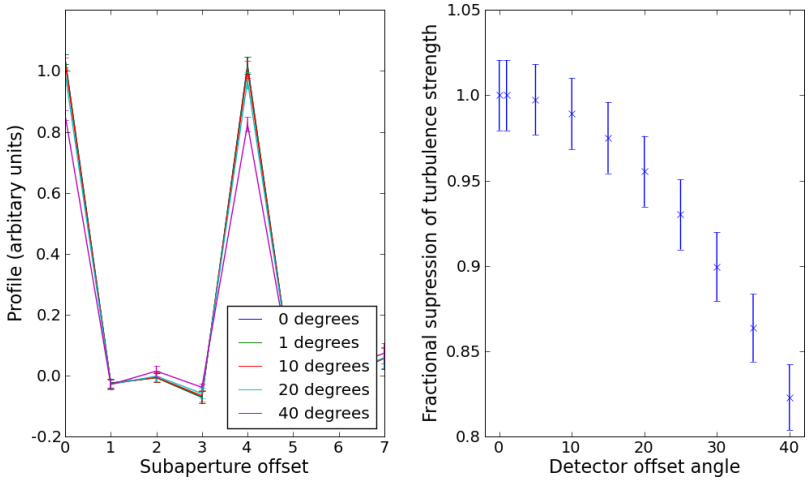

Figure 6.19: Figure showing the effect of rotational misalignment for the two detectors in an SL-SLODAR system. The results are generated from a geometric simulation, of two equal layers. The left hand plot shows the suppression of measured profile, for different rotations, however in all cases the underlying shape of the profile is the same. The right hand figure shows the fractional suppression of the fitted turbulence strength for increasing camera rotations. (For an offset angle of 10°, the rotation of the cameras are +5° and −5° respectively).

of the chip to the camera body, so assuming the camera bodies themselves are aligned, this could lead to up to a two degree offset between the two chips.

A two layer geometric simulation was used, with layers corresponding to sub-aperture offsets of 0 and 4 each with equal turbulence strength. The centroids were measured and a rotation matrix was applied to these measurements. The data was then reduced in the usual fashion. Figure 6.19 shows the results of this simulation. The overall shape of the profile is not affected for the range of offsets simulated. However a clear suppression of the turbulence strength can be seen in the second plot in the figure. We can conclude that the alignment tolerance of the detectors is ±5° for each detector.

6.4 Discussion of the effect of weather conditions and local topography

6.4.1 La Palma

Long term site monitoring on La Palma

There have been several long term site monitoring campaigns at the ORM, mainly concerned with measuring the overall seeing quality[1]. These include the Half Arcsecond Program [89], SCIDAR campaigns on the NOT [80], and the long term operation of the RoboDIMM discussed above. As we shall see in the next section, the long term evolution of seeing is coupled with the effects of climate change and the evolution of weather patterns.

The Half Arsecond Program involved measuring the seeing using JOSE, an instrument on the WHT, and comparing concurrently with an external DIMM. Between October 1994 and August 1998, a median seeing of 0.69" was measured, and was shown at all times to be in agreement with the DIMM. Fuensalida *et al.* performed a SCIDAR campaign on the NOT in the years 2004 and 2005, measuring 104 nights over the course of the two years, measuring median seeing of 0.8". The RoboDIMM itself has been operating continuously since the first quarter of 2008, and the median and quartile values for each year are shown in table 6.4.1.

Anecdotal evidence from astronomers on La Palma has suggested a worsening of image quality over the years [90]. However without continuous long term data we are unable to draw conclusions on the seeing getting worse. Perhaps the time of the half arcsecond program was unusually good, or they had a bias towards summer observing therefore biasing the statistics. This points towards a need to have independent site testing instruments on La Palma, to provide long term measurements of the seeing and the optical turbulence profile over many years. We note too that the RoboDIMM measures large seasonal fluctuations in seeing, with the Summer (April-September) median being 0.78" and the Winter median being 0.95". The regular nature of these fluctuations can be see in figure 6.20. There is evidence that this discrepancy is caused by differing prevailing conditions between the winter

[1] The atmospheric turbulence limited angular resolution of a telescope.

	Seeing (arcseconds)		
Year	Lower Quartile	Median	Upper Quartile
2008	0.60	0.78	1.07
2009	0.64	0.84	1.15
2010	0.63	0.81	1.04
2011	0.65	0.86	1.19

Table 6.1: Median and Quartiles for seeing measured by the ING RoboDIMM each year between 2008 and 2011. The RoboDIMM has been operating continuously in this time, and in all seasons. The median values are consistent from year to year given the size of the quartile range.

and summer months, with the average wind direction in the winter months being 175°, and in the summer 135°.

In addition to any seasonal effects, in section 6.2.3 we show strong directional effects on the seeing measured. The conditions exhibiting strong seeing (and large differences between DIMM and SLODAR data) correspond to winds from the direction of the Caldera de Taburiente, a significant geographical feature. It is likely this links with the seasonal effects seen on La Palma, as discussed in the previous paragraph.

There is no conclusive evidence that the seeing on La Palma has got noticeably worse over the years. With the installation of a turbulence profiler more evidence can be gathered on the long term stability of the conditions as the site.

6.4.2 Paranal

Brief review of *ESO Messenger* 132:11

Sarazin *et al.* comment that since the commissioning of the VLT, the seeing measured by the DIMM has been noticeably worse than that of the UT's. This was first quantified in 1999 by the test camera during the commissioning of UT2. These tests on their own however are inconclusive, as the seeing can fluctuate rapidly over short time scales (hour to hour, and night to night), and so these results could not provide statistically significant results [91].

Sarazin *et al.* present results comparing the seeing from the FORS2 spectrograph on UT2, and the ESO DIMM. FORS2 was chosen as it presents the most complete data set. It is noted that the DIMM seeing is often significantly worse than FORS2, and give values

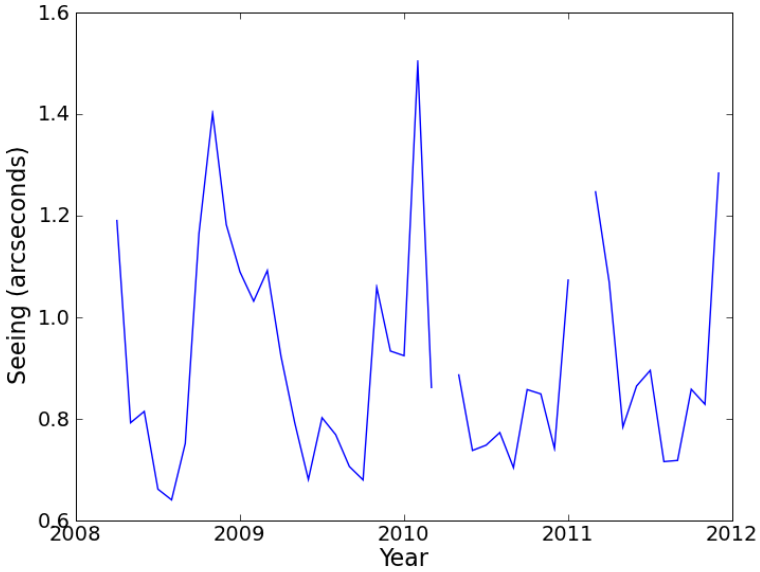

Figure 6.20: Figure showing the monthly median seeing recorded by RoboDIMM between 2008 and 2012. The seasonal pattern can clearly be seen, with much worse seeing in the winter months and a regular period from year to year. There are no clear trends for the long term evolution of seeing in this time. The year label corresponds to the January of that year. Gaps are where there are no RoboDIMM measurements for that month.

for the mean DIMM seeing (0.81") and mean FORS2 seeing (0.65"). They also note that in good seeing conditions the DIMM seeing is often better than FORS2, and in bad seeing conditions it can be a lot worse.

Having presented the case for further study of these effects, a larger set of UT data was required. The quality control systems for the active optics on the UT's record Shack Hartmann spots continuously. Hence the FWHM given by these spot patterns can be compared to the DIMM giving a virtually continuous dataset.

Using a combination of MASS, SLODAR, and DIMM data it is shown that for the vast majority of cases the ground layer turbulence is all contained below 94 m. The SLODAR data shows a large fraction of the turbulence very close ground, and Sarazin *et al.* suggest the discrepancy between the DIMM and UT could be explained if much of the ground layer turbulence is below 20 m, so that it is seen by the DIMM but not the UTs. The DIMM data was corrected for a surface layer of strength determined by SLODAR. The plot shows compelling evidence that the surface layer is the most likely explanation for the discrepancy.

Having shown strong evidence that the discrepancy between the DIMM and UT seeing is caused by a layer of turbulence below the UTs, Sarazin *et al.* turn to data taken from the weather tower at Paranal. Wind roses are presented showing both the deference in seeing between both the DIMM and UT (figure 6.21), and the temperature gradient between 2 and 30 m as a function of wind direction. The biggest seeing discrepancy occurs when the wind comes from NNE and SSE, and the biggest temperature gradient when the wind comes from the NE and SSE. They conclude that bad seeing occurs when warm air from the mountains along the Atacama fault is blown along the top of the mountain. This effect is known colloquially as the 'Bolivian Winter' [92]. The discrepancy is becoming *worse* over time, and they illustrate the proportion of wind from different directions for 1985 and 2007.

This data leads Sarazin *et al.* to a notable conclusion. The seeing change at Paranal is caused by local winds, but these are caused by climate events on a global scale, so global climate change has been observed at Paranal.

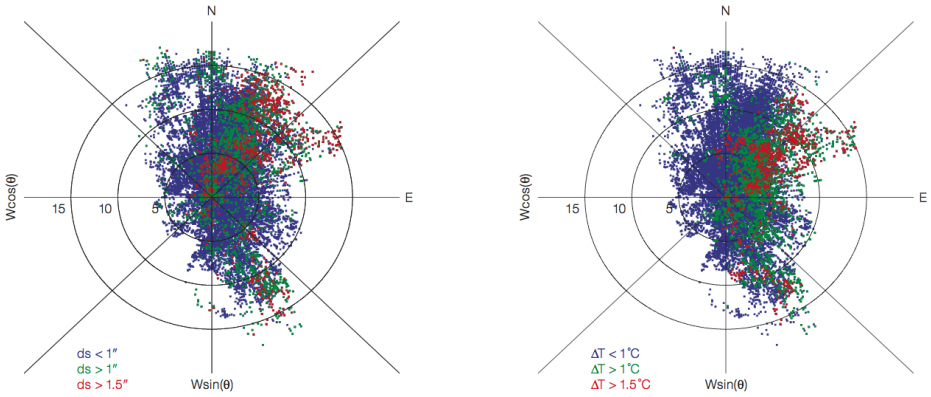

Figure 6.21: Wind roses for Paranal, colour coded by discrepancy between DIMM seeing and UT image quality (left), and the temperature gradient between 2 and 30 m (right). Plots taken from [91].

Direction	Jan 1985	Jan 2007
NNE	6%	23 %
NE	5%	12 %
SSE	2%	9 %
S	0%	4 %
Total	13%	48%

Table 6.2: Frequency of the wind directions at the Paranal observatory, for the directions that result in the large seeing discrepancies. The numbers are taken from the best fits of data presented in [91]. They show a dramatic change in wind direction in the 22 years after 1985.

Role of SL-SLODAR

The work by Sarazin *et al.* led to the installation of a SL-SLODAR at Paranal, to profile in much greater detail this surface layer of turbulence [47]. Since March 2011 the instrument has been operating robotically so the body of data now allows a statistical analysis to be performed on the SL profile.

The weather data from the robotic monitor adjacent to the SL-SLODAR instrument is publicly available, and so a comparison of key parameters of the surface layer can be made with wind conditions. Figure 6.22 plots four roses, showing the mean integrated turbulence up to different heights, the first bin, $\leq$ 10 m, $\leq$ 50 m, and $\leq$ 100 m. This plot clearly illustrates the directionality eluded to in figure 6.18. When the wind blows from southerly and south westerly directions, there is a very weak surface layer with almost no turbulence directly at the ground. For all other wind directions significant turbulence at the surface is observed. However when the wind blows from the north east and east significant turbulent structure appears over the full height of the surface layer profile. These same results are plotted for seasonal variation in figure 6.23, for summer (October to March) and winter (April to September). The stronger and more structured turbulence occurs in both seasons, however it is significantly stronger during the winter months.

We compare these turbulence profile roses against the seeing discrepancy presented by Sarazin *et al.* shown in figure 6.21. There is a directional correlation (for the wind) between turbulent structure throughout the surface layer and high discrepancy between the DIMM and UT seeing.

The height of the VLT mirror is approximately 10 m above the ground, and the top of the domes have a height of 30 m. From the turbulence profile roses it is clear that on average the turbulence is mostly below the mirror height for any wind directions other than from the north east and east. In section 2.2.8 we present the cases for turbulence profiling in terms of deciding what configuration of AO system (if any) would be most suitable. The roses imply that there are certain wind directions where GLAO (as an example) would be most effective at Paranal. Analysis of the weather data show these conditions occur 14% of the time. In cases such as this, a detailed profile of the surface layer can provide crucial evidence for the benefits of corrective optics.

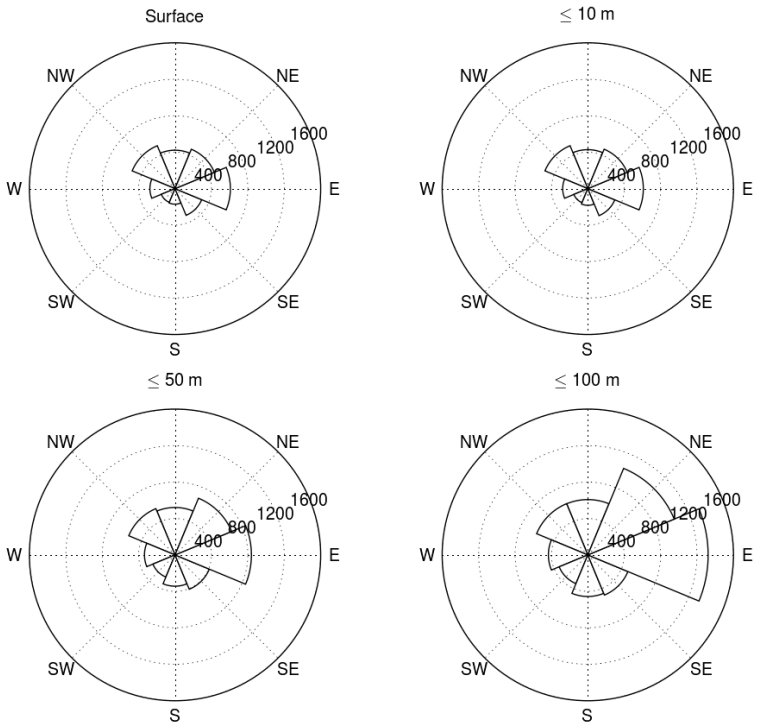

Figure 6.22: Directional effects on the SL-SLODAR profile at Paranal, for different heights. Clockwise from top left, the surface bin, $\leq$ 10 m, $\leq$ 50 m, and $\leq$ 100 m. The azimuthal axis indicates the direction from which the wind blows, and the radial axis the integrated turbulence strength in units of $\times 10^{-15}$ m$^{1/3}$. Between south and south west there is a very weak surface layer, and higher altitude effects typically only occur for wind blowing from the east or north east.

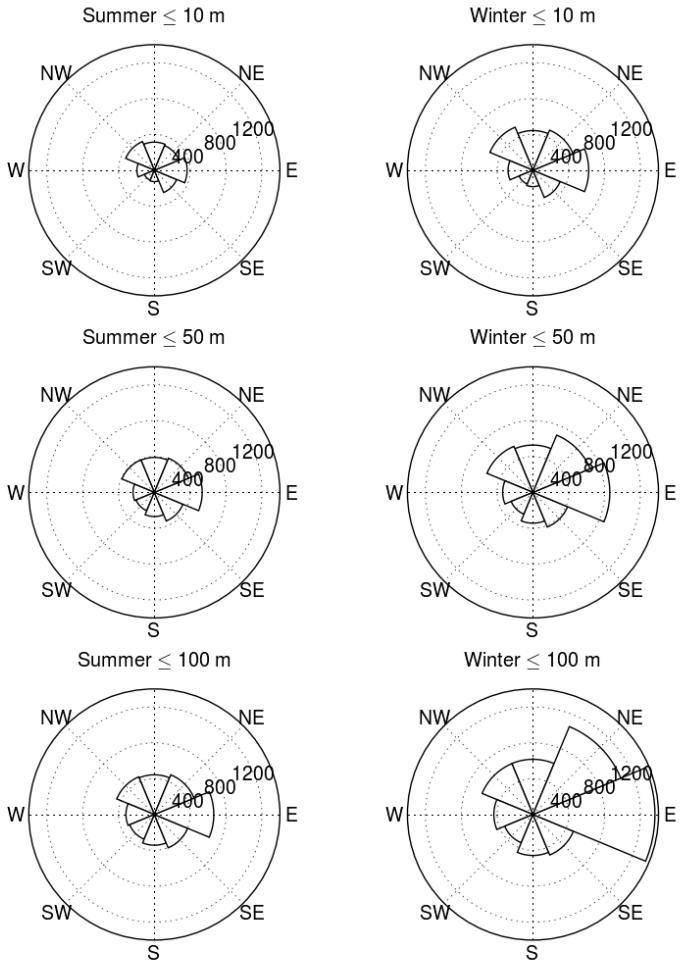

Figure 6.23: Directional effects on the SL-SLODAR profile at Paranal for the summer (October to March) and winter (April to September). The azimuthal axis indicates the direction from which the wind blows, and the radial axis the integrated turbulence strength in units of $\times 10^{-15}$ $m^{1/3}$. The increase in turbulence strength during the winter can be clearly seen, as can the significant increase for wind blowing from the east or north east.

From the data from the La Palma SLODAR presented in section 6.2.3, we see clear effects of local geography on the measured turbulence. At Paranal there is evidence for the effect of man made structures causing local effects, in this example the dome for the VLT Survey Telescope (VST). An arial photograph of the Paranal site is shown in figure 6.24, with the MASS-DIMM, SLODAR, and VST labelled. When the wind blows from the south, we see the MASS-DIMM is in the wake of the VST dome, but the path to the SLODAR is not obstructed. In figure 6.25, there is an example for two nights, March 9, 2012 (wind from the south) and March 28, 2012 (wind predominately from the north east), showing integrated DIMM and SLODAR seeing. We see for the southerly wind the DIMM measures significantly more turbulence than the SLODAR, whereas for the other wind directions there is good agreement between the two instruments. In figure 6.26 we show the corresponding turbulence profiles, and for the night with large discrepancy between the SLODAR and DIMM there is very little surface layer turbulence. We therefore conclude that the VST dome is causing turbulence that the DIMM measures, but the SLODAR does not. The DIMM and SLODAR are only separated by 10 metres, so this is a significant local effect.

6.4.3 Conclusions

Large scale changes in the atmospheric circulation have been observed across South America between 1899–1986, and interdecadal changes have been measured. Additionally instrument records, SODAR style measurements, and satellite data show variation, fluctuations, and "sudden jumps" in features of atmospheric circulation over South America, suggesting that this long term evolution of seeing conditions may well continue [93]. For the E-ELT the ground layer is potentially not an issue, as the primary mirror will sit 30 m above the ground, but these changing conditions may well lead to increases in PBL or free atmosphere turbulence, furthering the case for extensive and long term site testing campaigns, and also for monitoring concurrent with observations.

The seeing and the turbulence profile at both Paranal and La Palma are affected by local orography, as seen in sections 6.2.3 and 6.4.2. We see effects of both natural features, and also man made structures. The prevailing weather conditions have changed at Paranal, and with it has bought a change in seeing conditions. There is no evidence for such changes on

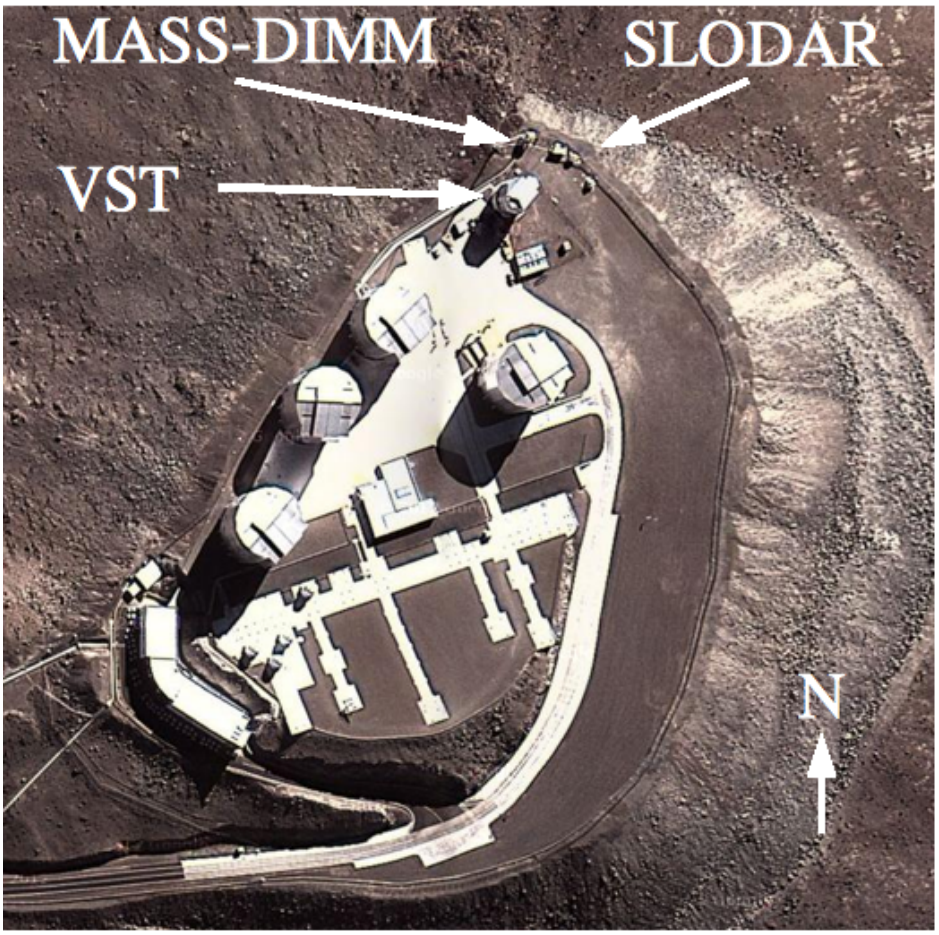

Figure 6.24: Arial photograph of the observing platform at Cerro Paranal, showing locations of the MASS-DIMM, SLODAR, and VST. For southerly winds the MASS-DIMM is in the wake of the VST dome but SLODAR is not. (Photo of Cerro Paranal, Chile, retrieved on Sept 11, 2012 from website http://maps.google.co.uk/).

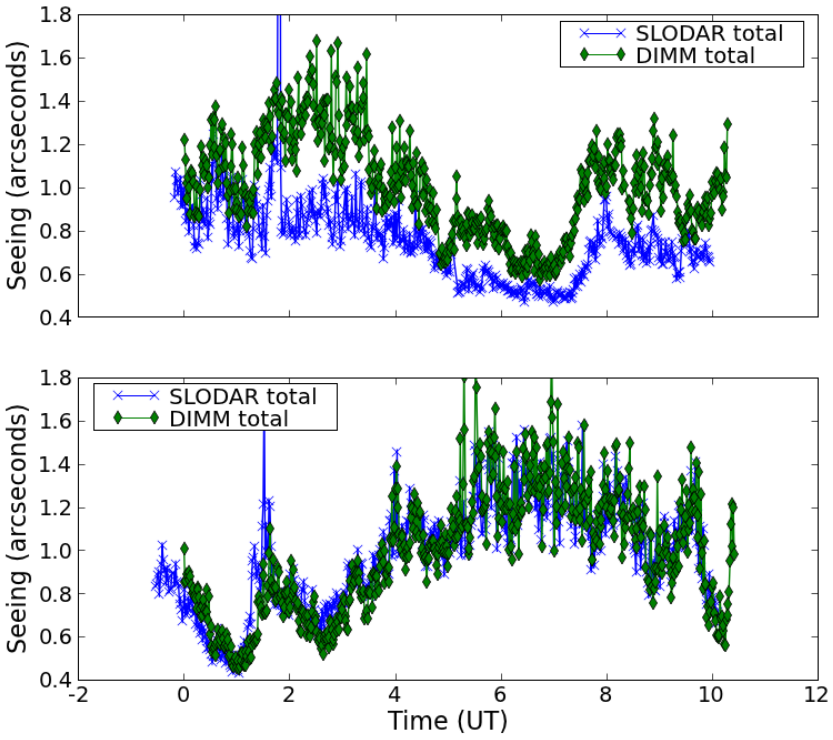

Figure 6.25: Plot of SLODAR and DIMM total seeing for 2 nights at Cerro Paranal, (top) March 9, 2012 (wind from the south) and (bottom) March 28, 2012 (wind predominately from the north east). We see for the southerly wind the DIMM measures significantly more turbulence than the SLODAR, and for the north easterly wind there is good agreement between both instruments. The corresponding turbulence profiles are shown in figure 6.26.

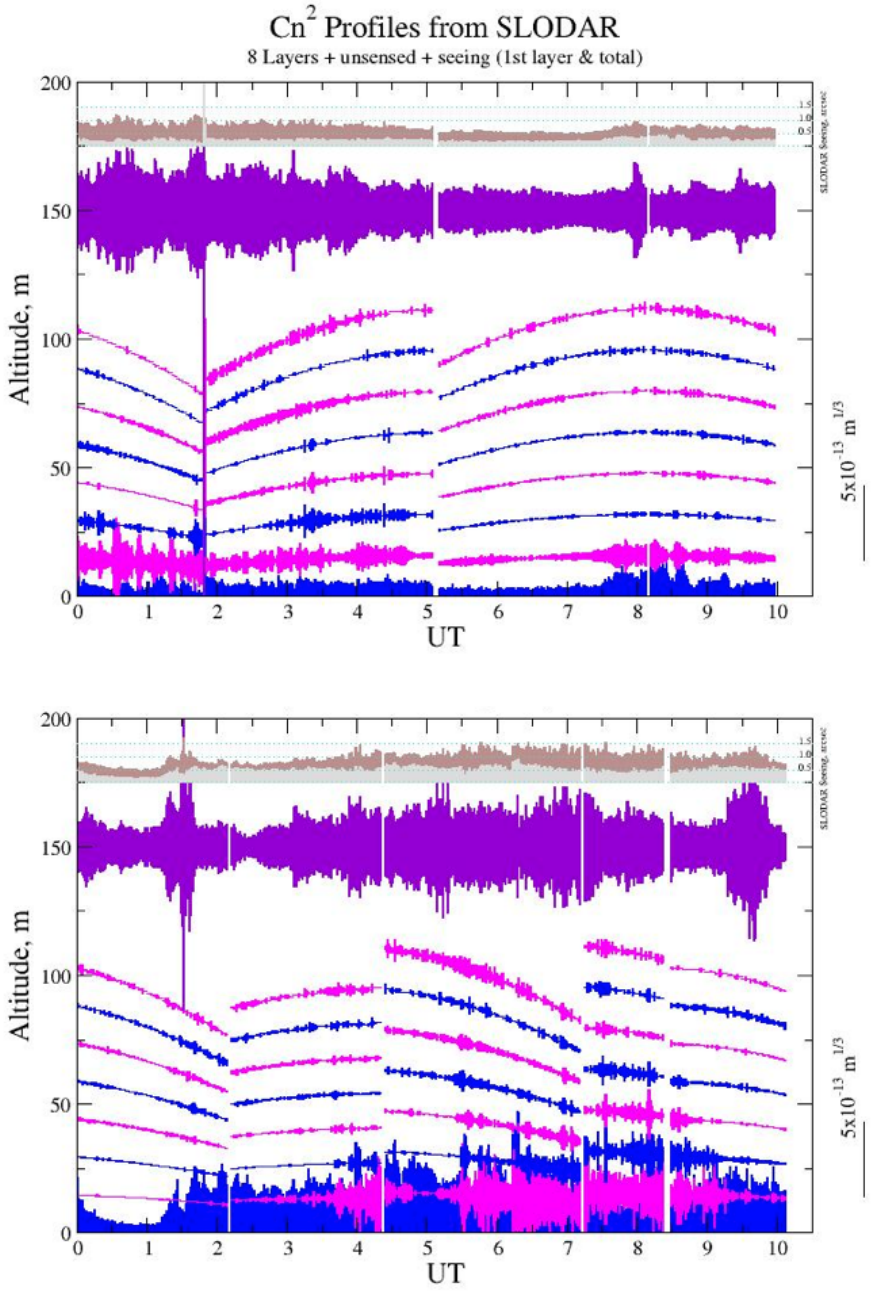

Figure 6.26: Turbulence profiles corresponding to the plots in figure 6.25, (top) March 9, 2012 (wind from the south) and (bottom) March 28, 2012 (wind predominately from the north east).

La Palma, but it is clear that any change in the prevailing surface layer winds would have significant consequences for the seeing at the observatory.

6.5 Conclusion

The La Palma SLODAR was introduced, including a description of the instrument, and its role in a profiling campaign to provide both long term data, and support measurements for CANARY. The data was compared with the ING facility DIMM, where there was a large discrepancy between the two instruments as the wind blew from the Caldera de Taburiente, but only for bad seeing conditions. The measurements made by the SLODAR were verified to ensure the measurements of turbulence were not saturating. By calculating the average profile of turbulence the profile is shown to be highly ground layer dominated, with any discrepancy between SLODAR and DIMM occurring in a region below 514 m.

A discussion is made of a long term issue with historical SLODAR instruments, that of measuring a non Kolmogorov power spectrum with a lower value of β than expected. Studies have made conclusions that non Kolmogorov turbulence is measured, however we show using measured data and simulations that this is indistinguishable from insufficient sampling caused by low wind speed. This is a problem that also affects the DIMM. In such conditions the SLODAR under estimates turbulence strength, and the DIMM over estimates.

Dome seeing has been a recurring issue for SLODAR, temporal filtering has previously been used to remove the low temporal frequency components associated with dome seeing. However it is not possible to separate out the frequencies corresponding to genuine atmospheric turbulence and those associated with the dome. Using simulations we show that applying a spatial filter leads to a significant underestimation of all turbulence strength.

A rather specific concern for the upgrade to SL-SLODAR involved the manufacturing tolerances of the CCD chip, and the potential rotational offsets between the the chips in the two cameras used in the instrument. We show through a geometric simulation that given the manufacturing tolerances of the instrument, this will have minimal effect on the measured turbulence profile.

Anecdotal evidence at the ORM on La Palma suggests the worsening of seeing quality over time, however the results from the half arcsecond program, and the DIMM and SLODAR present no evidence of this. However with the installation of a permanent turbulence profiler on the roof of the WHT a long term campaign including turbulence profiles can be carried out. The local orography is shown to have a significant effect on measured turbulence, however there appears to have been no change in prevailing weather conditions.

The surface layer SLODAR at Paranal has been operating for a year, and when the turbulence profiles are analysed with wind data, clear meteorological and seasonal effects on the strength and structure of the surface layer have been observed. The surface layer profile exhibits significantly more turbulent structure when the wind is from the North or North east. The turbulent strength in the surface layer is stronger in the winter, but disproportionally stronger for the North and North Easterly winds.

Chapter 7

Conclusion

This chapter presents a summary of the conclusions from the preceding three chapters, and of proposed future work.

7.1 A summary of conclusions

The work described in this thesis is set within the underlying theme of atmospheric turbulence profiling. There are four main subjects covered, scintillation based turbulence profiling (SCIDAR), phase based turbulence profiling (SLODAR), combining the two (FA-SLODAR) and site monitoring campaigns. In this chapter, the results of the work are summarised.

7.1.1 Stereo SCIDAR

SCIDAR is a turbulence profiling technique involving the correlation of scintillation patterns produced by double stars.

- Separating the two stars onto individual CCD detectors allows very 'clean' covariance images to be produced as the intensity patterns can each be normalised independently. Allowing each arm to dynamically reconjugate gives an increase in altitude resolution above conventional SCIDAR. Altitude resolution of $\sim 100 - 200$ m is good enough for real–time optimisation of LTAO for ELTs. This is the first demonstration of a technique that can provide this resolution over the whole atmosphere in real time.

- If the SCIDAR instrument observes non Kolmogorov turbulence, the only significant effect is a reduction in the peak of the turbulence profile. However if $\beta \geq 3.444$ there is minimal effect on the measured turbulence strength.

- An on sky example taken at the WHT showed a seven layer turbulent atmosphere, the turbulent layers are confirmed as they all exhibit either dispersion or wind shear when a temporal offset is applied to the cross covariance matrix.

7.1.2 FA-SLODAR

SLODAR is an analogous double star profiling technique, using the phase gradient variance as measured by a Shack Hartmann wavefront sensor.

- Atmospheric scintillation causes a suppression of phase gradient as measured at the ground, and this could lead to an underestimation of measured turbulence. Modified SLODAR response functions have been calculated and verified by Monte-Carlo simulation to correct for this effect. The numerical integration is robust over a physically realistic range of inner and outer scales.

- Using the scintillation variance from sub apertures it was shown using simulation that it is possible to retrieve an estimate for the strength and altitude of turbulence that is not directly sensed by cross beams. This was performed for the first incarnation of the SLODAR instrument with 4.75 cm subapertures.

- After the upgrade of the SLODAR systems to telescopes with 6.25 cm subapertures, the full analytical equation for scintillation variance could no longer be used, and so the system was re–calibrated using Monte Carlo simulation.

- On sky data from the SL–SLODAR observing campaign was analysed and compared against results from the MASS turbulence profiler. While there is correlation between measurements of turbulence strength and turbulence altitude between the two instruments, there are systematic errors still to be understood. The new response functions are shown to provide a more appropriate estimate for the strength of unresolved turbulence than the difference method.

7.1.3 La Palma SLODAR observing campaign

A SLODAR system was deployed on La Palma taking 50 nights of data between September 2011 and April 2012.

- The SLODAR system operated concurrently with the DIMM seeing monitor for these nights.

- There was good agreement between the seeing measured, for seeing better than 1.5 arcseconds, and then a large discrepancy where the DIMM estimated significantly higher turbulence strength than SLODAR. This discrepancy appears to have no dependency on wind speed, and the SLODAR measurements do not saturate. Plotting the directionality of this discrepancy we see that it occurs in times of bad seeing when the wind is blowing from the Caldera de Taburiente.

- In this observing campaign we measure a very ground layer dominated winter profile, and a ground layer with scale height 760 m. This is in agreement with the seasonal results from SCIDAR. The SLODAR operated for 3 nights in August 2012 after an upgrade, where a significant turbulent layer is seen at ~ 4 km.

7.1.4 Practical Effects on SLODAR

In the course of SLODAR instruments being deployed on small telescopes, there have been a variety of practical issues to be addressed, that have the potential to reduce the accuracy of the instrument.

- SLODAR instruments have measured values for the power spectrum of turbulence that deviates from the expected Kolmogorov spectrum. We show that this can rise from dome seeing, and also from insufficient sampling of the atmospheric turbulence in low wind speeds. Some implementations of SLODAR have applied a high pass temporal filter, however we show that this approach also effects the measured turbulence profile, leading to an underestimation of turbulence strength. Until the dome seeing is removed it is inappropriate to use the corrected response functions, as they in effect increase the value for β above 11/3. The corrected responses are broader than the uncorrected

ones, and so if fitted to the narrower peaks of the dome seeing would increase additional error.

- Due to the random nature of the turbulent atmosphere, using typical SLODAR parameters we show from simulation that there will be a 10% scatter on the measured values for r_0, even when the underlying value for r_0 is constant.

- The speed and direction of turbulent layers can be retrieved from the SLODAR cross and autocovariance matrices by the application of a temporal offset. However the speed of the layers that can be detected is limited by the cycle time of the CCD detector, meaning the La Palma SLODAR system can not detect layers faster than 18.5 ms^{-1} and the SL–SLODAR not faster than 29 ms^{-1}. The strength of this turbulence *can* however be measured.

- The surface and ground layers of turbulence have a strong dependence on prevailing weather conditions. Analysis of the surface layer at Paranal shows turbulent structure through the first 100 m only occurs for wind directions between the north and north east. In addition the surface layer is very weak when the winds are from between the south and west.

7.2 Proposed future work

7.2.1 SCIDAR

A second observing run is scheduled on the Nordic Optical Telescope in October 2012, and the proposal is to analyse SCIDAR data in conjunction with SLODAR data from the roof of the WHT. The effect of reconjugating the instrument on the measured turbulence profiles will be investigated. As the two instruments are in dramatically different locations at the ORM they will see common high altitude turbulence, and potentially different effects from the surface layer. As the S-SCIDAR can be conjugated to below ground level it may be possible to investigate discrepancies between the two locations at the site. However as noted above, the power spectrum of the surface layer can not be investigated using SCIDAR.

7.2.2 Full atmosphere SLODAR

The FA SLODAR method has been shown to be successful, in terms of fitting the strength and altitude of non directly sensed turbulence. In comparisons with MASS there are high amounts of scatter, and systematic differences for higher altitudes that require further investigation. It would be useful to mitigate the dome seeing present at the La Palma SLODAR by relocating equipment currently in the dome. This would allow the use of propagation corrected SIRFS. It would then be possible to compare the fitted high atmosphere turbulence to a high resolution profiler such as SCIDAR to fully understand the applications and limitations of the new process.

7.2.3 Geographical and Meteorological Effects

From the comparison of the SLODAR and DIMM seeing at the ORM, even for two instruments situated within a few tens of metres of each other, we see strong correlation for certain climate conditions, and a strong discrepancy for others, linked to geographical features. The effects seen could correspond to several factors, including difference in turbulence strengths in localised areas, or non–Kolmogorov turbulence measured. Additionally at Paranal, differences between the SL-SLODAR and MASS-DIMM profilers can be explained by their respective locations relative to the wake of a telescope dome.

An interesting avenue of future study would be to provide a surface layer turbulence profile for different locations across an observatory. Ideally multiple SL-SLODARs would be used to measure both the surface layer and any high altitude turbulence, however this approach would be costly, and the instrument would have limited portability.

For a more portable and cost effect method to measure local differences in seeing, I propose an experiment using multiple DIMM instruments on small telescopes taking measurements concurrently at different locations round an observatory site (and even within telescope domes). The multiple DIMMs could be calibrated together, to allow for reliability between measurements. Combined with a single full atmosphere profiler (for example a SLODAR with 100 m resolution), this would allow the effects of common high altitude turbulence to be removed. For each site a data set for the ground layer with respect to location

and weather conditions could be constructed. The use of a DIMM based on a 5 inch telescope has been demonstrated [94], mitigating cost issues and allowing for ultra portability. Ideally slightly larger telescopes would be used, but they would still be significantly smaller than the 16" telescopes required for SL-SLODAR.

To investigate the possibility of non–Kolmogorov turbulence in the surface layer, it is imperative that dome seeing be removed from the profiler, physically rather than by any post processing of data, as such seeing demonstrably does not obey the Kolmogorov power law. To fully average the statistics for low wind speed, long sampling times are required to fully measure low spatial frequencies. The Monte-Carlo simulation can be used to choose minimum sampling times.

Bibliography

[1] J.W. Hardy. *Adaptive Optics for Astronomical Telescopes*. Oxford University Press, New York, 1998.

[2] F.J. Rigaut, B.L. Ellerbroek, and R. Flicker. Principals, limitations and performace of multiconjugate adaptive optics. In *Proceedings of the SPIE*, volume 4007, pages 1022–1031, 2000.

[3] E. Hecht. *Optics*. Addison Wesley, San Fransisco, 4th edition, 2004.

[4] V.N. Mahajan. *Aberration Theory Made Simple*. SPIE, 1991.

[5] A.N. Kolmogorov. Dissipation of Energy in the Locally Isotropic Turbulence. *Reprinted in Royal Society of London Proceedings Series A*, 454:15–17, 1991.

[6] V. Tatarski. *Wave propogation in a turbulent medium*. McGraw-Hill, New York, 1961.

[7] J.W. Goodman. *Statisitcal Optics*. John Wiley & Sons, New York, 1985.

[8] F. Roddier. The Effects of Atmospheric Turbulence in Optical Astronomy. *Prog. Optics*, 19:281–376, 1981.

[9] D.L. Fried. Statistics of a Geometric Representation of Wavefront Distortion. *J. Opt. Soc. Am.*, 55(11):1427–1435, 1965.

[10] F. Martin, R. Conan, A. Tokovinin, A. Ziad, H. Trinquet, J. Borgnino, A. Agabi, and M. Sarazin. Optical parameters relevant for High Angular Resolution at Paranal from GSM instrument and surface layer contribution. *Astron. Astrophys. Suppl. Ser.*, 144:39–44, 2000.

[11] von Kármàn, T. Progress in the Statistical Theory of Turbulence. *Proc Natl Acad Sci*, 34:530–539, 1948.

[12] C.R. Jenkins. Fast guiding and small telescopes in the 8-m era. *Mon. Not. R. Astron. Soc*, 294:69–92, 1998.

[13] T.W. Nicholls, G.D. Boreman, and J.C. Dainty. Use of a Shack-Hartmann wave-front sensor to measure deviations from a Kolmogorov phase spectrum. *Optics Letters*, 20:2460–2463, 1995.

[14] G.D. Boreman and J.C. Dainty. Zernike expansions for non-Kolmogorov turbulence. *J. Opt. Soc. Am. A*, 13:517–522, 1996.

[15] C. Rao, W. Jiang, and N. Ling. Spatial and temporal characterization of phase fluctuations in non-Kolmogorov atmospheric turublence. *Journal of Modern Optics*, 47:1111–1126, 2000.

[16] J.T. Winthrop and C.R. Worthington. Convolution formulation of fresnel diffraction. *J. Opt. Soc. Am.*, 56(5):588–591, 1966.

[17] D. Dravins, L. Lindegren, E. Mezey, and A.T. Young. Atmospheric Intensity Scintillation of Stars. I. Statistical distributions and temporal properties. *Pub. Astron. Soc. Pacific*, 109:173–207, 1997.

[18] D. Dravins, L. Lindegren, E. Mezey, and A.T. Young. Atmospheric Intensity Scintillation of Stars. II. Dependence on Optical Wavelength. *Pub. Astron. Soc. Pacific*, 109:725–737, 1997.

[19] D. Dravins, L. Lindegren, E. Mezey, and A.T. Young. Atmospheric Intensity Scintillation of Stars. III. Effects for Different Telescope Apertures. *Pub. Astron. Soc. Pacific*, 110:610–633, 1998.

[20] Vernin, J. and Muñoz-Tuñòn, C. Optical seeing at La Palma Observatory. I. General guidelines and preliminary results at the Nordic Optical Telescope. *Astron. Astrophys.*, 257:811–816, 1992.

[21] Vernin, J. and Muñoz-Tuñòn, C. Optical seeing at La Palma Observatory. II. Intensive site testing campaign at the Nordic Optical Telescope. *Astron. Astrophys.*, 284:311–318, 1994.

[22] M. Sarazin and F. Roddier. The ESO differential image motion monitor. *Astron. Astrophys.*, 227:294–300, 1990.

[23] A. Tokovinin and V. Kornilov. Accurate seeing measurments with MASS and DIMM. *Mon. Not. R. Astron. Soc*, 381(3):1179–1189, 2007.

[24] J.L. Codona. The scintillation theory of eclipse shadow bands. *Astron. Astrophys.*, 164:415–427, 1986.

[25] J.M. Beckers. A seeing monitor for solar and other extended object observations. *Exp. Astr.*, 12(1):1–20, 2002.

[26] G.H. Crescenti. A Look Back on Two Decades of Doppler Sodar Comparison Studies. *Bulletin of the American Meteorological Society*, 78(4):651–673, 1997.

[27] B.C. Platt and R. Shack. History and Principles of Shack-Hartmann Wavefront Sensing. *J. Refract. Surg.*, 17:573–577, 2001.

[28] G.A. Tyler. Bandwidth considerations for tracking through turublence. *J. Opt. Soc. Am. A*, 11:358–367, 1994.

[29] A. Tokovinin. From Differential Image Motion to Seeing. *Pub. Astron. Soc. Pacific*, 114:1156–1166, 2002.

[30] F. Roddier. Curvature sensing and compensation: a new concept in adaptive optics. *Appl. Opt.*, 27:1223–5, 1988.

[31] R. Donaldson *et al.* MACAO and its aplication for the VLT interferometer. In *Proceedings of the SPIE*, volume 4007, pages 82–93, 2000.

[32] R. Ragazzoni. Pupil plane wavefront sensing with an oscillating prism. *J. Mod. Opt.*, 43(2):289–293, 1996.

[33] R.J. Noll. Zernike polynomials and atmospheric turbulence. *J. Opt. Soc. Am.*, 66(3):207–211, 1976.

[34] G. Love. Wave-front correction and production of Zernike modes with a liquid-crystal spatial light modulator. *Appl. Opt.*, 36(7):1517–1524, 1997.

[35] W.J. Wild, E.J. Kibblewhite, and R. Vuilleumier. Sparse matrix wave-front enstimators for adaptive-optics systems for large ground-based telescopes. *Optics Letters*, 20(9):955–957, 1995.

[36] F. Vidal, E. Gendron, and G. Rousset. Tomography approach for multi-object adaptive optics. *J. Opt. Soc. Am. A*, 27(11):253–264, 2010.

[37] E. Gendron *et. al.* MOAO first on-sky demonstration with CANARY. *Astron. Astrophys.*, 529:L2, 2011.

[38] F. Vidal, E. Gendron, M. Brangier, A. Sevin, G. Rousset, and Z. Hubert. Tomography reconstruction using the Learn and Apply algorithm. In *1st AO4ELT conference - Adaptive Optics for Extremely Large Telescopes*, pages 07001–1 – 07001–6, 2010.

[39] M. Lloyd-Hart and P. McGuire. Spatio-temporal prediction for adaptive optics wavefront reconstructors. In *Proc. European Southern Observatory Conf. on Adaptive Optics*, pages 95–102, 1995.

[40] J. Osborn *et. al.* Using artificial neural networks for open-loop tomography. *Optics Express*, 20(3):2421–2434, 2012.

[41] R. Foy and A. Labeyrie. Feasibility of adaptive telescope with laser probe. *Astron. Astrophys.*, 152:L29–L31, 1985.

[42] C.A. Primmerman, D.V. Murphy, D.A. Page, B.G. Zollars, and H.T. Barclay. Compensation of atmopsheric optical distortion using a synthetic beacon. *Nature*, 353:141–143, 1991.

[43] C.E. Max *et. al.* Image Improvement from a Sodium-Layer Laser Guide Star Adaptive Optics System. *Science*, 227(5332):1649–1652, 1997.

[44] E.N. Ribak and R. Ragazzoni. Reduction of laser spot elongation in adaptive optics. *Optics Letters*, 29:1351–1353, 2004.

[45] L. Schreiber, I. Foppiani, C. Robert, E. Diolati, Conan J-M., and M. Lombii. Laser guide stars for extremely large telescopes: efficient Shack–Hartmann wavefront sensor design using the weighted centre-of-gravity algorithm. *Mon. Not. R. Astron. Soc*, 396:1513–1521, 2009.

[46] J-G. Cuby *et. al.* EAGLE: an MOAO fed multi-IFU working in the NIR. In *Proceedings of the SPIE*, volume 7439, page 77352D, 2009.

[47] J. Osborn, R. Wilson, T. Butterley, H. Shepherd, and M. Sarazin. Profiling the surface layer of optical turbulence with SLODAR. *Mon. Not. R. Astron. Soc*, 406:1405–1408, 2010.

[48] S.G. Els *et. al.* Thirty Meter Telescope Site Testing VI: Turbulence Profiles. *Pub. Astron. Soc. Pacific*, 121:527–543, 2009.

[49] M. Chun *et. al.* 'Imaka: a one-degree high-resolution imager for the Canada-France-Hawaii Telescope. In *Proceedings of the SPIE*, volume 7735, pages 773517–753517–16, 2010.

[50] Neyman, C. Atmospheric Parameters for Mauna Kea. Keck Adaptive Optics Note #303, 2004.

[51] D. Racine, R. amd Salmon, D. Cowley, and J. Sovka. Mirror, dome, and natural seeing at CFHT. *Pub. Astron. Soc. Pacific*, 103(667):1020–1032, 1991.

[52] A. Basden, R. Myers, and T. Butterley. Considerations for EAGLE from Monte Carlo adaptive optics simulation. *Appl. Opt.*, 49:G1–G8, 2010.

[53] R.W. Wilson. SLODAR: measuring optical turbulence altitude with a Shack-Hartmann wavefront sensor. *Mon. Not. R. Astron. Soc.*, 337:103–108, 2002.

[54] T. Butterley, R.W. Wilson, and M. Sarazin. Determination of the profile of atmospheric optical turbulence strength from SLODAR data. *Mon. Not. R. Astron. Soc.*, 369:835–845, 2006.

[55] R.W. Wilson and C.R. Jenkins. Adaptive optics for astronomy: theoretical performace and limitations. *Mon. Not. R. Astron. Soc*, 268:39–91, 1996.

[56] M. Sarazin, T. Butterley, A. Tokovinin, T. Travouillon, and R. Wilson. The Tololo SLODAR Campaign; Final Report. Technical report, ESO/CTIO/University of Durham/Caltech, 2004.

[57] R. Wilson, T. Butterley, M. Sarazin, G. Lombardi, M. Chun, S. Benigni, D. Weir, R. Avila, and J. Aviles. SLODAR turbulence monitors for real-time support of astronomical adaptive optics. In *Proceedings of the SPIE*, volume 7015, pages 70154K–1 – 70154K–9, 2008.

[58] A. Rocca, F. Roddier, and J. Vernin. Detection of atmospheric turbulent layers by spatiotemporal and spatioangular correlation measurements of stellar-light scintilation. *J. Opt. Soc. Am.*, 64(7):1000–1004, 1974.

[59] M. Azouit, J. Borgnino, and J. Vernin. Use of a linear photodiode array in order to estimate in real time the contribution of the lower atmospheric layers in astronomical-image degradation. *J. Opt.*, 9:291–299, 1978.

[60] A. Fuchs, M. Tallon, and J. Vernin. Focusing on a Turbulent Layer: Principle of the "Generalized SCIDAR". *Pub. Astron. Soc. Pacific*, 110:86–91, 1998.

[61] D. Garnier. *Profiling Atmopsheric Turbulence with Single Star SCIDAR*. PhD thesis, National Univeristy of Ireland, Galway, 2007.

[62] R. Avila, J. Aviles, R.W. Wilson, M. Chun, T. Butterley, and E. Carrasco. LOLAS: an optical turbulence profiler in the atmospheric boundary layer with extreme altitude-resolution. *Mon. Not. R. Astron. Soc*, 387:1511–1516, 2008.

[63] B.L. Ellerbroek and G.M. Cochran. A wave optics propagation code for multi-conjugate adaptive optics. In *Proceedings of the SPIE*, volume 4494, pages 104–120, 2002.

[64] R.A. Johnston and R.G. Lane. Modelling scintillation from an aperiodic Kolmogorov phase screen. *Appl. Opt.*, 39(26):4761–4769, 2000.

[65] D. Saint-Jaques. *Astronomical Seeing in Space and Time.* PhD thesis, University of Cambridge, 1998.

[66] N.M. Gavrilov, H. Luce, M. Crochet, F. Dalaudier, and S. Fukao. Turbulence paramater estimations from high-resolution balloon temperature measurements of the MUTSI-2000 campaign. *Annales Geophysicae*, 23:2401–2413, 2005.

[67] J.C. Christou *et. al.* Altair performance and updates at Gemini North. In *Proceedings of the SPIE*, volume 7736, page 77361R, 2010.

[68] J. Osborn, R. Wilson, V. Dhillon, R. Avila, and G. Love. Conjugate-plane photometry: Reducing scintillation in ground-based photometry. *Mon. Not. R. Astron. Soc*, 411:1223–1230, 2011.

[69] J-L. Prieur, G. Daigne, and R. Avila. SCIDAR measurements at Pic du Midi. *Astron. Astrophys.*, 371:366–377, 2001.

[70] R. Avila and S. Cuevas. On the normalization of scintillation autocovariance for generalized SCIDAR. *Optics Express*, 17:10926–10938, 2009.

[71] C. Lawson and R.J. Hanson. *Solving Least Squares Problems.* SIAM, 1987.

[72] J.-L. Starck and F. Murtagh. *Astronomical Image and Data Analysis.* Springer, 2002.

[73] V.A. Klückers, N.J. Wooder, T.W. Nicholls, M.J. Adcock, I. Munro, and J.C. Dainty. Profiling of Atmospheric Turbulence Strength and Velocity using Generalised SCIDAR Technique. *Astron. Astrophys. Suppl. Ser.*, 130:141–155, 1998.

[74] J. Osborn. *Profiling the turbulent atmosphere and novel correction techniques for imaging and photometry in astronomy.* PhD thesis, University of Durham, 2010.

[75] M. Chun, R. Wilson, R. Avila, T. Butterley, J. Aviles, D. Wier, and S. Benigni. Mauna Kea ground-layer characterization campaign. *Mon. Not. R. Astron. Soc*, 394:1121–1130, 2009.

[76] L. Catala. Atmospheric turbulence characterization and adaptive optics modelling for the Southern African Large Telescope. Master's thesis, Master *Physique Fondementale et Appliquée* OMEGA, Université de Nice Sophia–Antipolis, 2011.

[77] N. Védrenne, V. Michau, C. Robert, and J-M. Conan. C(n)(2) profile measurement from Shack-Hartmann data. *Optics Letters*, 32:2659, 2007.

[78] Austin, P. ATSC 500 - Boundary Layer Meteorology. http://clouds.eos.ubc.ca/~phil/courses/atsc500/docs/strfun.pdf, July 2012.

[79] Andersen, M.I. and Sorensen, A.N. Report 2: Image Quality at the Nordic Optical Telescope. Instrumentcentre for Jordbaseret Astronomisk Forskning, 1996.

[80] Fuensalida J.J., García-Lorenzo B., Delgado J.M., Rodríguez-Hernández M.A.C., and Vernin J. Sampling and Characterization of the Turbulence Vertical Distribution. Statistics of SCIDAR Profiling. In *Rev. Mex. Astron. Astroffs. Conf. Ser.*, volume 31, pages 86–92, 2007.

[81] G. Lombardi. Combining turbulence profiles from MASS and SLODAR, A study of the evolution of seeing at Paranal. ESO Garching. Doc. No. E-ELT-TRE-222-0215, 2008.

[82] Andor Technology. *Andor Luca Technical Specifications*, 2008. Doc. No. Luca(S) 658M.

[83] M. Sarazin and A. Tokovinin. The Statistics of Isoplanatic Angle and Adaptive Optics Time Constant derived from DIMM Data. In *Beyond conventional adaptive optics : a conference devoted to the development of adaptive optics for extremely large telescopes.*, pages 321–326, 2002.

[84] E. Masciadri, F. Lascaux, Fuensalida J.J., G. Lombardi, and H. Vázquez-Ramió. Recalibrated generalized SCIDAR measurements at Cerro Paranal (the site of the Very Large Telescope). *Mon. Not. R. Astron. Soc*, 420:2399–2418, 2012.

[85] Andor Technology. *Andor iXon Technical Specifications*, 2006. Doc. No. DV885LC.

[86] García-Lorenzo B. and Fuensalida J.J. Atmospheric optical turbulence at the Roque de los Muchachos Observatory: data base and recalibration of generaliszed SCIDAR data. *Mon. Not. R. Astron. Soc*, 416:2123–2129, 2011.

[87] A. Berdja. On the DIMM interpretation of non-Kolmogorov turbulence in the atmospheric surface layer. *Mon. Not. R. Astron. Soc*, 409:722–726, 2010.

[88] M. Goodwin, C. Jenkins, and A. Lambert. Improved detection of atmospheric turbulence with SLODAR. *Optics Express*, 15:14844–14860, 2007.

[89] R.W. Wilson, N. O'Mahony, C. Packham, and M. Azzaro. The seeing at the William Herschel Telescope. *Mon. Not. R. Astron. Soc*, 309:379, 1999.

[90] N. O'Mahony. Results from the Calibration of ING's RoboDIMM. Isaac Newton Group of Telescopes, 2005.

[91] M. Sarazin, J. Melnick, J. Navarrete, and G. Lombardi. Seeing is Believing: New Facts about the Evolution of Seeing on Paranal. *ESO Messenger*, 132:11–17, 2008.

[92] M.A. Holdaway *et al.* Comparison of Rio Frio and Chajnantor Site Testing Data. MMA Memo #152, 1996.

[93] *Climate Change 2001: Impacts, Adaptation and Vulnerability*, chapter 14. CUP, 2001.

[94] D. Föhring. A study of seeing and image quality for Durham AstroLab. Master's thesis, University of Durham, 2009.